NEUTRINO INTERACTIONS
IN NEON-HYDROGEN
AT HIGH ENERGY

BY

KENNETH JOHN POWELL

A thesis presented for the degree of Doctor of Philosophy of the University of London.

The Blackett Laboratory,
Imperial College of Science and Technology,
LONDON, SW7

October 1979

ABSTRACT

This thesis describes the general features of the Cern West Area Neutrino Facility Narrow Band Beam and the method used to obtain the antineutrino cross-section at high energy. The results of an investigation of the beam parameters obtained from the muon flux distributions are presented together with the latest data on the antineutrino cross-section from the WA47 exposure of the Big European Bubble Chamber.

CONTENTS

CONTENTS (Concluded)

FIGURE CAPTIONS

FIGURE CAPTIONS continued

5.5 Correction matrix for the calibration box spray effect

Chapter 6

6.1 Acceptance of the NBB as a function of angle and momentum

6.2 Four fields of view scanned at Ø cm in gap 2 - straight parallel tracks are muon tracks sheered due to developing of the emulsion.

6.3 Ø cm angular distribution of the tracks found in the emulsion with respect to the fitted beam direction.

6.4 3Ø cm angular distribution.

6.5 $\mu^-/\mu^+\delta$ as a function of radius in gap 2. (Neutrino and anti-neutrino).

6.6 Trapped μ as a function of radius in gap 2 (from TURTLE).

6.7 Closed collimator running compared with TURTLE distribution. in gap 2. (WA47 antineutrino running).

6.8 (a) Fitted K/π ratio in neutrino versus beam divergence, and

(b) K/π and χ^2 for various beam divergences.

6.9 (a) Muon profile in pit 2 showing one standard deviation error curves. Positives.

(b) The same for negatives.

(c) χ^2 of fit for a) versus K/π ratio.

(d) The same for b).

6.10 Light intensity versus pressure plot from the cerenkov.

6.11 North Area spectrum for π^+

6.12 North Area spectrum for K^+

6.13 North Area spectrum for π^-

6.14 North Area spectrum for K^-

6.15 K/π from North Area measurements.

Chapter 7

7.1 Muon and hadron P_t balance.

7.2 ϵ from section 7.1.1 versus E_h.

7.3 Neutral energy calibration for 70GeV/c π^- interactions.

7.4 Fiducial volume used in the WA47 experiment.

FIGURE CAPTIONS concluded

7.5 Wide band background flux and correction percentage as a function of neutrino energy at the position of BEBC for neutrino and antineutrino.

7.6 Final distribution of antineutrino event energies after all corrections.
Radius versus energy plot for antineutrino events in WA47.
Energy plotted as described in the text.

7.7 Number of events with $\epsilon > 20$GeV, $\theta_\mu > 5°$/15cm flux versus beam divergence, assuming σ/E =1.

7.8 σ/E versus energy for WA47. Also shown are the CDHS, Gargamelle and Wide Band test in Neon results. The curve is from Buras Gaemers, including charm.

Table of WA47 antineutrino cross-sections.

—00000—

CHAPTER 1

INTRODUCTION

1.1 HISTORY

The neutrino was first postulated to exist by Pauli in 1933 as a spin one half particle to explain the apparent non-conservation of angular momentum in the β decay of neutrons. This idea was made quantitative by Fermi[1] using the spinor formalism of Dirac. The first interactions of neutrinos were observed by Reines and Cowan[2] in 1956 who used the neutrino flux from a nuclear reactor. Their experiment showed that an $\bar{\nu}_e$ and a neutron were emitted from the interaction of a neutrino coming from β decay with nucleons and thereby demonstrated that neutrino interactions could be observed experimentally. This is now known as electron lepton-number conservation. The existence of two types of neutrino was demonstrated experimentally in 1962 at Brookhaven[3] using beams of pions and kaons which both decay to muons and neutrinos. The number of electron events seen was consistent with the known branching ratio of kaon into electron , neutrino plus pion and all other events were seen to have a muon in the final state. Thus there was another lepton conservation rule, that of muon lepton number, which was conserved independently of electron lepton number.

These reactions all occur through the exchange of a charged particle, known as the intermediate vector boson, and are given the generic name charged current, or CC interactions. However, some decays could not be described by charged current exchange alone.

Consider the decay $K^0_L \to \mu^+\mu^-$. Since strangeness is conserved in both strong and electromagnetic interactions, this decay must

proceed through the weak interaction. However, strangeness-changing charged current interactions are suppressed relative to non strangeness-changing interactions by only $\sin^2\theta_C \simeq .05$, but the branching ratio $K^0_L \to \mu^+\mu^- / K^0_L \to \text{all}$ is of the order 10^{-8}. Thus it seemed that either the neutral current interaction postulated by Weinberg and Salam[4] in 1967 was very weak or strangeness changing neutral currents do not exist.

In 1973 the existence of Neutral Currents (NC) was confirmed by the Gargamelle collaboration at CERN.[5] The suppression of strangeness - changing neutral currents was explained by the GIM[6] mechanism by the introduction of a fourth quark with charge +2/3 which cancels the exchange of the u quark in fig 1.1.

The discovery of $e\mu$ events in the e^+e^- storage rings SPEAR at SLAC[7] was shown to be due to a new lepton, the tau, which was assumed to have its own tau-neutrino to accompany it. In this way all the le ptons and quarks can be grouped into left-handed (i.e. V-A coupling, see chapter (2)) weak isospin doublets (Fig 1.2). The discovery of the b quark with charge -1/3 in 1978, introduced a new doublet. If the t quark were discovered the lepton-quark symmetry, which some theorists regard as a fundamental symmetry of nature, would be restored. At the time of writing the best chance of restoring this symmetry lies with the e^+e^- storage ring Petra, at Hamburg, but so far top (the t quark) has failed to show itself.

1.2 THE 200GeV/C NARROW BAND EXPERIMENT

With the advent of high energy proton accelerators at FNAL and CERN it became possible to produce high energy beams of pions and kaons which could be made to produce high energy beams of neutrinos by

allowing them to decay. The experiment on which this thesis is based was proposed in 1974 and was designed to study all aspects of neutrino physics at high energy. The Bubble chamber BEBC (Big European Bubble Chamber) was used to obtain the data, it being originally designed as a weak interaction chamber.

The neutrino beam was the CERN Narrow Band Beam which provides a dichromatic beam of Neutrinos of known energy spread. This beam enabled a more detailed and accurate study of neutrino cross-sections, structure functions and neutral current interactions than had previously been possible.

Six European research groups collaborated on the initial experiment in January 1977, which was given the label WA19, and were joined by another laboratory for further running at the end of 1978, designated WA47. (Refs. 1.8 - 1.13).

The subject of this thesis will be the authors' contribution to the data reduction of the events found on the WA19 film, and his work on the analysis of the flux data to obtain cross-sections for WA47.

CHAPTER 2

THEORY

2.1 KINEMATICS

Neutrino interactions take place through the exchange of either a neutral or charged intermediate vector boson Fig. (2.1). In describing this process, if final state hadron distributions are ignored, the reaction may be described completely with the knowledge of three variables. The ones measured experimentally are:-

E_ν - the laboratory incident neutrino energy

E_μ - the laboratory muon energy

θ_μ - the laboratory muon angle with respect to the incident neutrino direction.

From these variables, and the mass of nucleon one may construct several Lorentz invariant quantities:-

$$Q^2 = (k-k')^2 = 2E_\mu E_\nu (1-\cos\theta_\mu) - m_\mu^2$$
$$\nu = P.q/M = E_\nu - E_\mu$$
$$y = P.q/k.q = \nu/E_\nu$$
$$x = Q^2/2M\nu$$
$$S = (k+p)^2 = M^2 + 2ME_\nu$$
$$M = \text{proton mass}$$

the symbols are defined in fig. 2.1. Q^2 is the invariant mass of the exchanged boson, ν the energy transfer between the leptons, y the fraction of the incident neutrino energy carried by the hadronic final state after the interaction and s the total centre of mass energy. The significance of the variable x will become apparent later, but in fact is the fraction of the nucleon momentum carried by the struck quark-parton.

2.2 CROSS-SECTIONS

The cross-section for neutrino nucleon scattering depends upon the form of the interaction and is usually expressed in terms of the current-current hypothesis[1] which is written in the form

$$J_\mu(\text{lepton})\ J^\mu(\text{hadron})$$

The lepton current is well described in terms of dirac spinor fields and in weak interactions has a V - A form. That is, it is a sum of vector and axial vector currents, so called because of their spatial transformation properties. The hadron current is more complicated, however, if the weak interaction is mediated by a vector particle the maximum number of terms it may contain is 3, one for each spin component of the exchanged particle. Each term is multiplied by an undetermined function $W_i (i=1,2,3)$. These W_i (termed form factors) may in principle be different for neutrino, antineutrino and neutron and proton. Hence the maximum number of W's is 12 (three for each interaction νp, νn, $\bar{\nu} p$, $\bar{\nu} n$). However, for strangeness conserving processes the number of independent W_i may be reduced by use of charge symmetry:-

$$W_i^{\nu n} = W_i^{\bar{\nu} p} \qquad W_i^{\nu p} = W_i^{\bar{\nu} n}$$

$$\text{and} \quad W_i^{\nu N} = \tfrac{1}{2}\left[W_i^{\nu n} + W_i^{\nu p}\right] = \tfrac{1}{2}\left[W_i^{\bar{\nu} p} + W_i^{\bar{\nu} n}\right] = W_i^{\bar{\nu} N}$$

so the number of independent W's is now three.

If final state hadron distributions are not observed, there are two independent kinematical variables at the hadronic vertex namely Q^2 and ν. Thus the W_i can only be functions of these two variables. By summing over all possible polarisation states we find the cross-section for charged current neutrino nucleon scattering is then

$$\frac{d^2\sigma}{dQ^2 d\nu} = \frac{G^2}{2\pi M}\frac{E_l}{E_\nu}\left[\cos^2\frac{\theta_\mu}{2}\, W_2(Q^2,\nu) + 2\sin^2\frac{\theta_\mu}{2}\, W_1(Q^2,\nu) \pm \frac{E_\nu + E_l}{M}\sin^2\theta/_2\, W_3(Q^2,\nu)\right] \tag{2.1}$$

2.3 SCALING

Of fundamental importance to the analysis in this thesis and all neutrino experiments is the hypothesis of scaling, first proposed by Bjorken[2]. The scaling argument states that in the high energy limit ($E_\nu \gg M$) the dimensionless structure functions become independent of energy and are functions only of the dimensionless ratio:

$$x = Q^2/2M\nu$$

If there are any thresholds in the reaction due to the production of heavy particles (e.g. charm) then scaling ought to set in at higher energy. The assumption is that there are no intrinsic masses in the problem above the mass m and at high energy the cross-section should become independent of this mass. Rewriting the cross-section formula 2.1 in terms of the scaling variables x and y we find, for charge symmetric nuclei,

$$\frac{d^2\sigma}{dx\,dy} = \frac{G^2 s}{2\pi}\left[(1-y)F_2(x) + xy^2 F_1(x) \pm y(1-y/2)xF_3(x)\right] \quad (2.2)$$

where, as expected the term in brackets has no s dependence. The F_i are related to the W's by

$$F_1(x) = W_1(Q^2,\nu)$$
$$F_2(x) = \frac{\nu}{m} W_2(Q^2,\nu)$$
$$F_3(x) = \frac{\nu}{M} W_3(Q^2,\nu)$$

and are assumed the same for ν , $\bar{\nu}$ using charge symmetry. The main results of the scaling hypthesis are that the neutrino cross-section rises linearly with s, and the x,y dependance is independent of s.

2.4 PARTON MODEL

If we assume that hadrons are made up of constituents of different types, each with its own distribution function in the fractional momentum of the hadron carried by that constituent, then if ξ is the fractional momentum

$$\int f_j(\xi)\,d\xi = N_j = \text{the number of constituents } j$$
$$\sum_j \int \xi f_j(\xi)\,d\xi = 1$$

we further assume that these constituents interact independantly. (i.e. do not interact with each other and have point-like cross-sections). It may then be easily seen that if such a constituent is scattered, it results in a momentum transfer $Q^2 = 2\nu\xi m$ from the following argument.

Consider the frame in which the parton recoils with equal

momentum in the opposite direction (fig. (2.2)). We have, for massless particles

$$P = (p, 0, 0, p) \qquad q = (0, 0, 0, q)$$

and

$$q = -2\xi p$$

$$\nu = P \cdot q/m = 2\xi p^2/m$$

$$Q^2 = -q^2 = 4\xi^2 p^2$$

$$\Rightarrow \quad x = \frac{Q^2}{2m\nu} = \xi$$

the neutrino-nucleon cross-section may now be written as a sum of the elementary point like cross-sections:-

$$\frac{d^2\sigma}{dx\,dy} = \sum_j f_j(x) \frac{d\sigma_j}{dy}$$

Fig (2.3) shows the elementary cross-sections in Quark Parton Model for various scattering processes.

2.5 QUARK PARTON MODEL

It is assumed that the partons are the spin one half quarks of ordinary hadron spectroscopy, bound by gluons which have no weak or electromagnetic interactions. Nucleons are assumed to be made of valence quarks surrounded by a sea of quark anti-quark pairs. For the proton, the valence quarks are uud and by definition all quark distribution functions are measured with respect to the proton. From the quantum numbers of the proton, the following identities hold

$$\int (u(x) - \bar{u}(x))dx = 2 \qquad \int (s(x) - \bar{s}(x))\,dx = 0$$

$$\int (d(x) - \bar{d}(x))dx = 1 \qquad \int (c(x) - \bar{c}(x))\,dx = 0$$

where u, d, s, c, $\bar{u}$, $\bar{d}$, $\bar{s}$, $\bar{c}$ are the up, down, strange and charm quark and anti-quark distribution functions which are functions of x only. The neutron distribution functions are obtained from the proton distribution functions by exchanging u and d.

The cross-sections per nucleon for targets with equal numbers

of protons and neutrons are

$$\left.\begin{aligned}\frac{d^2\sigma^{\nu}}{dx\,dy} &= \frac{G^2 s}{2\pi}\left[q(x) + (1-y)^2\,\bar{q}(x)\right] \\ \frac{d^2\sigma^{\bar{\nu}}}{dx\,dy} &= \frac{G^2 s}{2\pi}\left[q(x)(1-y)^2 + \bar{q}(x)\right]\end{aligned}\right\} \qquad (2.3)$$

$$q(x) = x[u(x)+d(x)] \qquad \bar{q}(x) = x[\bar{u}(x)+\bar{d}(x)]$$

and we have ignored any possible contributions from strange or charmed quarks. (See Appendix B).

2.6 CONSEQUENCES OF THE QUARK PARTON MODEL

By comparing the equations 2.2 and 2.3 (see appendix B) the following correspondences may be made between the quark distribution functions and the structure functions:-

(i) $2xF_1 = F_2$

(ii) $xF_3 = q - \bar{q}$

(iii) $\sigma_{\nu} + \sigma_{\bar{\nu}} = \frac{4}{3}\frac{G^2 s}{2\pi}\int F_2\,dx$

(iv) $\sigma_{\nu} - \sigma_{\bar{\nu}} = \frac{2}{3}\frac{G^2 s}{2\pi}\int xF_3\,dx$

(v) $$\frac{\int xF_3\,dx}{\int F_2\,dx} = \frac{Q-\bar{Q}}{Q+\bar{Q}} = \frac{2(\sigma_{\nu}-\sigma_{\bar{\nu}})}{\sigma_{\nu}+\sigma_{\bar{\nu}}}$$

(vi) $$\frac{\bar{Q}}{Q} = \frac{R-1/3}{1-R/3} \qquad R = \frac{\sigma_{\bar{\nu}}}{\sigma_{\nu}}$$

in the above relations the y dependence has been explicitly integrated over, and the notation:-

$$Q = \int q(x)\,dx$$

$$\bar{Q} = \int \bar{q}(x)\,dx$$

has been used.

The first of the above relations is known as the Callan-Gross relation[3] and if found to hold tests the spin one-half nature of the quark fields. Experimentally, this is measured by fitting the y distributions in charged currents and if found not to be true adds an extra term $R(1-y)$ into the brackets of equations 2.3, where

$$R = \frac{\int (F_2 - 2xF_1)\,dx}{\int 2xF_1\,dx} \qquad (Q^2 \gg M^2)$$

All experiments so far are consistent with the value $R = 0$, albeit with large errors, and thus demonstrates the spin one-half character of the quarks. Using this relation and charge symmetry the number of independent structure functions has been reduced from three to two, namely F_2 and xF_3.

Relation (iii) enables the fraction of the nucleon momentum carried by the quarks and antiquarks to be measured, with the value of G^2 in principle already measured in other weak interaction experiments.

Relations (ii) and (iv) deal with the difference of neutrino and anti-neutrino scattering and measure the valence quark distributions. The measurement of F_3 itself is particularly important owing to the Gross-Lewellyn Smith sum rule[4] which states

$$\int_0^1 xF_3 \frac{dx}{x} = 3$$

i.e. the number of quarks in the nucleon should be three. This can only be measured from the differential cross-sections which will not be discussed here.

Relations (v) and (vi) follow immediately from relations (i) - (iv) and allow the relative anti-quark momentum fraction to be measured.

With the discovery of scaling violations at SLAC[5], and their subsequent confirmation by the experiment described in this thesis at higher Q^2, the quark distribution functions become dependent on Q^2

as well as x. This analysis also requires a study of the differential cross-sections and will not be attempted in this thesis.

We continue with a description of the experimental layout of WA19 and 47 and a presentation of the authors' work on the neutrino flux for WA47. The final chapter deals with the cross-section data available at the time of writing.

CHAPTER 3

BEBC, EMI, SCANNING AND MEASUREMENT

The data analysed in this thesis was obtained in the Big European Bubble Chamber (BEBC) at CERN exposed to the West Area Neutrino Facility (WANF) 200GeV/C Narrow Band Beam. Data taking was performed in January 1977, with the first results appearing in September 1977. This chapter will describe the chamber and its External Muon Identifier (EMI) and the method used at Imperial College to analyse the film. A description of the beam, and the authors' work on flux measurement is left to later chapters.

3.1 BEBC

3.1.1 CHAMBER CONSTRUCTION

The body of the chamber is essentially an upright cylinder of radius 1.85m and height 4m, made of 8 cm thickness stainless steel and completely enclosed in a vacuum tank to reduce heating of the liquid inside to a minimum. The piston is housed in a cylindrical extension of the chamber and is 181 cm in diameter. The inside of the chamber is lined with a retro-reflective material (Scotchlite) to enable the bubbles formed by tracks passing through the chamber to be viewed as light images on a dark background. The scotchlite has fiducial marks (fixed reference points) printed onto it for off-line measurement purposes. The general layout of the chamber is shown in Figs. (3.1) and (3.2).

3.1.2 MAGNETIC FIELD

In order to measure the momentum of charged tracks originating in the chamber liquid, BEBC is surrounded by two super-conducting coils raised to a 17 volt potential and supplied with a current of 5,700 Amperes. These coils produce an approximately uniform magnetic field of 3.5T within the chamber volume, which is mapped out with Hall probes and supplied as a set of titles (data cards) for the geometry programmes to reconstruct the momenta of the tracks off-line.

3.1.3 CAMERAS AND OPTICS

The hemispherical dome of BEBC is fitted with five port-holes, four of which are supplied with cameras, each with their own flash tube to enable stereoscopic reconstruction of the events in the chamber. Due to the large size of the chamber, fish-eye optics are used so each camera views as much of the chamber volume as possible. The fiducial marks on the side of the chamber were used to fit the optical distortion parameters of the lenses. These parameters are used by the geometry program along with the magnetic field map and the fiducial marks for event reconstruction by computer.

3.1.4 LIQUID

In order to perform a neutrino experiment in a bubble chamber the liquid has to have very special properties. At high energies, many photons will be emitted from the primary vertex, and unless the radiation length (distance for $(1 - e^{-1})$ of the photons to be converted) is small much of the neutral energy will escape from the chamber and hence be unmeasurable.

Secondly, in order to gain sufficient event rate the liquid should be as dense as possible, that is, the chamber should have as large a fiducial mass as possible.

Thirdly, for later analysis of the data in terms of scaling variables (described in chapter 2) the liquid should have equal numbers of protons and neutrons, i.e. be isoscalar.

For this experiment, a 74% molar mixture of Ne-H_2 (n/p = .93) was chosen, the radiation length being 44 cms. Fig. 3.3 shows the conversion length of the photons for charged current events found during

the WA19 running, and Fig. 3.4 summarises the operating conditions of the chamber.

3.2 THE EMI

3.2.1 CONSTRUCTION

The bubble-chamber is surrounded by an array of Multi-wire proportional chambers which serve to identify muons coming from neutrino interactions in the chamber liquid, and is known as the External Muon Identifier (EMI).

The EMI is situated 7m from BEBC and consists of high resolution chambers in the forward direction for identification of fast muons and lower resolution chambers for slower muons arranged around the chamber and spanning $\pm 80^{\circ}$ horizontally and $\pm 23^{\circ}$ vertically viewed from the centre of the bubble chamber. In all, fifty chambers were used, the dimensions and layout of the wires in each chamber are shown in Fig 3.5.

In between BEBC and the EMI are between 5 and 15 interaction lengths of iron to stop hadrons leaving the bubble chamber from hitting the EMI.

3.2.2 EMI INEFFICIENCY

The EMI may lead to a mis-classification of CC and NC events due to three effects:-

(a) For low momentum muons the track may not reach the EMI as it has short range or becomes trapped by the magnetic field in or around the chamber. This effect was seen to be small above a momentum of 5 GeV/C and so a cut was imposed at this momentum with all events below the cut being deliberately classified as NC. Above 5 GeV/C the inefficiency of the EMI was estimated in two ways:

(i) A sample of 2000 straight through beam associated muons of different momenta and angles were measured and extrapolated to the EMI by the EMI programme (to be described later).

(ii) A comparison of the P_T spectrum of right and wrong sign tracks in NC was made. There was an excess of right sign tracks at high P_T which was interpreted as being due to electronic EMI inefficiency. Both methods give the same result of $(2.5 \pm 1.0)\%$ inefficiency above 5GeV/C muon momentum.

(b) Accidental association of hits in the EMI with the prediction from the extrapolation programme generated false charged-current events. This was estimated by attempting to associate hits from the previous beam spill to the extrapolation of the hadron tracks from a different pulse. This gives approximately 3% mis-classification of NC events as CC events per leaving right sign hadron in neutrino, and 1% in anti-neutrino.

(c) It is possible for a leaving hadron to decay in flight and give a false muon hit in the EMI. This was found to be a small effect and was ignored in this experiment.

3.3 SCANNING

3.3.1 INITIAL SCANS

After developing by CERN the rolls of film are sent out for data reduction to each of the six laboratories in the collaboration. This and subsequent sections describe the method employed at Imperial College to prepare the final DST (Data Summary Tape) of the events found on the rolls of film allocated to Imperial College.

On arrival at Imperial College the film is cut into quarter rolls

(each with 1500 frames on three views) for easier handling on the scanning machines. Two initial scans on three views are performed by trained scanners on all the film to locate the various types of event. The various classes of event recorded were:-

(a) Background Events

(i) X - event due to an incoming hadron (forward or backward) not signed by a δ ray (a knock-on electron kicked out of an atom by the hadron)

(ii) Y - event due to an incoming hadron signed by a δ ray

(iii) Z - low energy neutron stars, and a possible source of contamination in the Neutral Current sample of events

(iv) W - neutrino interactions in the wall of the chamber

(b) Neutrino Events

Any other event in the chamber liquid which cannot be ascribed to the above background types is assumed to be from a neutrino interaction.

Single prong events (events with only one charged track leaving the primary vertex) were not recorded.

After the two initial scans were performed a comparison list was made and a third scan was performed by physicists, to check the events found on the first two scans.

3.2.2 THIRD SCAN

Owing to the complexity of high-energy neutrino events (the average charged hadron multiplicity is of the order of six or seven) all candidate neutrino events have to be measured by hand as automatic measuring devices are incapable of disentangling the hadronic shower. To make the measuring as quick as possible and to avoid incorrect

topologies being entered to the measuring programme all events are drawn and labelled by physicists before being sent for measurement. The agreed labelling code for this experiment is shown in Fig(3.6) subsequently all tracks with their code appear on the DST for later analysis.

3.3.3 SCANNING EFFICIENCY

The scanning of the film is not perfect and it is expected that some events will be missed by the scanners due to human error. Thus one must calculate the probability that an event will be missed off the final third scan list. Assuming the first and second scans are independent one may compare the numbers of events found and obtain this number. For Imperial College it was found to be 99%, consistent with the other laboratories in the collaboration. This result is important for total cross-section, to be evaluated later.

3.4 MEASUREMENT OF EVENTS

3.4.1 ONLINE GEOMETRY ANALYSIS

The online measuring programme uses digitised information as input concerning the camera and bubble-chamber fiducials for use in online fitting of each track as it is measured by the operator. A two way dialogue between the programme and the operator enables the frame number, topology and end codes to be recorded on a disk file by the program.

Each track in an event is measured individually with approximately 5 cm spacing between measurement points. When the track has been measured the data are sent to the Online Geometry Analysis programme (OLGA) which is normally resident on disk, but is 'woken up' by the measuring programme when the measurement of a track is complete.

This programme takes the raw measurement data and attempts a

simple helix fit to obtain the momentum of the track and the spread of the measurement points about the fit. The results are then communicated back to the operator. If the fit is a poor one (large spread of data points or no fit possible) the operator is requested to repeat the measurement and check that the same track has been measured on all views. If this procedure is repeated three times with no fit possible and the track has no secondary tracks coming from its end point (i.e. the track is not interacting) the program goes on to the next track. If the track interacts then the operator is requested to enter the topology of the interaction and measure all the secondary tracks.

The exceptions to this procedure are:-

(i) When one or more tracks curve through more than 120°. Since the programme uses the end point of the track, all such tracks have to be treated specially, and must be measured on a view by view basis, the programme then sorts out the tracks from each other and makes helix fits as described previously.

(ii) The momenta of short stopping tracks (protons, and nuclear fragments) are obtained by range, and only the beginning middle and end points of the track are measured.

Gammas and V^{o}'s are measured at the end of the event and in addition to obtaining the momentum of the track, the program makes fits to all upstream vertices (primary, and secondary). Once the measurements have been accepted by the programme, the raw measurement data are written out onto a disk file for off-line geometry analysis.

3.4.2 OFFLINE GEOMETRY ANALYSIS & EMI PROGRAMMES

After one quarter roll has been measured the data from the measur-

ing program are run through an off-line Hydra Geometry package which essentially repeats the on-line fits but also does fits for all relevant mass hypotheses (for example, in the case of leaving tracks it will attempt a muon fit, as well as all relevant hadron fits). The program does a 3C (3 constraint) fit to V^0's to obtain the mass of the neutral. For gammas it performs a 4C and 2C fit to all possible upstream vertices and outputs the results of its fits in standard Hydra Geometry bank structure.

The EMI program extrpolates all leaving tracks through the fringe field of the bubble chamber including multiple scattering in the iron between the chamber and the EMI to the plane of the EMI and calculates the position the track would have hit the EMI if it were a muon. It then compares this predicted hit with any recorded hits in the EMI and calculates a χ^2 using the bubble chamber measurement errors.

The final decision on whether a track is a muon is left to the programme DECID, which essentially calculates the χ^2 and imposes a cut, chosen to be $\chi^2<5$. All leaving tracks with $\chi^2<5$ retain their muon hypotheses, tracks with $\chi^2>5$ are excluded from being muons.

3.4.3 CHECKING OF THE EVENTS

Once the events have been passed through the chain of analysis programmes the physicists go back to the scanning table and check that the events have been measured correctly. The most important checks made are that no tracks have been missed off the drawing or have been omitted from measurement. The physicist also checks that all tracks have been labelled correctly and rules out obviously incorrect mass

assignments and V^0 or gamma associations by checking with the event on the film. Events which have missed tracks or poorly measured tracks ($\Delta p/p > 30\%$ for hadrons or muons and $\Delta p/p > 50\%$ for electrons) are sent for remeasurement. If the remeasurement is still not successful the physicist may decide to resubmit the track or event for another measurement, or may decide not to if it is obvious that no improvement can be made (e.g. very fast electrons in which the charge cannot be determined).

When all the measurements have been finalised, the charged current events with poorly known muon momentum are run through a momentum and error improvement programme. This uses the geometry and EMI data points to make a refit of the muon parmeters. It has been shown that the angles calculated through this procedure are unbiased.[3)]

Finally, all the measurements from all laboratories were combined and a condensed DST was produced from the Geometry Output which contains all the relevant information for data analysis. The DST was in card image form for WA19 with one card for each track, specifying the track label and code, mass hypothesis, momentum and two angles in the bubble chamber co-ordinate system and χ^2 or probability for a given hypothesis. This DST was later transformed to a Hydra bank structure for WA47.

CHAPTER 4

THE NEUTRINO BEAM

4.1 GENERAL CONSIDERATIONS

The main source of neutrinos at proton accelerator machines are the decays $\pi \to \mu\nu$ and $K \to \mu\nu$ which are produced by the interaction of protons with a target. Owing to the small size of the neutrino cross-section, the study of neutrino interactions with matter only became possible with the advent of high intensity beams, and the development of detectors with large fiducial mass (see section 3.1). In WA47 the neutrino flux traversing BEBC was $\sim 10^{3}$ cm^{-2} the fiducial mass was 16.8 tons and using $\frac{\sigma}{E} \sim 10^{-38}$ cm^{2}/nucleon of the order of $\cdot 03$ events per accelerator pulse were found.

In order to obtain the highest neutrino flux possible, the π and K mesons must be allowed to decay over the largest possible distance. This must be compromised with the fact that all beams have an inherent divergence (i.e. cannot be perfectly focused), and hence all the parents cannot produce neutrinos with the possibility of going through the detector. The final major requirement of all neutrino experiments is a large shield infront of the detector to absorb the undecayed pions and kaons, and to reduce the flux of muons at the detector to a minimum leaving only the neutrinos to pass through the detector.

The two major types of neutrino beam are the Wide Band and Narrow band beams. In the wide band beam the major objective is to obtain the highest possible flux of neutrinos, and thus all the parents of the widest possible momentum bite are focused. This is achieved through the use of rotationally symmetric magnetic fields created by passing large pulsed currents (100kA) around the surface of a conductor. Because of the shape of these conductors they are usually called magnetic horns.

(Fig 4.1). Sign selection is performed by selecting the sign of the current flowing in the conductor. Since no information is available from the beam itself about the energy of a particular event, the detector must have good energy resolution, and the energy spectrum of the beam must be inferred from the π and K production spectrum.

With the introduction of high energy and high intensity proton accelerators at CERN and FNAL it was possible to both sign and momentum select the parent muons and still retain a sensible event rate in the detector. These beams are the so-called Narrow Band Beams which use conventional quadrupoles (focusing devices) and bending magnets to perform the selection. The chief advantage of this type of beam is that if the parent π's and K's are momentum selected with a small momentum bite, one may use the kinematical relation between neutrino energy and decay angle, this allows the neutrino energy to be inferred (within a certain tolerence) from its radius of interaction in the detector.

4.2 PRINCIPLE AND DESIGN OF THE NARROW BAND BEAM AT CERN

4.2.1 KINEMATICS

The relation between the neutrino energy and its decay angle with respect to the parent beam direction follows immediately from four momentum conservation, and is

$$E_\nu = \frac{p\,(1-(m_\mu/m)^2)}{1+\gamma^2\theta^2}$$

where p is the parent beam momentum

m_μ is the mass of the muon

m is the mass of the parent

$\gamma^2 = (1-\beta^2)^{-1}$, $\beta = v/c$

θ is the decay angle of the neutrino with respect to the parent beam direction.

Consider Fig. 4.2. From this diagram and the above relation, it is clear

that at a given radius in the detector there is a minimum and maximum energy which may be attained by any neutrino, given by

$$E_\nu^{min} = \frac{E_\nu^0}{1 + \gamma^2\theta^2_{max}}$$

$$E_\nu^{max} = \frac{E_\nu^0}{1 + \gamma^2\theta^2_{min}}$$

where $E_\nu^0 = P(1 - (m_\mu/m)^2)$

Thus the resolution on the neutrino energy inferred from its radius of interaction only is

$$\frac{\Delta E}{E} = \frac{\gamma^2[\theta^2_{max} - \theta^2_{min}]}{1 + \gamma^2(\theta^2_{max} + \theta^2_{min})}$$

from which it is clear that the energy spread in the kaon peak is smaller than in the pion peak since $\gamma = E/M_p$, and that to obtain the best resolution, the length of the decay tunnel should be as small as possible without compromising the neutrino intensity. All the above applies for a zero divergence monochromatic parent beam, but is not significantly altered if the beam divergence is included, since the beam divergence is of the order of $\theta_{max}/10$. The momentum bite of the beam also does not alter the above argument significantly. Fig 4.3 shows the variation of E and $\Delta E/E$ with radius.

4.2.2 THE CERN NARROW BAND BEAM

This section describes the general features of the neutrino beam line as it was for both the WA19 and WA47 experiments. The proton beam was extracted at 400 GeV/C from the SPS (Super Proton Synchrotron) in two bunches, separated by two SPS revolutions (~4μs). The general layout of the beam is shown in Fig 4.4, and the magnetic beam line is shown in Fig. 4.5 in greater detail.

(i) TARGET

When the protonshave been extracted from the SPS, they pass through the neutrino switch-yard, which selects either the wide band or the narrow band beam lines. In the former the protons are already pointing in the direction of BEBC, but in the Narrow Band configuration they are pointing at 15 mr away from the target BEBC axis. This is so that the decays from pions and kaons before momentum and sign selection (i.e. the wide band background) give as small a contribution to the neutrino flux as possible in BEBC. The target itself was 90 cm (3 interaction lengths) long; 2 cm diameter Beryllium rod, designed for maximum proton usage and minimum π and K reabsorption.

(ii) MAGNETIC BEAM LINE

After leaving the target the parents and protons are focused by three quadrupoles and then bent horizontally towards the momentum slit. Before reaching the slit the protons are dumped into a large copper block, the proton dump by a septum magnet. The π's and K's are then focused and bent in preparation for momentum selection.

The momentum slit is a 3 m long iron block with a hole bored through to allow the parents of the desired momentum to be transmitted through to the end of the beam line. Parents of any other momentum are bent such that they are not accepted by the slit, but are absorbed by it. The slit is made in two sections so that the horizontal and vertical widths may be altered to suit the beam line conditions.

After leaving the slit the parents are bent more on line with BEBC and then focused with another pair of quadrupoles. The end of the magnetic beam line comes with the final train of bending magnets

which brings the beam on-line with BEBC and a final quadrupole for further focusing.

At the end of the magnetic beamline is a differential Čerenkov detector for measuring the hadron composition of the beam. This is essential since the relative proportions of kaons and pions must be known in order to measure the high energy neutrino cross-section.

(iv) THE DECAY TUNNEL

The magnetic beam line is followed by a 1.2 m diameter 290 m long decay tunnel evacuated to 5 torr, to allow the parents to decay and produce neutrinos as described above. At the end of the tunnel indented into the shielding and thermally isolated from it, is a large calorimeter block for the measurement of thehadron flux by its temperature rise, due to the energy deposited in it by the hadrons.

(v) SHIELDING

Following the decay tunnel is an iron shield of 185 m total length to absorb the muons from the parent decays. At various positions in the shielding there are gaps of length $\sim$ 95 cm equipped with arrays of solid state detectors to enable the muon flux to be continuously monitored. Since these detectors provide the basis for the cross-section normalization in the WA19 and 47 experiments the detectors and their arrangement in the gaps will be described in greater detail later.

Following the iron shielding is 223 m of rock and earth to absorb any muons not already stopped by the iron.

Finally, the centre of BEBC is situated 822 m away from the target, followed by the WA1 counter detector, the WA18 counter and the bubble chamber Gargamelle.

4.3 FLUX MEASUREMENT

The neutrino flux can be measured by either of two methods, hadron flux measurement or muon flux measurement. The muon method offers the advantage that the beam profile can be monitored continuously and checked for shape, positioning and radial symmetry, whereas the hadron flux method only gives the total flux. The positioning of the beam is of special importance in narrow band experiments since one of the chief advantages of this type of beam is that the neutrino event energy may be inferred from its radius. This can clearly only be accomplished if the beam is well centred. The following two sections describe the two methods, with particular emphasis on the muon flux method since this was used in WA19 and 47.

4.3.1 HADRON FLUX

The hadron flux is measured by a device called a Beam Current Transformer placed on the same monitoring platform as the Čerenkov. This consists essentially of a coil of wire placed near to the hadron beam. When the beam passes by the BCT it induces a current in the wire which is summed up for thewhole of the running of the experiment. Using this information and the composition of the beam (i.e. by knowing how many of the hadrons were protons), the total π and K flux may be determined. Knowing this, the decay length and kinematics of the decay of both types of muon, the total neutrino flux may be determined.

4.3.2 MUON FLUX MEASUREMENT

(i) Principle of the muon flux measurements

As already stated, the muon flux method provides for continuous on-line monitoring of the beam stability and centring. The flux is measured by arrays of detectors placed in gaps at 9.2 m, 29.6 m, 49.7 m, 70.1 m, 94.1m, and 118.6 m depth in the iron shielding. In each of these

gaps, the detectors are mounted on a moveable support plate as shown in Fig. 4.6. The detectors have to be moveable since the centre of the wide band beam is displaced with respect to the narrow band beam by of the order of 30 cm.

Each gap is also equipped with a box of detectors with varying sensitivities. This box is mounted on a gantry which is driven by rack and pinion drives to enable the box to move over the whole gap and measure the flux at any position. The major purpose of this box (hereafter called the calbox) is to calibrate the fixed detectors throughout the duration of the experiment. In addition, another box of detectors also equipped with a set of detectors of varying sensitivity moves from gap to gap at the end of each period of running (usually ten days) and is fixed onto the calibration box for a whole period. The purpose of this box (known as the refbox) is to calibrate each of the calibration boxes to each of the others. In this way, all the detectors in all gaps are linked electronically to each other. The final absolute calibration of the detectors is done by nuclear emulsion, and will be described later.

This procedure is particularly important for the wide band configuration since the neutrino energy spectrum is a sum of all parent production angles and momenta and must be varied to fit the muon energy spectra or distribution with depth in the shielding, and the parent production spectra. (The distribution of muons with depth clearly measures their energy distribution since the muons lose energy through ionisation and δ-ray production in the shielding). However, this is not so important in the narrow band beam since only a well defined momentum is accepted and the neutrino spectra are well determined with a knowledge of the decay kinematics and the K/π ratio at the target. In practice, in the narrow band beam only gap two is used since this is free of background from the hadron interactions in the beginning of the shielding.

Usually only part of the support plate is used for mounting the fixed detectors, viz., the central position, the horizontal bar, and the two concentric rings at 15 cm and 30 cm radius from the centre of the support plate.

(ii) THE SOLID STATE DETECTORS

Before the final system as it is known now was set up, many types of detector were tested for durability, since the detectors were expected to withstand high radiation doses over a long period of time and still maintain their accuracy of flux measurement. See Ref. (6.1) for a complete description of the initial detector testing phase.

Silicon detectors have the advantage over ionization chambers in that they are small, have a high signal, low bias voltage and are easy to handle. Unfortunately they are susceptible to radiation damage and must therefore be continually checked for constancy.

The basic operating principle of the detectors is the separation by an electric field of the electron-hole pairs created by a minimum ionising particle traversing the detector. In order to achieve full collection efficiency the detector must be fully 'depleted', i.e. made completely clear of free charge, since if this is not the case, some of the pairs created in the detector will recombine with the free charge in the non-depleted layer and hence will not be collected.

The detectors used in the gaps are operated in the so-called charge integration mode, since single particle counting is not possible with the fast extraction from the SPS ($\sim 20\mu s$). The charge obtained is corrected for the natural leakage current of the detector. This is measured between SPS pulses and the correction is applied every 15 minutes.

The nominal sensitivity of any detector may be obtained from

its dimensions. This is subject to error, since the sensitive area of the detector is governed by the irregular shape of the epoxy mounting and the depleted layer extends underneath the mounting. This may be partially accounted for by increasing the sensitive radius by one detector thickness. Thus, the sensitivity of the detector defined as the number of minimum ionising particles per square centimetre required to make one pico-coulomb of charge in the detector is

$$S_D = \left[\frac{401}{3.62} \times 1.6 \times 10^{-7} \times d \times (\pi(d+r)^2) \right]^{-1}$$

where d is the thickness of the detector

r is the radius of the detector

The energy loss of a minimum ionising particle in silicon is 401 eV/μm and the energy required to make an electron-hole pair is 3.62 eV.

In principle therefore, it is simple to measure the muon flux from the known properties of the detector and the coulombs detected in it. However, it was discovered in the early days of the Gargamelle experiment that this method did not work, because the muons when leaving the end of the shielding, bring with them a shower of knock-on electrons which are also minimum ionising and also create charge in the detector. The solution adopted then, and also adopted now, is to expose a nuclear emulsion placed infront of the detector for a few accelerator bursts. The sensitivity of the detector may then be worked out from the voltage collected during the exposure, and the number of muons counted in the emulsion.

The relative calibration of the detectors will be described later. For convenience we record here that we assume the response of the detector to the muon flux is linear and is related to the sensitivity of the detector by a relation of the form

$$N_\mu = (V - O) \times \frac{S_D}{G} \qquad (4.2)$$

where O is an offset

V is the voltage at the output of the detector amplifier

G is the gain of the detector amplifier

Previous work on the relative calibrations has shown that the offset is small and therefore we shall usually set this to zero in future.

(iii) OTHER BEAM MONITORS

Apart from the BCT and the solid state detectors, the beam is equipped with other sensors at several positions to monitor its shape.

(a) The target monitors

A set of secondary emission monitors (SEM's) (a set of strips sandwiched by electrode planes to collect the knock on electrons created in the strips) placed upstream and downstream of the target to monitor the proton intensity. These are usually called the target monitors the most commonly used one is the Target Monitor upstream (or TMU).

(b) Septum monitors

Before and after the septum there is a set of SEM's to monitor the horizontal beam profile of the 400GeV/c protons.

(c) At the beginning and end of the decay tunnel

A set of horizontally and vertically aligned SEM's to monitor the hadron beam profile at the beginning and end of the decay tunnel. The difference between the two profiles measures the beam divergence.

(d) In gap one

An ionization grid monitor to measure the profile in both dimensions, an ionization chamber to measure the intensity, and a secondary emission grid monitor again to measure the horizontal and vertical beam profiles.

CHAPTER 5

FLUX PROGRAMS

As mentioned previously, the narrow band beam requires continuous monitoring to ensure its stability and positioning. This is done on-line with the aid of the NFM (Neutrino Flux Monitoring) on-line program. The final flux analysis is best done off-line with the raw data tapes written by the on-line program as input. The off-line program must serve two main functions; to sum the flux for any specified period of time; and to calibrate the detectors to determine whether any have gone bad due to radiation damage.

The present chapter describes the on-line program and its use, and the authors' work on the off-line program which has been his main preoccupation until the writing of this thesis.

5.1 ON-LINE PROGRAM

Since the on and off-line programs have many features in common we only describe here the main functions of the on-line program and leave the detailed description of the common purposes of the two programs to later in this chapter.

The main functions of the on-line program are to collect the data from the various beam monitors and to provide the user with a facility to monitor the conditions of the beam so that he may take corrective action if some element of the beam-line becomes faulty or the beam is incorrectly adjusted.

The information which the on-line program writes onto tape arrives on a pulse by pulse basis from various sources. The proton beam information coming from the SPS monitors placed around the

target is sent to the Narrow Band Computer (NBC) situated in the BA7 control room which contains the power supplies for the beam line. From there it is sent to the NFM where it is written onto tape along with the information concerning the magnet currents in the beam line, which is also assembled in BA7. The muon flux information from each gap is also written onto tape every pulse and stored on disk for interactive use by the user. The reader is referred to the list of references at the end of this chapter for a detailed description of the data blocks and their contents.

As described previously, each gap is provided with a set of five detectors of differing sensitivity, capable of measuring the full range of the flux, mounted in a moveable box. This box serves two main functions; to provide a continuous calibration facility for the fixed detectors in each gap; and to provide the user with a profile of the muon distributions in each gap. In the WA19 experiment the whole system was new, and the movement of the box had to be controlled by the user. For the WA47 experiment, some two years later, the so-called calibrations and scans were instigated automatically by the system every eight hours, and flagged on the tape with a bitted word which describes the status of each gap (viz. scan or calibration, one bit per gap). The user has the opportunity of monitoring the profile for circular and radial symmetry and centring. This information is also available on a pulse by pulse basis via a TV screen which is continuously updated by the program, and displays the ratio of the flux in the 15 cm ring to the central flux (aconstant for given beam conditions) in each gap, and also the 'centre of flux' in centimetres in both the vertical and horizontal directions. For good beam centring this should be minimum. For convenience we record here that the ratio 15/0 (i.e. the average of the 15 cm ring flux to the central flux) in gap two, with the on-line calibrated detector sensitivities is .42 in neutrino and .39 in antineutrino. This difference is due to the smaller proportion of muons from K-decay in anti-neutrino, and will be investi-

gated further in the next chapter.

Besides providing the interactive facility for profile monitoring the on-line program also has the task of writing the so-called layout files onto tape. This file contains all the data about each detector, namely its identifier (a three digit number which labels each detector individually), its position (gap and coordinates with respect to the plate), nominal sensitivity, and gain of the amplifier connected to that detector. This latter number is computed automatically by the program at the start of a run, when the nominal fluxes are entered for the ensuing running conditions. The gain clearly does not have to be as large in wide-band or neutrino running since the muon flux per proton incident on target is larger. The program also writes a special block in narrow band running which gives the position of the plate in the gap. This is necessary since, as was seen in chapter 4, the wide-band and narrow band axes are displaced with respect to each other by some 20 cm horizontally and vertically.

The data from the beam monitors are written onto tape for every pulse in which the muon intensity in the centre of gap two exceeds a certain threshold, which is determined from the running conditions, and also if the timing of the beam is within a certain tolerance. Provided these conditions are met, the BEBC flashes are triggered and a photograph is taken.

5.2 THE OFFLINE PROGRAM

The offline program has two chief objectives; the summing of the flux for any detector and any specified period of time; the calibration of each detector, and the calculation of new sensitivities when new detectors are introduced into the system. This procedure is illustrated diagramatically in Fig. 5.1. Owing to the large flow of data in the neutrino experiment (some 30 master tapes were filled for WA47 alone)

the program was written using the HYDRA[4] system of data storage. This is an extremely economical method of data storage, since the data is only resident in core (computer memory) until it is no longer required. A conventional system of dimensioned arrays must be resident in core for the duration of the program run and hence is less efficient in memory usage. This chapter deals only with the general operation of the program, and the reader is referred to the references at the end of the chapter for a detailed description of the data structure and routines of the program (ref 5.3)

5.2.1 FLUX SUMMING

For both branches of the flow diagram Fig. 5.1, the program consists of two units, the sum-tape creation; and sum-tape reading units. The sum-tape creation may be summarised by fig. 5.2, which, apart from the flushing out of the data, is the same for the summing and calibration tape creation programs.

When the HYDRA input routine reads a logical record off the NFM master tape, the data is communicated to a specified routine depending on the logical record identifier. Each of these routines treats a specific block of data namely:

(i) Detector off-sets

(ii) Detector flux for a given pulse

(iii) Sensitivities and gains

(iv) Detector layout

(v) Plate reference co-ordinates

(vi) NBC data (Magnet currents etc.) (NBB only)

(vii) Horn and reflector currents

Data blocks (i), (iii), (iv) and (v) arrive only rarely and hence the latest set of data are used by the program for flux computation. This

of course, arises naturally since the data are stored in common-blocks, thus any subsequent calculations are done on the latest layout information.

The routines treating data blocks (ii), (vi) and (vii) also perform the task of summing the data, (e.g. muon flux, protons on target, horn current, etc.) and flushing out the data in HYDRA format, when any one of several conditions are met. These are:

(a) End of BEBC or GARGAMELLE quarter roll (1500 pictures).

(b) End of file on input tape.

(c) Total of 100 accelerator pulses has been summed into the HYDRA bank structures.

in the scan-tape creation program, there is only one requirement:

(a) Flux summed when the CALBOX is stationary in all gaps. The data are flushed when the calbox is found to be moving in any gap, and not after 100 pulses.

This last requirement is usually correlated with the Calbox being situated in front of a fixed detector, but this need not be the case, since there are many scans with fine spacing between measurement points (3 cm or 5 cm).

The summing branch of the program is in the form of a set of user routines which may be optionally selected with the usual PATCHY selection methods. These routines allow the user to sum the fluxes on the sum-tape for any desired period of time, and to look at the beam stability and targeting conditions, by making various crude profile plots using the fixed detector fluxes and plotting the flux per proton for given sign selection.

The program requires a set of 'titles' as input which are the sensitivities of the detectors used during the run. These sensitivities are determined by first running the calibration routines on the scan tapes.

5.2.2 DETECTOR CALIBRATION

The bank structure of the calibration and summing programs is shown in Fig. 5.3.

For each fixed position of the calibration box, the program saves the five voltages of the box and the voltage (gain and sensitivity) of the fixed detector at that position if there is one. If the reference box is in the gap under consideration the program hangs another bank of information onto each position bank, filled with the relevent refbox data. The voltages written into the banks are the average voltages over the period of time the calbox was in that position. This bank structure is created for every scan and calibration, processed by the 'play' program, the results stored, and the whole structure is then dropped (i.e. HYDRA is then allowed to read in the next calibration or scan and create a new data structure). The 'play' program allows the user to perform three essential tasks.

(i) LINKING OF FIXED DETECTORS TO CALIBRATION BOX

As already described, the philosophy of the muon flux measurement of the total flux depends upon calibrating each detector to one chosen detector which is then calibrated absolutely with a nuclear emulsion. The scan tape analysis programs do this through the following method.

For each position of the calbox situated at a fixed detector location, the program computes the average flux of the detectors in the calbox which were in voltage range ($.5<v<9.0$), weighted by the square of the voltage on each detector i.e. it computes $\langle F_c \rangle$ given by

$$\langle F_c \rangle = \left\{ \sum_{i=1}^{5} (V_i^2) \quad \frac{V_i S_D^i}{\sigma_i} \right\} \Big/ \left\{ \sum_{i=1}^{5} (V_i^2) \right\}$$

where

V_i is the voltage of the i^{th} detector
S_D^i " " sensitivity " " "
G_i " " gain " " " "

V_i is computed using the latest off-set as already described. The programmethen computes the deviation of each calbox detector with respect to $\langle F_c \rangle$ and also the deviation of the fixed detector flux with respect to $\langle F_c \rangle$.

The linking of the fixed detector to the calbox is then achieved by adjusting the sensitivity of the fixed detector so that its deviation is zero with respect to $\langle F_c \rangle$ assuming the flux in the calbox is equal to the flux in the fixed detector. It was found that this cannot be done to better than 2% for any given calibration, and therefore we conclude that the error in the electronic muon flux measurement system is of order 2%. This must be taken into account when summing the flux for any experiment.

The linking is usually done to one detector in the reference box. This is done by calculating the value of $\langle F_R \rangle$ in the same way as for $\langle F_c \rangle$. The ratio:

$$R = \frac{\langle F_R \rangle}{\langle F_c \rangle}$$

per gap is then used to calculate an S_D for each detector with respect to the reference box, thus only leaving the overall calibration factor equal to

$$R^{abs} = \frac{\langle F_R \rangle^{abs}}{\langle F_R \rangle^{measured}} \quad \begin{matrix} (\text{true } \mu) \\ (\mu + \delta) \end{matrix}$$

to be determined from the emulsion. This of-course assumes that R^{abs} is independent of position in the shielding. This is certainly not true, and therefore position dependent correction factors must be applied to account for e.g. δ-ray variation as a function of position. This

analysis is still under investigation. Chapter 6 describes one method used by the author in an attempt to do this for the Narrow band experiment in gap 2.

An important remark must be made concerning the voltage cuts. The response of a detector to a given flux is only of the linear form given by equation (4.2), when the voltage of the detector is above a minimum value and below a maximum value. This may be seen from fig. 5.4 which shows the variation of detector signals in the calibration box in gap 2 as a function of radius in the gap.

For this reason one usually applies 'safe' voltage cuts of $.5<V<9.0$ or even $1.0<V<9.0$ for some applications.

(ii) CALCULATION OF NEW SENSITIVITIES

The calculation of the sensitivity of a new detector introduced into the system is carried out in essentially the same way, from the formula

$$\frac{V^{new} S_D^{new}}{G^{new}} = \langle F_c \rangle$$

where the symbols have their usual meanings. The S_D of the detector is calculated over many calibrations (say one ten day period) and the average is entered into the on-line table of detector sensitivities.

The above two applications of the sum program are generally only used at CERN to provide the user with a calibrated set of detector sensitivities for use in the calculation of total fluxes.

(iii) MUON PROFILE MEASUREMENTS

With a slight modification the program will print out the flux

in any specified detector. In particular the average calbox fluxes as a function of position are printed out for those scans which have fine spacing e.g. 3 cm or 5 cm. An analysis of the flux scans for the WA47 experiment is presented in the next chapter.

In wideband experiments, this is clearly of great importance since the muon flux profiles as a function of depth in the shielding must be fitted with the production spectrum and horn parameters to predict the neutrino energy spectrum. We now proceed to describe some simple analysis done by the author with the off-line flux analysis program.

5.2.3 CALIBRATION BOX EFFECT

The calibration box detectors are mounted in an aluminum box itself mounted on a large gantry. The muons passing through the box and gantry create a spray of electrons with unknown energy and angular distribution. This spray creates additional charge in the fixed detectors during calibrations and hence when the linking routines are used, the sensitivity of the detector is under-estimated due to this effect.

This effect was investigated by comparing the fixed detector signal with calbox infront of the detector and calbox in the 'garage' (completely away from the fixed detectors). The ratio of these two numbers directly measures the spray effect and is different for different fixed detector positions. The correction matrix for this effect is displayed in Fig. 5.5. Clearly the fractional error on this correction is large since the inherent system error is of the same magnitude as the correction.

This effect could also influence the total flux measurement due to the calbox being infront of the detectors for some of the time. This effect has been investigated by comparing the flux per pulse for

100 pulse sum records where there was a scan or calibration against those where there was no scan or calibration. For constant targetting conditions the effect was seen to be less than .5% in narrow band and is therefore ignored in the total flux computation.

CHAPTER 6

MUON FLUX ANALYSIS AND THE K/π RATIO

This chapter describtes the authors' work on the analysis of the muon flux data obtained with the summing program described in the previous chapter, and his attempts to obtain the K/π production ratio from this and other sources. We begin with a description of the monte-carlo simulation programs of the CERN WANF narrow band beam.

6.1 MONTE-CARLO PROGRAMS

At present, there are two programs available for Monte-Carlo studies of the beam line which are mutually complementary namely TURTLE[1]; and DISMUNU The former traces the parent particles from the target through the magnetic beamline and tracks all the muons from π and K decay in the beam line and decay tunnel through the shielding to the measurement pits including multiple scattering and energy loss in the iron. The neutrinos are also tracked from the decay point to the position of BEBC, enabling their energy spectrum and radial distribution to be plotted. The beam line is set up in detailed form by inputting the position, aperture, length and magnetic field configuration of all the bending magnets, quadrupoles, and slits in the form of data cards. By generating π's and K's over a sufficiently wide production angle and momentum range (0-4 mrad and 170-230GeV/C were used) the parameters of the parents may be obtained at the beginning of the decay tunnel (momentum spread, divergence). Since this program was originally intended to simulate the parent propogation in a magnetic beam line the properties of the parents as they enter the decay tunnel are fed into the program DISMUNU at this point. In theory the TURTLE muon distributions in gap 2 could be used, but were found to give very poor agreement with the data, especially at small radii.

In order to determine these parameters the TURTLE program was used to calculate the acceptance of the NBB as a function of production angle and momentum, π's are generated at the angles displayed in Fig. 6.1 and the number of π's reaching the decay tunnel at each momentum as a fraction of the number of π's generated at that momentum is plotted. Fig. 6.1 shows that the acceptance is constant out to 2 mrad and falls dramatically for momenta $\pm 6\%$ either side of the design momentum.

The program DISMUNU therefore uses the known production spectrum and generates π's and K's at 200GeV/C $\pm$ 6% and 0 - 2 mrad at the beginning of the decay tunnel. The program then follows the parents as they decay and predicts muon fluxes in the gaps and event rates in the bubble chamber with the known fiducial volume, chamber liquid density and muon momentum cut.

6.2 ABSOLUTE CALIBRATION

In the WA47 experiment the absolute calibration of the fixed detectors in gap 2 was performed with two emulsions placed at 0cm and 30 cm on the horizontal bar at 180° (See fig. 4.6). The 0 cm emulsion was exposed for 4 SPS pulses and the 30 cm one for 20 pulses.

In both cases the emulsion was positioned upstream of the refbox and was mounted perpendicular to the beam. The refbox and calibration box were down stream of the emulsion at both radii.

On developing the emulsion sheers due to shrinkage, and straight through tracks acquire the same distortion features. When the emulsion is scanned therefore, care must be taken to ensure that in the regions scanned the tracks have the same sheer and should preferably be as short as possible (See fig. 6.2). The tracks appear through a microscope to be dots moving across the field of view when the focal point of the microscope objective is moved up and down. All tracks which traverse the whole thickness of the emulsion are drawn on a scan sheet provided with linear

graph paper so the positions of the beginning and end points of each track may be measured. In order to calculate the muon flux per square centimetre the area of each field of view must be known. For the microscope used in this experiment this was $79 \times 79 \mu^2$.

The data from thescan sheets are run through a program which uses the thickness of the emulsion and microscope magnification factors to calculate the angular distribution of the tracks. The sheer is assumed constant for all the field of view. The program calculatesthe axis through the emulsion which makes the distance between the entry and exit points of the majority of the tracks a minimum. The angular distribution of the tracks about this axis is then computed. These distributions are shown for both emulsions in figs. 6.3 and 6.4.

The tail in both plots is attributed primarily to the delta ray background with energy greater than ~2MeV, sufficient to penetrate the emulsion. These came from the shielding and are scattered in the air between the shielding and the solid state detectors. This constitutes a background under the muon peak in the fist few bins and must be subtracted. The background calculation was performed with a monte-carlo of the electromagnetic cascade in the shielding due to Burmeister[1]. The curve displayed is this background normalised to the background signal beyond .001 in bins of $1-\cos\theta$, where θ is theangle of the tracks with respect to the fitted axis.

Since a precise knowledge of the background cannot be expected from the monte-carlo program due to the unknown straggling, (fluctuations in the energy loss of the electrons in the shielding) and scattering in the air in the gap, the subtraction was given a 100% error. This gave the delta ray background in the bin 0-20 mrad as 12.1% at 0cm and at 30cm.

The scanning inefficiency was estimated by a complete independent re-scan of the same emulsions as 10%. Due to this the absolute calibration of the detectors was not done with these emulsions, however they were used to determine the δ-ray variation across the gap as will now be described.

6.3 MUON PROFILE FITTING

In principle, the charged hadron ratio may be determined from the muon profiles in the gaps. This may be done provided the backgrounds are subtracted out, in particular the δ-ray contribution to the flux at each position in the gap must be known, and the number of muons reaching the gaps from decays in the magnetic beam line must also be determined. We describe in this section the method used by the author to obtain the true narrow band muon flux signal in gap 2.

6.3.1 DELTA RAY SUBTRACTION

It is clear that the only way to measure the δ contribution to the flux signal is to expose emulsions at each position and measure the number of muons at each point. Since this is not practicable (the emulsions would take a very large number of man-scanning hours!) a means of doing this electronically was found. The method employed here, is to use the calibration box in over out (I/O) curves described in chapter 5. The ratio I/O may be expressed as

$$\frac{I}{O} = \frac{f.\mu + g.\delta}{\mu + \delta} = R \text{, say}$$

where μ and δ are the muon and δ fluxes at any position and f,g are functions which describe how the μ's and δ's create spray. Clearly, these two functions depend on the energy distributions of the μ's and δ's and in general cannot be expected to be the same. In particular the δ-ray energy distribution is peaked to much lower energy than the muon energy distributionand hence the δ's are much more likely to be scattered out of the box than produce spray. However, the δ ray spectrum is completely unknown at present and the best one can assume about the muon factor f, is that it is a constant. For the present analysis we assume that the μ and δ energy distributions do not vary significantly with radius, then

$$\frac{\mu}{\mu+\delta} = \frac{R-g}{f-g}$$

where f and g are assumed to be independent of radius.

Using the calbox effect already calculated from chapter 5, we calibrate these curves so that the proportion of δ's at 30 cm divided by the proportion of δ's at 0 cm is the same as that given by the absolute calibration. This curve is displayed in fig. 6.5 with the δ contribution at 0 cm arbitrarily fixed to zero. The overall normalization of the curves does not matter in this analysis, since all fluxes will be normalised to the 15 cm flux for reasons to be explained later.

6.3.2 THE TRAPPED μ SUBTRACTION

The term 'trapped ' refers to those muons which come from parent decays before and after the collimator and are transported through the beam line to the measurement pits. The proportion of μ's in gap 2 which are trapped μ's has been calculated with the TURTLE program by flagging those muons which reach gap 2 and originate in decays before the decay tunnel.

This proportion is different for π 's and K's as is to be expected since the K has a larger mass. The numbers have been combined with a K/π ratio of .144 as measured by the Čerenkov. This presumes the answer being sought but is insensitive to the K/π ratio as displayed in Fig. 6.6. The result also depends on the spectrum used at production. The spectrum given by the North Area measurements (examined in greater detail later) was input to this calculation and is displayed in Figs 6.11 - 6.14.

The trapped μ results were checked by comparing the TURTLE results for closed collimator with the closed collimator running during the WA47 antineutrino running. These are displayed in Fig. 6.7 and are clearly in good agreement with the experimental data. This gives support to the trapped μ calculation with TURTLE, though the turtle muon distributions themselves do not agree with the data for open collimator. For this reason, the trapped muon results were given a 2% error on all data points.

The trapped μ correction results are shown in fig. 6.6.

6.3.3 PROFILE FITTING

Using the flux summing program, several scans of the calbox were summed from the NFM tapes. Since the targetting efficiency was unknown, all profiles were corrected for the δ-ray and trapped μ effects and then normalised to the 15 cm flux. The resulting statistical spread was then 2%, the system fluctuation error. All the scans were then averaged and two profiles obtained, one for positive parents and one for negative parents.

The fitting of the profiles involves two parameters; the beam divergence; and the K/π ratio of the parents in the beam. These parameters cannot be fixed both at the same time since a large beam divergence requires a smaller K/π ratio to fit the same distribution. This is because a large beam divergence means a broader distribution and since the K muons are the only contribution to the flux beyond 45 cm in gap the number of K's required is clearly smaller. This is made quantitative

in fig. 6.8 which shows the effect of varying the beam divergence on the fitted K/π ratio. These curves were obtained with the program DISMUNU. The beam divergence therefore, was first fixed by fitting the region 0-15 cm with a K/π ratio given by the Cerenkov ($K/\pi = .1446(\nu)_1 .047(\bar{\nu})$) and was .17. This number was checked with TURTLE by plotting the angular distribution of the parents at the end of the magnetic beam line. The average of the vertical and horizontal divergences was .21, in rough agreement with the profile fitted number.

Having fitted the small radius region the large radii were fitted by a minimum χ^2 method by varying the K/π ratio. The result of the fit is shown in fig. 6.9. Also shown are the theoretical curves obtained when the χ^2 increases by one unit from its minimum value, corresponding to the 64% confidence level error. These curves verify that fitting the beam divergence at small radii with a constant K/π ratio is independent of the K/π ratio used since all the curves lie ontop of each other for radii less than $\sim$20 cm.

Fig 6.8(b) shows the results of the fits obtained with various beam divergences. The table displays the χ^2 of the fit and the corresponding K/π ratio and error as a function of the beam divergence. The best value is:

ν: $K/\pi = .137 \pm 9\%$ beam divergence $= .17$ mrad.

$\bar{\nu}$: $K/\pi = .070 \pm 8\%$ beam divergence $= .13$ mrad.

6.4 CERENKOV MEASUREMENTS

The best method of measuring the K/π ratio is with the differential Cerenkov at the beginning of the decay tunnel. By varying the pressure in the detector the particle ratios may be measured by integrating the corresponding curve in the light intensity versus pressure plot. One such curve is shown in fig. 6.10. These plots were made at various times during the WA47 run with different Cerenkov conditions. The averaged ratios are:-[2)]

$$\left.\frac{K^+}{\pi^+}\right|_{\nu} \simeq .144 \pm .004 \qquad \left.\frac{K^-}{\pi^-}\right|_{\bar{\nu}} = .047 \pm .002$$

At the time of writing the p/π ratio is subject to uncertainty since the number of protons measured by the calorimeter at the end of the decay tunnel does not agree with the Cerenkov numbers. It is felt that this is a problem with the calorimeter and that the cerenkov particle ratios are correct. However, it is still important that these numbers are checked by as many independent methods as possible.

6.5 North Area Measurements

The production spectrum of π's and K's has been measured with a spectrometer in the CERN North Area beam lines at 60, 120, 200 and 320GeV/C π and K momentum with a 400GeV/C proton beam incident on a beryllium target with the same dimensions as the narrow band beam target. The resulting spectra are shown in fig. 6.11 - 6.14, the measurement points are indicated with circles. Given the acceptance of the NBB these measurements are clearly not sufficient by themselves to determine the K/π ratio at the beginning of the decay tunnel since this depends critically on the interpolation used between the data points. The curves shown are thermodynamical model type curves adjusted so they pass through the measurement points.

The K/π ratio was determined from these curves by inputting the spectra into the TURTLE program andapplying various interpolations in angle to obtain some idea of the K/π ratio. All interpolations were in $\ln d^2N/dpd\Omega$ and are shown in fig. 6.15 together with the K/π ratio obtained. The values are consistent with the cerenkov numbers for positives. Since there is a large spread on the answers no attempt has been made to obtain the K/π ratio for negatives.

6.5 CONCLUSION

The results on the K/π ratio and beam divergence are clearly dependent on the method used to subtract out the delta-ray background. Conventional wisdom, based on Quantum Electrodynamics, states that the δ-ray flux distribution should be a constant fraction of the total flux measured and this fraction should should be independent of radius. The fact that the two emulsion exposures during the WA47 running give a different muon flux per coulomb in the calibration box at $\emptyset$ and $3\emptyset$ cm is in complete contradiction to this assumption, and shows that there must be some 'washing out' of the δ-rays by scattering in the air in the gap.

The method used by the author to obtain the δ-ray distribution rests on assumptions which must be clearly false given that there is multiple scattering of the δ's between the end of the shielding and the detectors. However the present method is the only one available unless all detectors are calibrated by emulsion, a feat which would require $\sim$ 1 man year to accomplish. The results of the profile fitting must therefore be treated with skepticism and viewed only as a check of the other beam monitors which give results for the same parameters.

Within these qualifying statements therefore, one may state that the muon flux profiles are not inconsistent with the values.

$$\frac{K^+}{\pi^+} = .144 \quad , \quad \frac{K^-}{\pi^-} = .047$$

Beam divergence = .20 mrad

For the cross-section analysis of chapter 7. We assume these values to be the correct ones.

CHAPTER 7

ANTINEUTRINO TOTAL CROSS-SECTION

We present the results available so far on the total cross-sections for WA47. To date the physicist checked DST's contain only the antineutrino data, thus only the antineutrino cross-section is calculated here. Without the neutrino cross-section tests of the Callan-Gross relation and measurement of the anti-quark content of the nucleon are not possible. However, the linearity of the energy dependence of the antineutrino cross-section tests the scaling hypothesis, we therefore present this analysis here.

7.1 NEUTRAL ENERGY CALIBRATION

Due mainly to the complexity of the high energy events in the 200GeV/C beam the total neutral energy of any event cannot be completely measured since some is lost in the hadronic shower and some entirely escapes from the chamber without converting in the liquid. The neutral energy loss has been investigated by two different methods:

7.1.1 P_T BALANCE

The average value of ε in the formula

$$E_\nu = \epsilon_\mu + E_m/\varepsilon$$

has been calculated which makes the distribution of $\theta_h - \theta_m$ in Fig. 7.1 centre on zero in each bin of hadronic energy. The measured hadronic energy is calculated from

$$E_m = \sum_{i=1}^{N} E_i - m$$

where N is the total number of hadronic tracks in the event and m is the mass of the nucleon. The value of ε is displayed in Fig. 7.2

for the complete range of hadronic energy measured in this experiment.

ε is clearly independent of E_h and has the average value $\varepsilon = .82 \pm .02$

ε has also been estimated by comparing the modulus of the momenta of the hadronic shower and the muon transverse to the beam direction. This method has shown that events from K decay are brought onto the kaon peak expected from Monte-Carlo studies of the beam line. The value of ε is consistent with the value of ε obtained from the previous method.

7.1.2 70GeV/c π^- INTERACTIONS

A special exposure of BEBC (filled with the same 74% molar NeH_2 liquid) was made during the WA19 experiment with 70 GeV/c π^- particles. More exposures were made during the WA47 experiment at several other incident pion beam momenta. The events were measured by the same method as the neutrino events and the fraction of the event energy measured was plotted. The result is shown in Fig 7.3. The average correction factor is consistent with that obtained in the balance method.

The average event correction factor of 1.2 was thus applied to all measured hadronic energies for neutrinos in the pion peak. Events with energy larger than the maximum ν_π energy at the event radius in the chamber were given the nominal ν_K energy for that radius.

7.1.3 FIDUCIAL VOLUME CUT

Only events within the fiducial volume indicated in Fig. 7.4 were included in the total event numbers. This region was chosen to give a minimum measurement length of 50 cm for leaving tracks to be extrapolated to the EMI. A cut in z (vertical distance from the centre of BEBC) of $\pm$ 100 cm on the vertex position of the event was also made to remove events for which the muon could potentially miss the EMI due to being too high in z. A backward cut on the horizontal radius of the

vertex of the event was imposed, to remove all events which could have been unnoticed interactions in the wall of the chamber.

7.2 EVENT NUMBERS AND CORRECTIONS

The raw number of events found on the DST was 433. This raw event number was corrected for various effects:

(i) Isoscalarity

The neutron to proton ratio with the 75% molar mixture of NeH_2 is 0.93. Thus

$$\frac{\sigma(Ne\,H_2)}{\sigma(\text{Isoscalar})} = 1.012$$

therefore the cross-section was decreased by 1% to refer to an isoscalar target.

(ii) EMI inefficiency

Since the muons from charged current events are required to give a two plane hit in the EMI an upward correction of 5% was made to account for EMI electronic inefficiency. (Both planes were assumed to have the same inefficiency of 2.5%). In addition the geometrical inefficiency of the inner plane was estimated by counting the number of muons which only gave hits in the outer plane. In a sample of $\sim$400 events only three missed the inner plane in positive focussing conditions, (i.e. neutrino beam). Thus we assume here that this was a negligible effect in antineutrino since the y distribution favours the production of energetic muons in the forward direction and very few are expected to miss the inner plane.

(iii) Magnetic Beam line decays

Using the TURTLE monte-carlo program the proportion of the neutrino flux due to decays in the magnetic beam line has been calculated. Since the beam is pointing away from BEBC before the collimator, the neutrino flux from before this point is expected to be small, and

the correction to the neutrino flux from decay after the collimator should be approximately independent of energy since this flux is already essentially narrow band flux. Fig. 7.5 shows the energy distribution ofthis flux, the total flux and the correction percentage. The percentage is indeed independent of energy and has a mean value of 3%. The relation between flux and event numbers is linear, therefore this fraction of the events was subtracted to give the true narrow band event number.

(iv) $K_{\mu 3}$ decays

2% of the events between 60GeV and 130GeV were subtracted to account for the decays $K^{\pm} \Rightarrow \pi^{0} \mu^{\pm} \nu(\bar{\nu})$. This correction is based mainly on the ratio of branching ratios

$$\frac{K^{\pm} \Rightarrow \pi^{0} \mu^{\pm} \nu(\bar{\nu})}{K^{\pm} \Rightarrow \mu^{\pm} \nu(\bar{\nu})} \sim 5\%$$

the decay kinematics, and the fact that roughly half of the events in this energy range are events from K decay.

The energy distribution of the events in the bubble chamber after these corrections is shown in Fig. 7.6, with a muon momentum cut of 5 GeV/C.

7.3 THE TOTAL FLUX

As has already been seen in chapter 6 the muon flux depends critically on the beam divergence. This may be reduced by measuring the flux at 15 cm in gap 2, since all the beam divergence curves intersect at ~17 cm. The muon flux was therefore summed for the 15 cm ring in gap 2 for the whole of the antineutrino running using the sum program of chapter 5.

In practice this is done roll by roll by multiplying the flux per NFM pulse by the number of scanned BEBC photographs for which all the

information required to measure the total cross-section was available. This condition requires that:

(a) the film be measurable on at least two views,

(b) the NFM was working and the beam was giving narrow band flux,

(c) The EMI was working and taking data.

The total uncorrected flux in antineutrino beam for WA47 was then

$$\sum \mu = 13.9 \times 10^{8} \mu/cm^{2}$$

averaged over the eight detectors of the 15 cm ring. This raw flux was then corrected for the following:

(i) absolute calibration of the ring detectors with the calibration box (linking) and emulsions,

(ii) δ - ray contribution at 15 cm,

(iii) beam trapped muons at 15 cm,

(iv) spray effect of the calibration box during calibrations.

the errors on these corrections are: absolute calibration 3%: linking 2% delta rays at 15 cm 4%, beam trapped muons 2%, spray effect 2%, giving an overall flux error of 6.1%.

After corrections for these effects the number of corrected events with $E_\mu > 20$GeV and $p_\mu > 5$ GeV/C per corrected flux was

$$\beta = 36.6 \pm 3.04$$

where we have included a 50% error on the EMI inefficiency and wide-band background corrections, as well as the statistical event error and the flux error. A 1% correction has been made to account for scanning inefficiency.

7.4 ANTINEUTRINO CROSS-SECTION AS A FUNCTION OF ENERGY

In order to calculate the total cross-section the measured number of events per 15 cm flux was divided by the Monte-Carlo number from DISMUNU, assuming the same neutrino energy and muon momentum cuts, a beam divergence of .20 mrad, K/π ratio of .047, bubble chamber liquid density of .67gcm^{-3}, and a total cross section given by

$$\sigma = E_\nu \ 10^{-38} \ cm^2 / GeV / Nucleon$$

The error on this number is determined mainly by the error on the beam divergence and also on the production spectrum. Fig 7.7 shows the variation in β for $E_\nu > 20 GeV$, $P_\mu > 5 \frac{GeV}{c}$ as a function of beam divergence. Since the beam divergence cannot be accurately pinned down by the muon profiles owing to the uncertainty of the delta-ray subtraction, we assume the maximum error on β is thus 2%.

Finally, the total antineutrino cross-section as a function of energy is displayed in Fig 7.8. An additional error of 10% should be included in the data point above 100 Gev to accomodate the uncertainty in the K/π ratio. No correction has been made for smearing in the neutrino energy in the pion peak.

7.5 CONCLUSION

The cross-section data presented in this thesis are consistent with the hypothesis of scaling but show a general trend to rise faster than the linear dependence predicted by scaling. The trend of the scale violating effect and the magnitude are both in agreement with the dependence predicted by Quantum Chromodynamics in which the violations are supposedly due to the higher energy neutrinos probing

the fine structure of the proton revealed by a large Q^2 intermediate vector boson.

The curves in Fig 7.8 show the prediction of QCD for two different values of the parameter Λ , which determines the Q^2 dependence of the strong coupling constant α_s through the relation

$$\alpha_s(Q^2) = \frac{12\pi}{25} \Big/ \ln\left(\frac{Q^2}{\Lambda^2}\right) \quad (SU4)$$

The data are clearly not accurate enough to distinguish between any particular value of Λ at this stage.

APPENDIX A

In the neutrino scattering depicted in fig. 2.1 the three kinematically independent lorentz invariant quantities may be chosen to be Q^2, x, y . Then equation 2.2 may be derived from equation 2.1 via the following argument.

The quantities $\sin^2\theta/2$ and $\cos^2\theta/2$ are given by

$$\sin^2\theta/2 = Q^2/4E_\nu E_l = \frac{2mE_\nu xy}{4E_\nu E_l} = \frac{mxy}{2E_\nu(1-y)}$$

$$\cos^2\theta/2 = 1-\sin^2\theta/2 = \frac{1-y-mxy/2E_\nu}{(1-y)}$$

and $$\frac{E_\nu+E_l}{m}\sin^2\theta/2 = \frac{E_\nu(2-y)}{m}\cdot\frac{mxy}{2E_\nu(1-y)} = \frac{xy(1-y/2)}{1-y}$$

The differential cross-section $\frac{d^2\sigma}{dxdy}$ must be evaluated by replacing ν with some other variable z say, and performing the differentiation with respect to this variable afterwards letting $z = \nu$. The result is

$$J = \begin{vmatrix} \partial^2Q^2/\partial x & \partial Q^2/\partial y \\ \partial z/\partial x & \partial z/\partial y \end{vmatrix}_{\substack{z=\nu \\ =E_y}} = \begin{vmatrix} 2mE_\nu y & 2mE_\nu x \\ 0 & E_\nu \end{vmatrix} = 2mxE_\nu$$

then the equation 2.1

$$\frac{d^2\sigma}{dQ^2d\nu} = \frac{G^2}{2\pi m}\frac{E_l}{E_\nu}\left[\cos^2\theta/2\ W_2 + 2\sin^2\theta/2\ W_1 \pm \frac{E_\nu+E_l}{m}\sin^2\theta/2\ W_3\right]$$

becomes

$$\frac{d^2\sigma}{dxdy} = \frac{G^2}{\pi}\nu E_\nu(1-y)\left[\frac{(1-y-mxy/2E_\nu)}{(1-y)}W_2 + \frac{mxy^2}{E_\nu(1-y)}W_1 \pm \frac{xy(1-y/2)}{(1-y)}W_3\right]$$

$$= \frac{G^2mE_\nu}{\pi}\left[(1-y-\frac{mxy}{2E_\nu})\frac{\nu}{m}W_2 + xy^2W_1 \pm xy(1-y/2)\frac{\nu}{m}W_3\right]$$

Equation 2.2 is recovered if we make the identification

$$F_1 = W_1$$

$$F_2 = \frac{\nu}{M} W_2$$

$$F_3 = \frac{\nu}{M} W_3$$

and we make the approximation that

$$\frac{MxY}{2E_\nu} \ll 1$$

which is valid for high energy experiments where $E_\nu \gg M$, so that the above relation becomes

$$\frac{d^2\sigma}{dx\,dy} = \frac{G^2 S}{2\pi}\left[(1-y)F_2 + \frac{y^2}{2}(2xF_1) \pm y(1-y/2)xF_3\right] \qquad (2.2)$$

APPENDIX B

The elementary cross-sections for scattering of neutrinos of spin one-half quarks and anti-quarks are

$$\frac{d\sigma^{\nu\bar{q}}}{dy} = \frac{d\sigma^{\nu q}}{dy} = 1 \; ; \; \frac{d\sigma^{\nu\bar{q}}}{dy} = \frac{d\sigma^{\bar{\nu}q}}{dy} = (1-y)^2$$

These relations are a consequence of helicity conservation. In the neutrino case there is zero helicity in the initial state and hence no angle dependence to the scattering cross-section. In the anti-neutrino case there is a net spin of -1 ($-\frac{1}{2}$ from the $\bar{\nu}$ and $-\frac{1}{2}$ from the anti-quark) in the direction of the incident neutrino beam. (See fig. B.1) and hence angular dependence of the form.

$$\frac{d\sigma}{d(\cos\theta^{*})} \propto (1+\cos\theta^{*})^2$$

in the centre of momentum system (CMS). By considering the dot product of the quark and final state lepton four vectors, one may show that the $(1+\cos\theta^{*})^2$ dependence is equivalent to the $(1-y)^2$ dependence.

The formulae 2.3 are then recovered by adding the elementary quark and anti-quark cross-sections with the centre of momentum energy given by

$$s = (xp_N + p_\nu)^2 \simeq 2Mx E_\nu$$

The consequences of the quark-parton model may be derived from the following argument, considering equation 2.3

$$\frac{d^2\sigma^{\nu N}}{dxdy} = \frac{G^2 s}{2\pi}\left[q(x) + \bar{q}(x)(1-y)^2 \right] \quad (a)$$

$$\frac{d^2\sigma^{\bar{\nu}N}}{dxdy} = \frac{G^2 s}{2\pi}\left[q(x)(1-y)^2 + \bar{q}(x) \right] \quad (b)$$

Relation (a) may be re-written by simple algebraic manipulations as

$$\frac{d^2\sigma^{\nu N}}{dxdy} = \frac{G^2 S}{2\pi}\left[(1-y)(q(x)+\bar{q}(x)) + \frac{y^2}{2}(q(x)+\bar{q}(x)) + y(1-y/2)(q(x)-\bar{q}(x))\right]$$

collecting terms in $q(x)$ and $\bar{q}(x)$ we recover relation (a). Hence by comparing terms in this equation with the neutrino scattering equation 2.2,

$$\frac{d^2\sigma}{dxdy} = \frac{G^2 S}{2\pi}\left[F_2(x)(1-y) + \frac{y^2}{2}(2xF_1(x)) + y(1-y/2)\,xF_3(x)\right]$$

we find,

$$F_2(x) = q(x) + \bar{q}(x) = 2xF_1(x)$$

$$xF_3(x) = q(x) - \bar{q}(x)$$

The first of those relations is the Callan-Gross relation for spin one-half scattering. It applies equally well in electro-magnetic scattering. Clearly, by interchanging $q(x)$ and $\bar{q}(x)$, the xF_3 term changes sign, as expected for anti-neutrino scattering on the basis of equation 2.2.

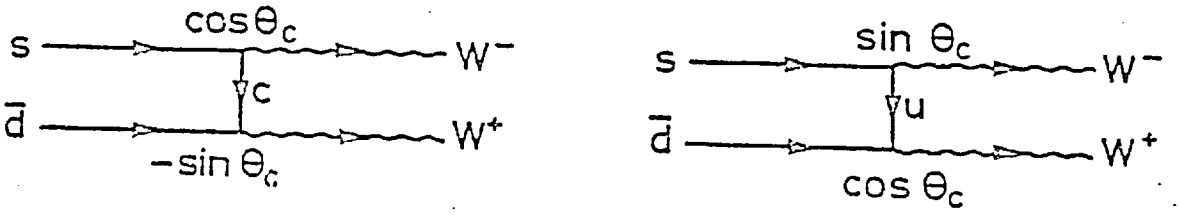

Fig 1.1

$$\begin{pmatrix} \nu_e \\ e^- \end{pmatrix}_L \quad \begin{pmatrix} \nu_\mu \\ \mu^- \end{pmatrix}_L \quad \begin{pmatrix} u \\ d_c \end{pmatrix}_L \quad \begin{pmatrix} c \\ s_c \end{pmatrix}_L$$

$$d_c = d\cos\theta_c + s\sin\theta_c$$

$$s_c = s\cos\theta_c - d\sin\theta_c$$

$$\tan^2\theta_c \simeq .05$$

Fig 1.2

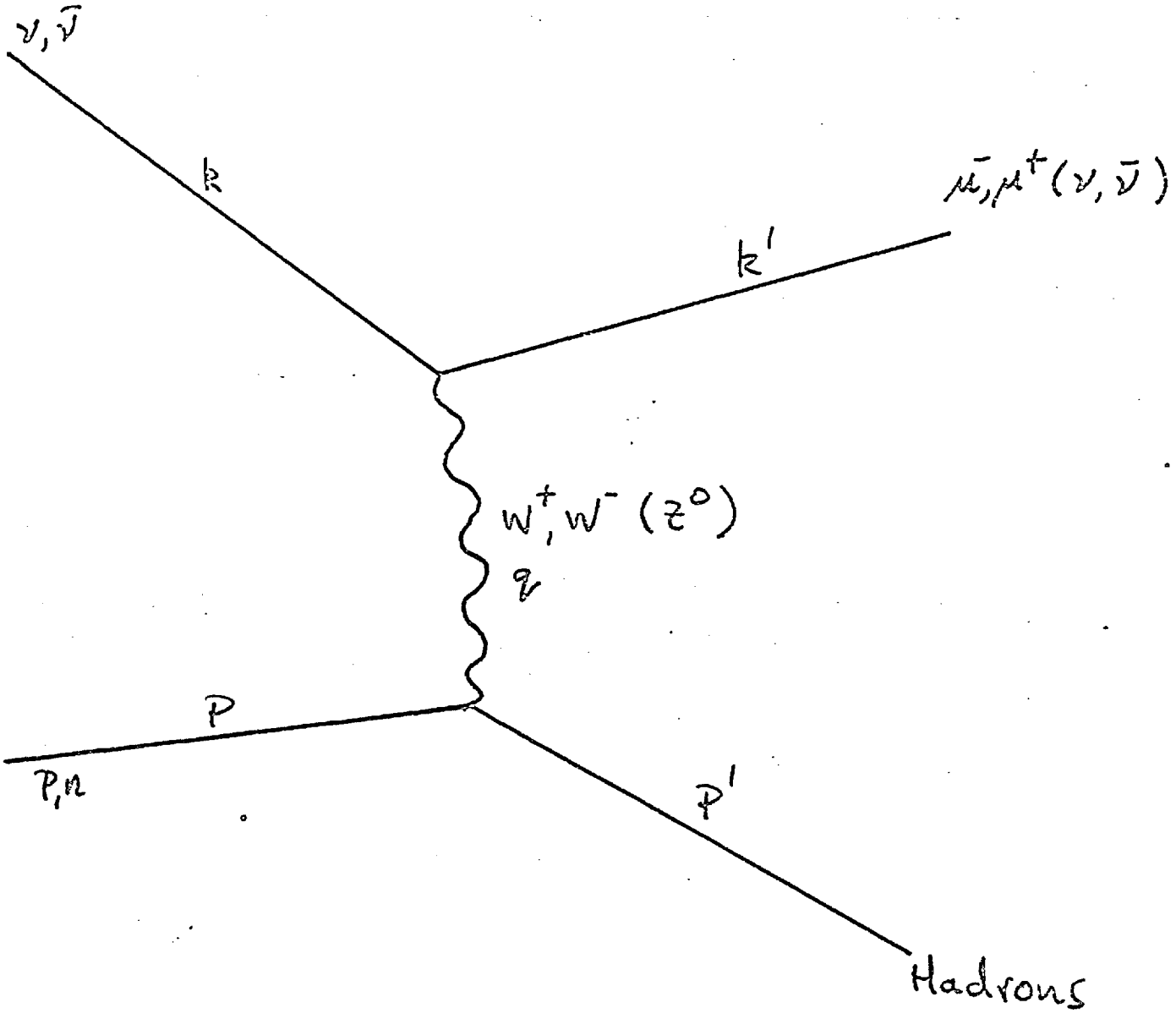

$k = (E_\nu, 0, 0, E_\nu)$

$k' = (E_l, \vec{P}_l)$

$p = (M, 0, 0, 0)$

$p' = (E_h, \vec{P}_h)$

Fig 2.1

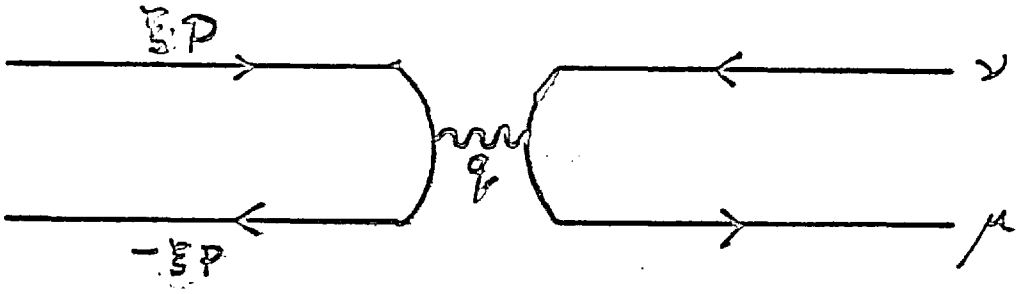

$$P = (P, 0, 0, P)$$

$$q = (0, 0, 0, q) \qquad q = 2\xi P$$

Fig 2.2

PROCESS	$\frac{d\sigma/dy}{G^2 m E/\pi}$
$\nu_\mu + d \to \mu^- + u$	$\cos^2\theta_c \, 2x$
$\bar{\nu}_\mu + u \to \mu^+ + d$	$\cos^2\theta_c \, 2x(1-y)^2$
$\bar{\nu}_\mu + \bar{d} \to \mu^+ + \bar{u}$	$\cos^2\theta_c \, 2x$
$\nu_\mu + \bar{u} \to \mu^- + \bar{d}$	$\cos^2\theta_c \, 2x(1-y)^2$

Fig 2.3

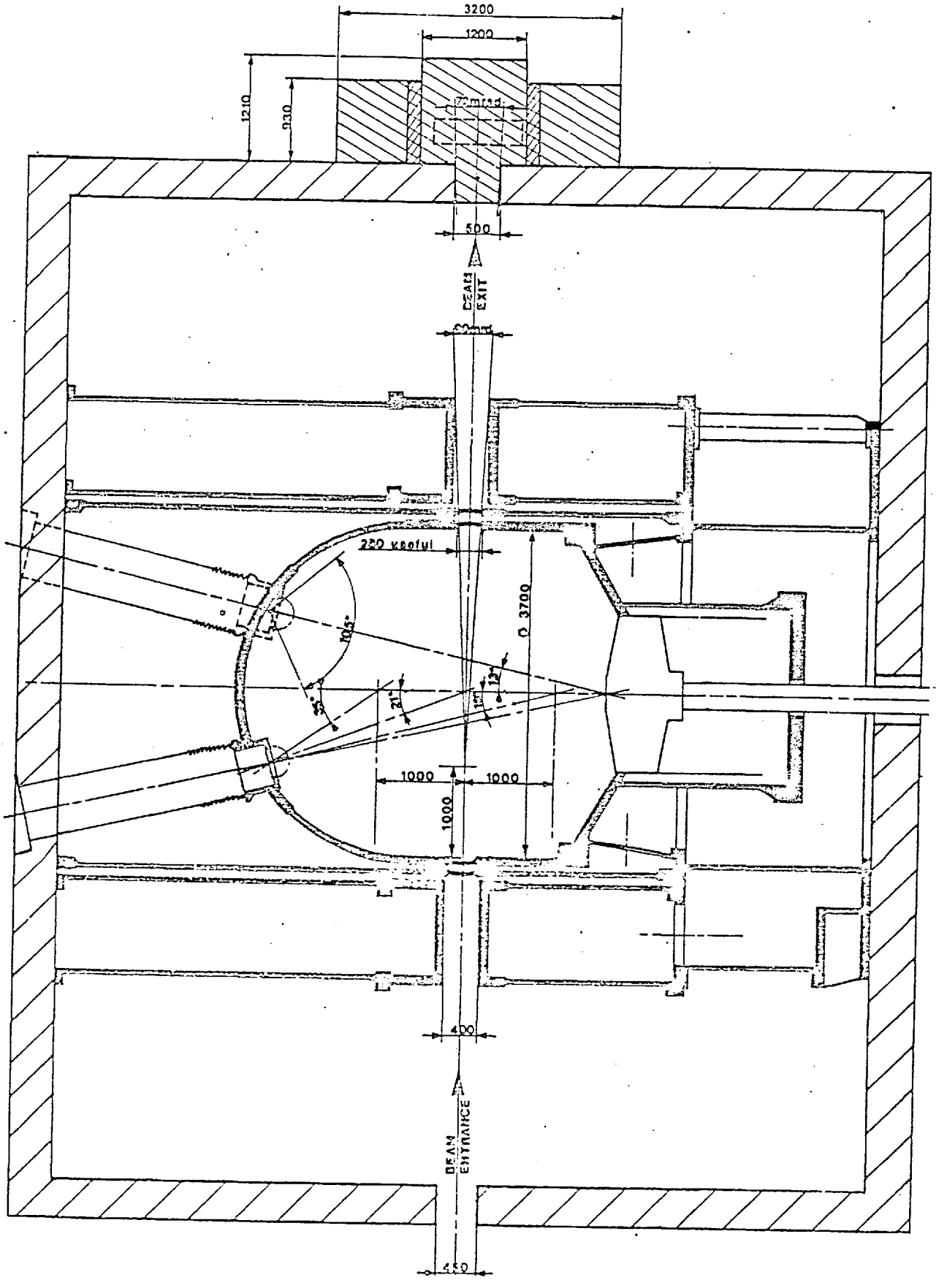
3200
1200
1210
930
500
BEAM EXIT
220 krafui
105°
Ø 3700
25°
21°
12°
1000
1000
1000
400
BEAM ENTRANCE
450

Fig 3.1

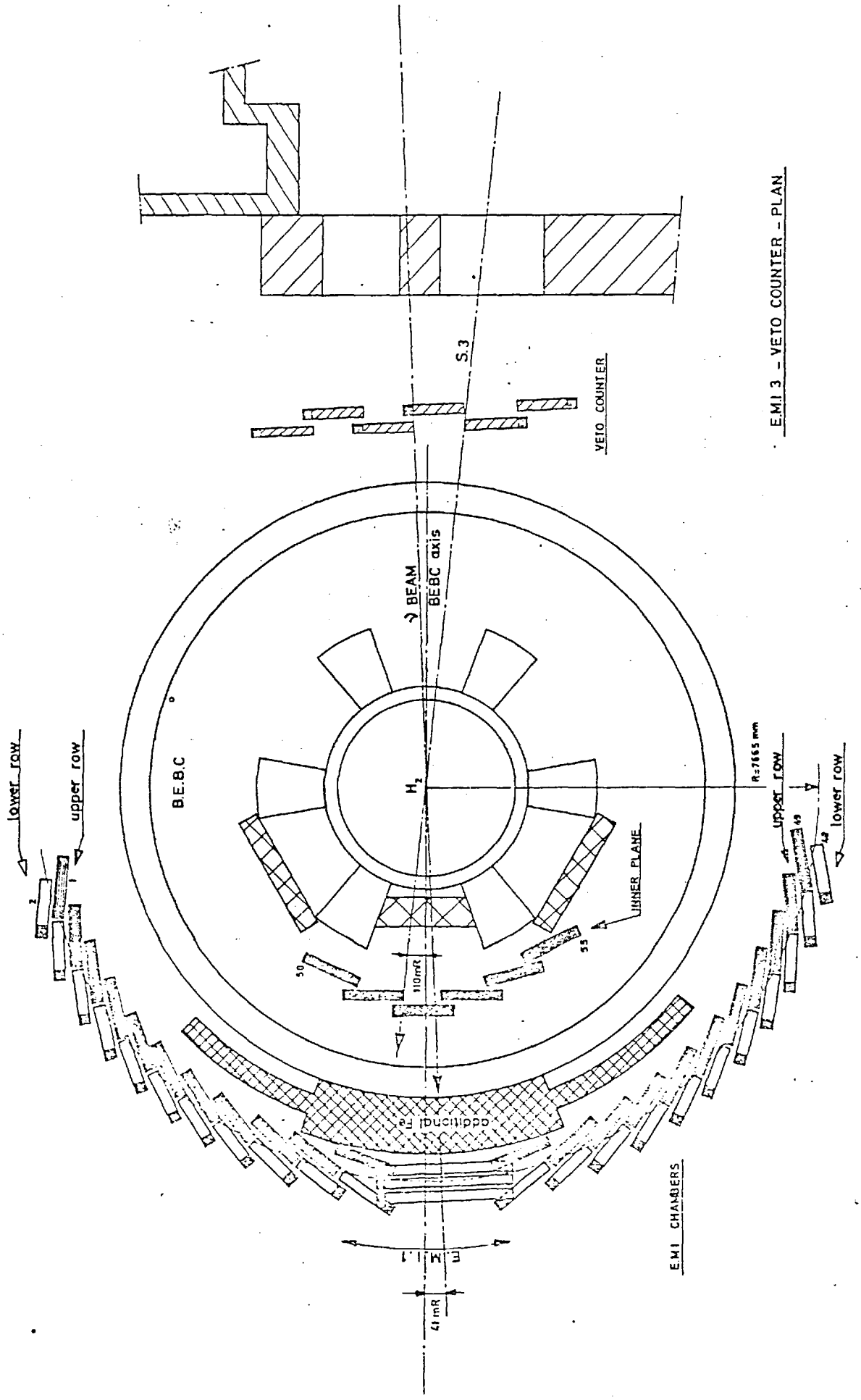
E.M.I 3 - VETO COUNTER - PLAN
S.3
VETO COUNTER
BEAM
BEBC axis
B.E.B.C
H2
R=7665 mm
INNER PLANE
110mR
41 mR
E.M.I. 1
E.M.I CHAMBERS
lower row
upper row
upper row
lower row

Fig 3.2

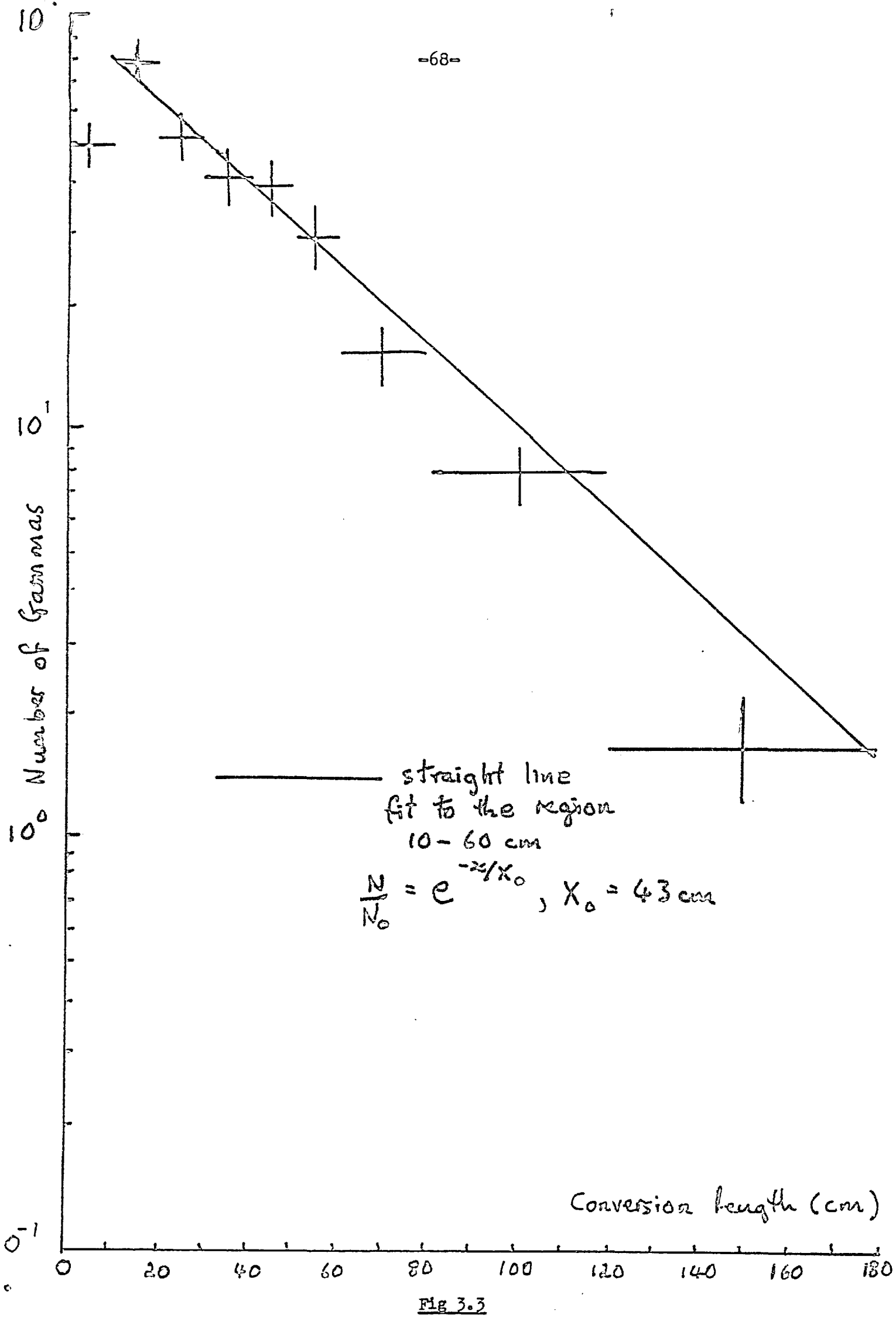
10
10^1
10^0
10^-1
Number of Gammas
straight line
fit to the region
10 - 60 cm
N/N_0 = e^(-x/X_0) , X_0 = 43 cm
Conversion length (cm)
0
20
40
60
80
100
120
140
160
180

Fig 3.3

	WA19	WA47
NUMBER OF NEUTRINO PIX ANTINEUTRINO PIX	103000 181000	157000 261000
DENSITY BEFORE EXPANSION	.72	.68
LIQUID TEMPERATURE	29.2 K	29.2 K
RADIATION LENGTH	42. CM	42. CM
EXPANSION CYCLE LENGTH	9.6 S	9.6 S
MOLAR MIXTURE NE-H2	76/24	73/27
PROTON INTENSITY ON TARGET UNITS OF 10^{12}	2.0-3.0	4.0-5.0

Fig 3.4

a)

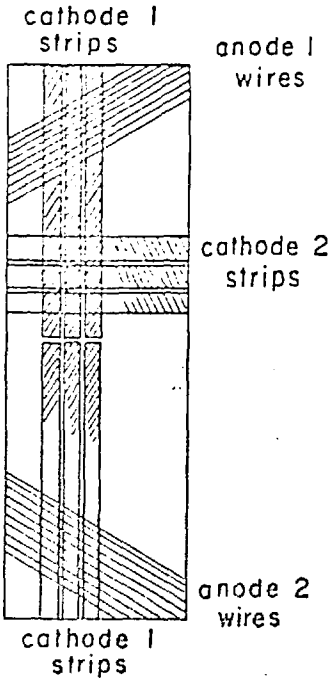

b)

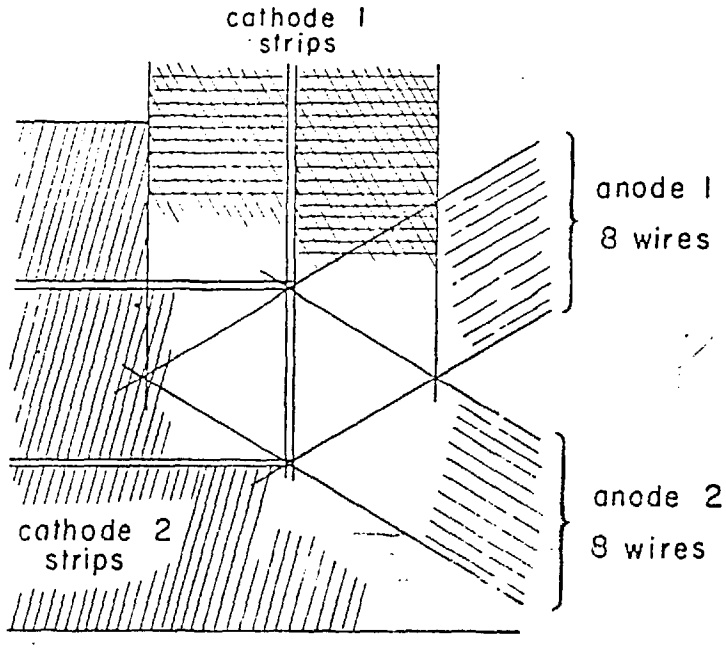

a)

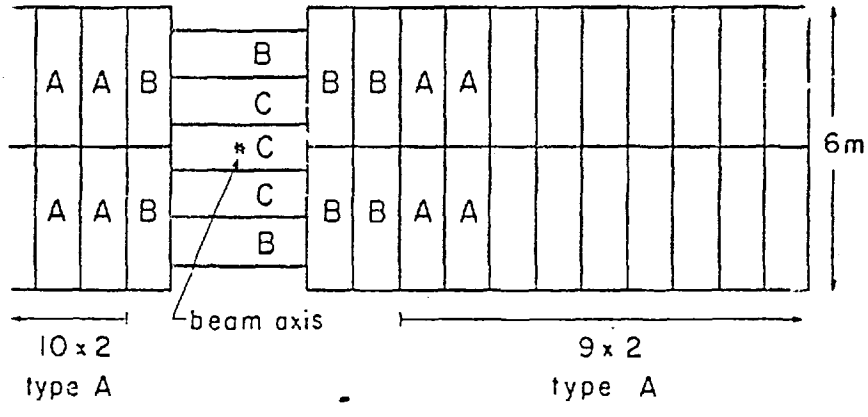

b)

chamber type	anodes one amplifier is connected to	cathode 1 one amplifier is connected to
A	8 wires	2 strips
B	4 -"-	1 -"-
C	2 -"-	1 -"-

Fig 3.5

TRACK LABELLING AND COMMENT SCHEME Fig 3.6

Label & Comment	Description of Track	Entry on Measurement Inf. Sheet
CA (L)	Leaving	No. of C Labels
CA (I)	Interacting. Scatters, kinks and tracks disappearing in flight which are to be measured as corresponding points.	"
CA (P)	A short, straight stopping track. These should be measured as 2-point tracks.	"
CA (S)	Stopping. Any stopping track whose charge can be determined by curvature. Note: It can be positive or negative. If it is negative, make sure it is very heavy at the end, otherwise call it an I.	"
CA (D)	Decay. Decay at rest i.e. $\pi - \mu - e$ or $\mu - e$.	"
CA (C)	Negative capture. A heavy, stopping negative track with a very short recoil proton at the end.	"

KA (I)	Interacting. A short, straight interacting track whose secondaries must be measured.	Enter no. of such tracks and the no. of secondaries to measur from each.
QA	Kink. A track which has a kink close to the primary vertex so that the outgoing track from the kink must also be measured. If the track after the kink need not be measured, then call it CA (I) or AA2 (I) instead.	Enter no. of kinks.
AA2 (E)	Electron. Unambiguously identified primary electron (See Sect. 6)	Only enter in no. of charged prongs.
AA2 (PE)	Possible electron. Primary electron candidate which might also be a hadron (See Sect. 6)	"
MA (G)	Gamma. Gammas associated to primary vertices. Note: one-armed gammas must be labelled first before all other gammas and V^0's. (See Sect. 4e)	Total no. of gammas including asymetric ones, in the gammas and V^0 total. Asymetr gammas also appear in a separate column.

Fig 3.6 (continued)

MA (V)	V^o	Included in gamma and V^o total.
MA	Ambiguous V^o/gamma. These should only appear at the end of the chamber when the tracks both leave.	"

Fig 3.6 (continued)

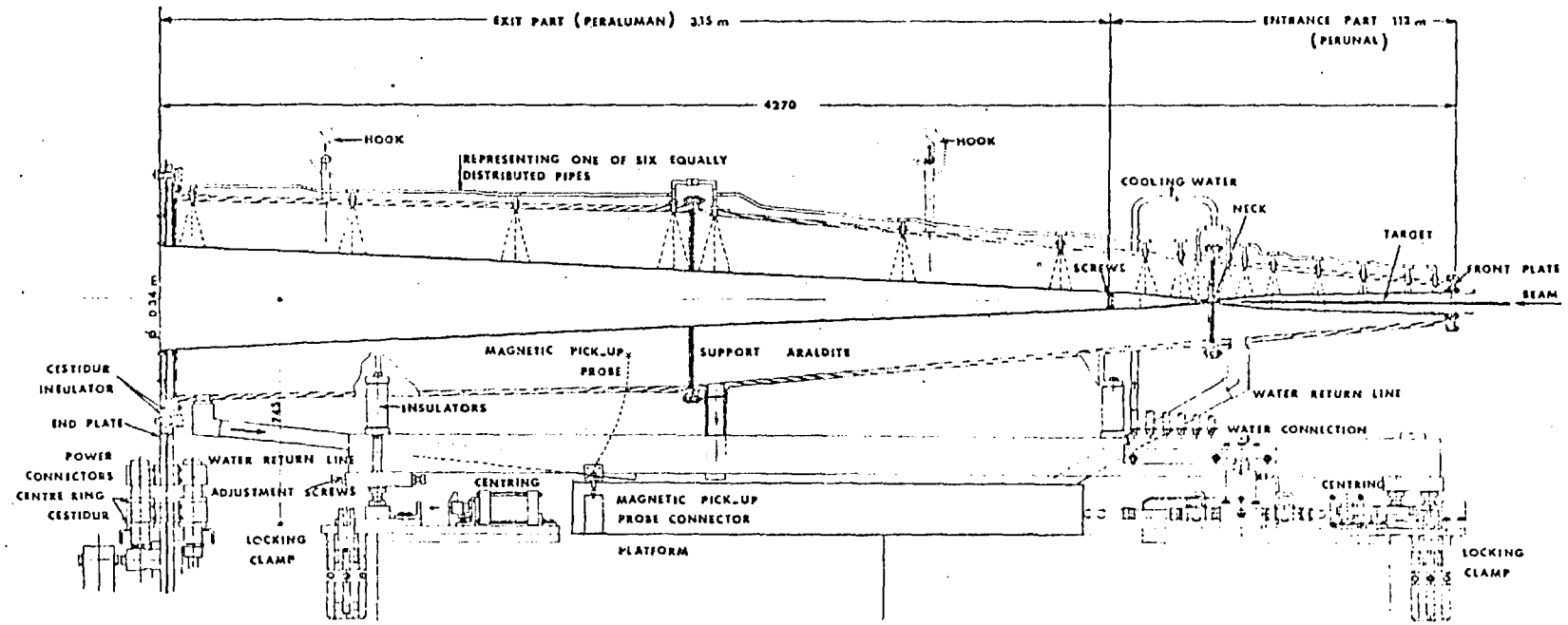
EXIT PART (PERALUMAN) 3.15 m
ENTRANCE PART 1.12 m
(PERUNAL)
4270
HOOK
HOOK
REPRESENTING ONE OF SIX EQUALLY
DISTRIBUTED PIPES
COOLING WATER
NECK
TARGET
FRONT PLATE
BEAM
SCREWS
MAGNETIC PICK-UP
PROBE
SUPPORT ARALDITE
CESTIDUR
INSULATOR
END PLATE
INSULATORS
WATER RETURN LINE
WATER CONNECTION
POWER
CONNECTORS
CENTRE RING
CESTIDUR
WATER RETURN LINE
ADJUSTMENT SCREWS
CENTRING
MAGNETIC PICK-UP
PROBE CONNECTOR
CENTRING
LOCKING
CLAMP
PLATFORM
LOCKING
CLAMP

Fig 4.1

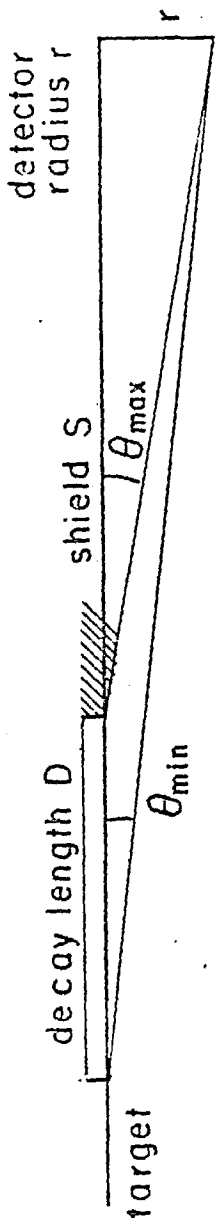
detector
radius r
r
shield S
θ_{max}
decay length D
θ_{min}
target

Fig 4.2

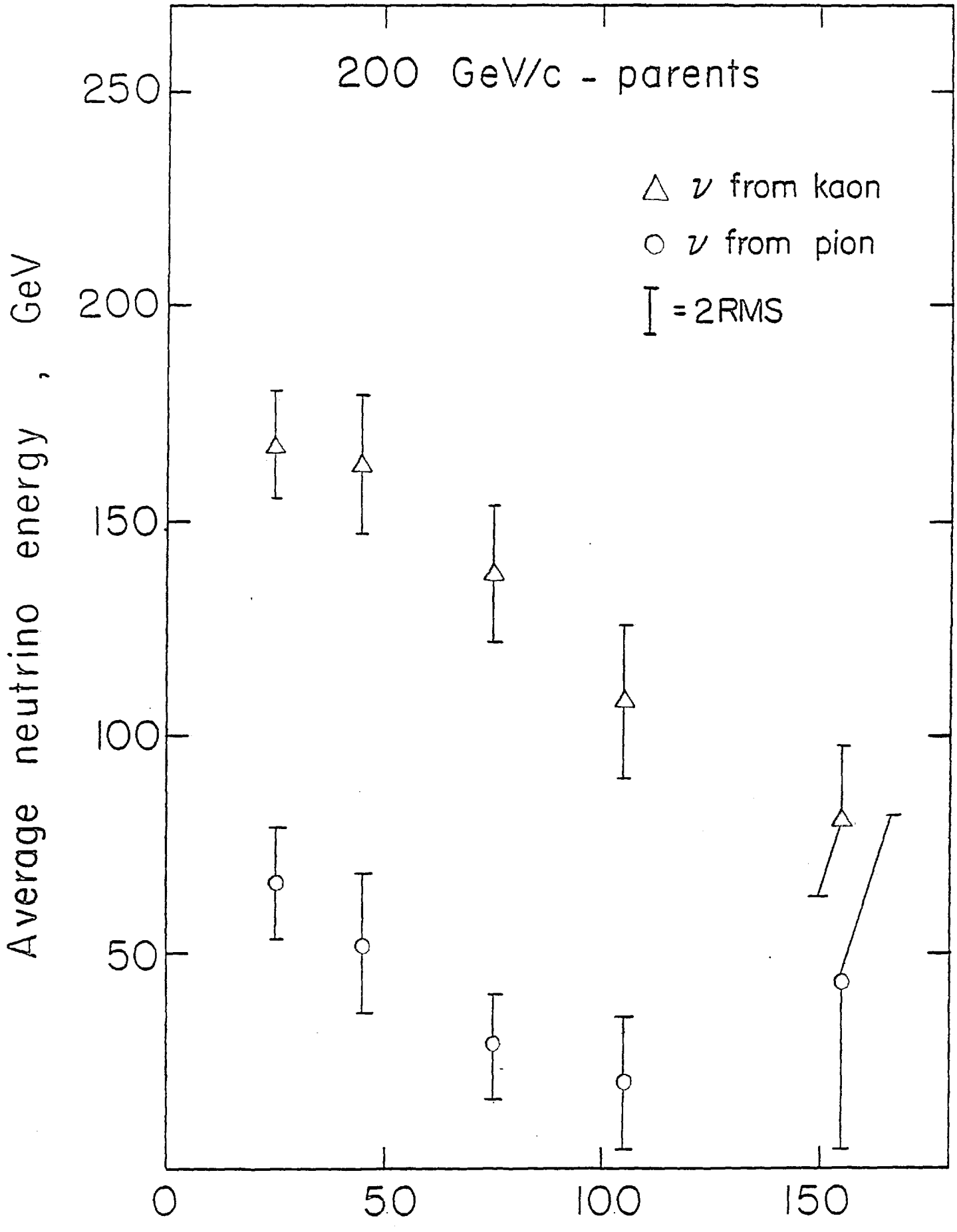
200 GeV/c - parents
△ ν from kaon
○ ν from pion
I = 2RMS
Average neutrino energy , GeV
250
200
150
100
50
0
50
100
150
R = distance of neutrino from beam axis , cm

Fig 4.3

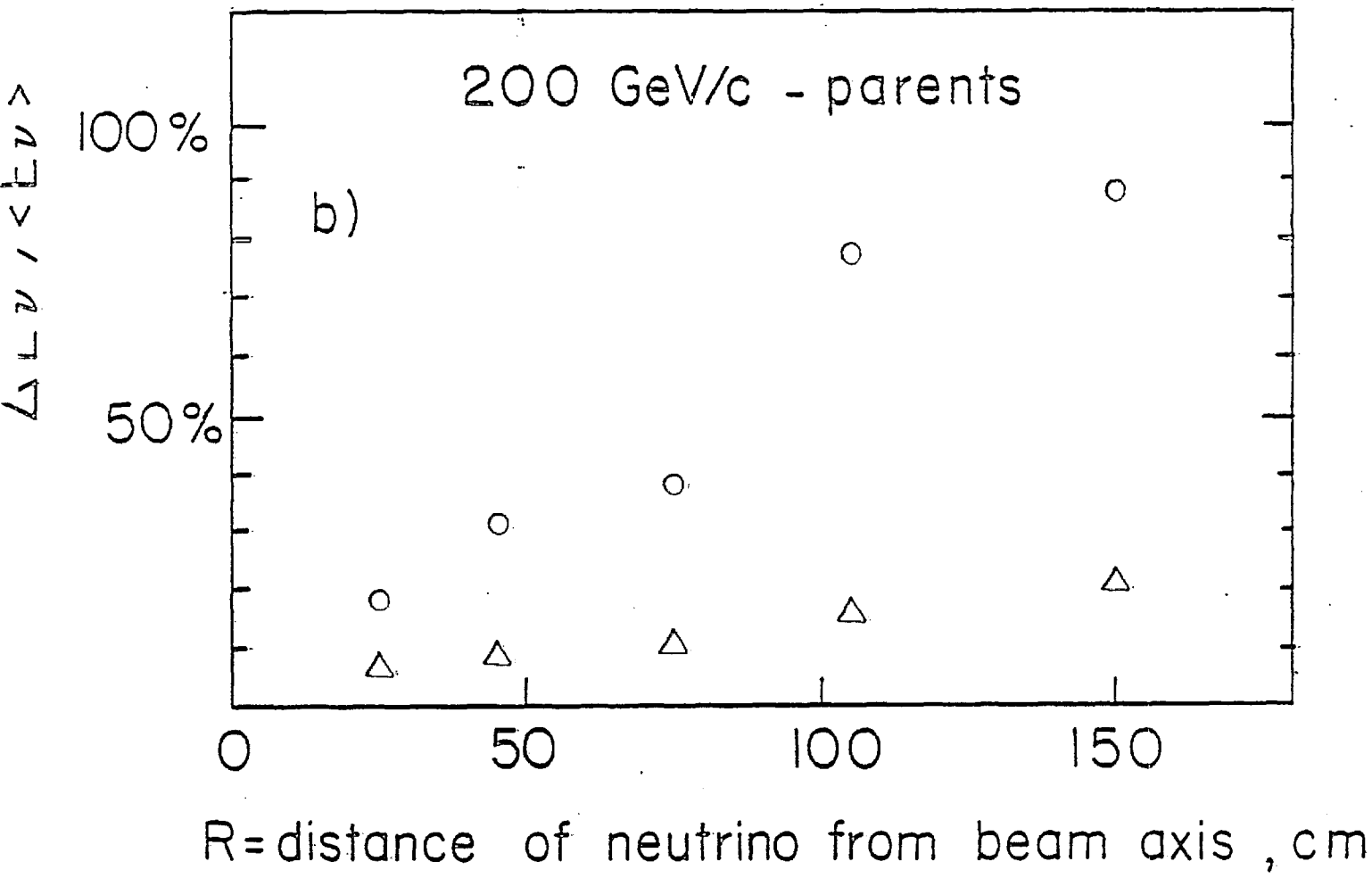

Fig 4.3 (continued)

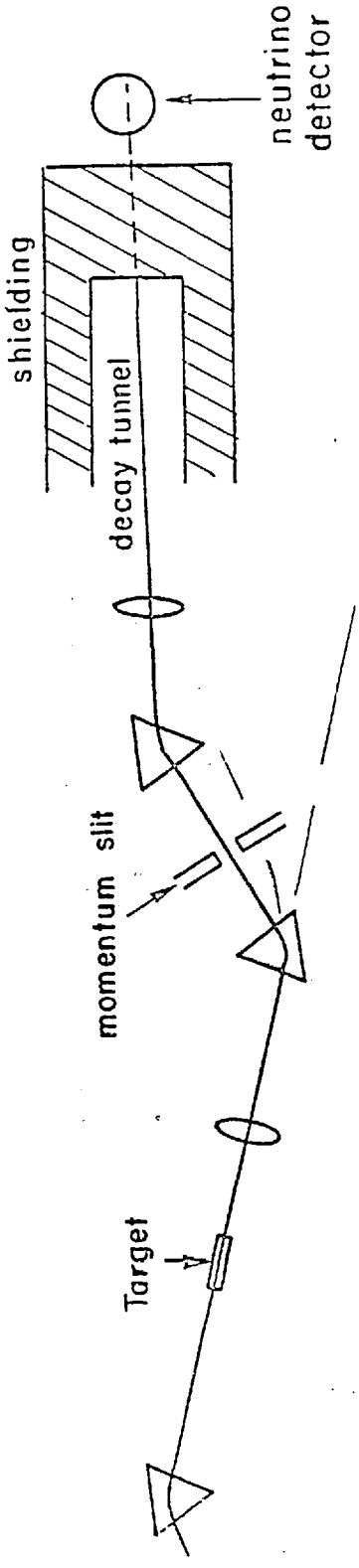
neutrino
detector
shielding
decay tunnel
momentum slit
Target

Fig 4.4

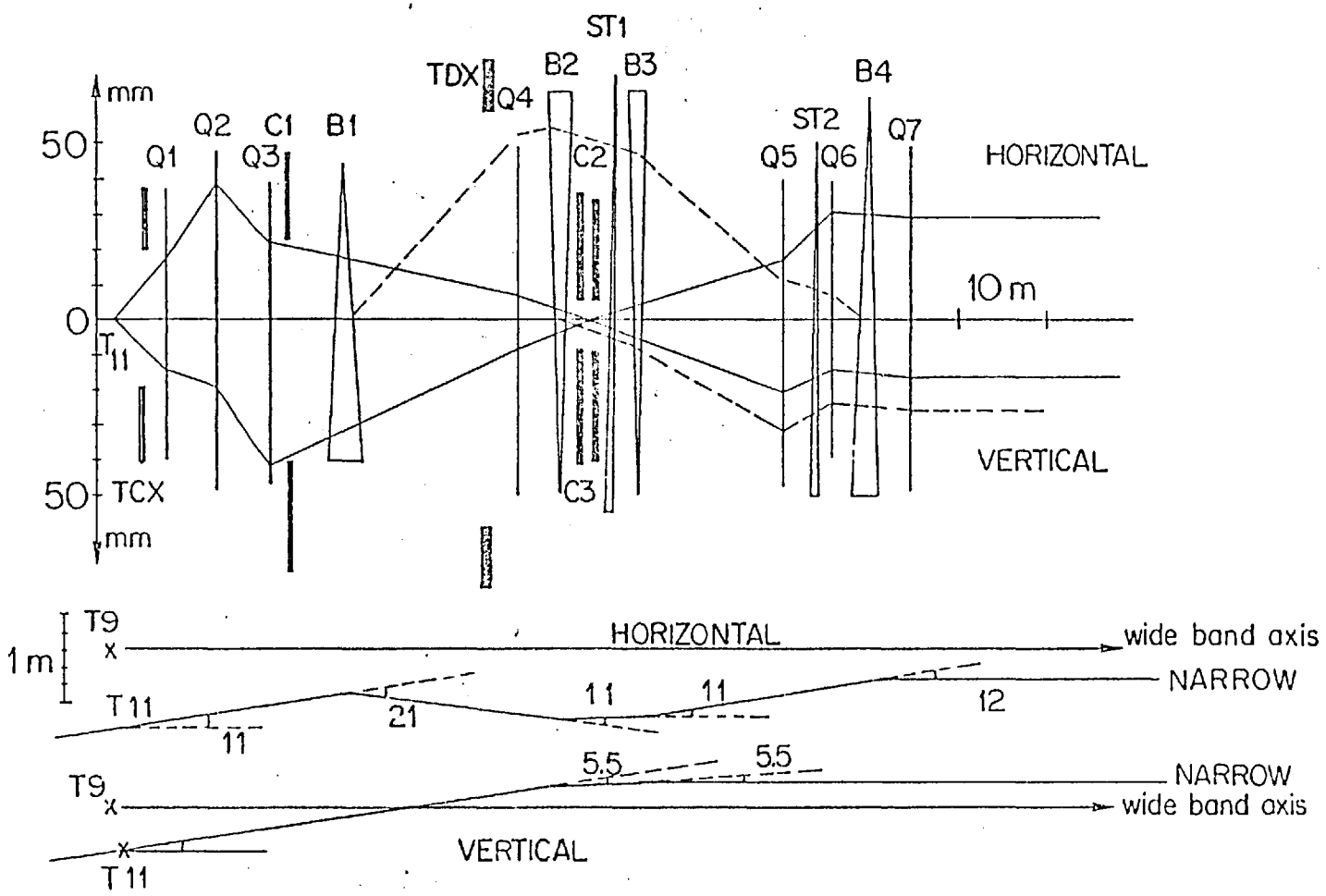
mm
50
0
50
mm
Q1
Q2
C1
B1
Q3
TDX
Q4
B2
ST1
B3
C2
C3
B4
ST2
Q5
Q6
Q7
HORIZONTAL
10 m
VERTICAL
T11
TCX
1 m
T9
x
HORIZONTAL
wide band axis
NARROW
T11
11
21
11
11
12
5.5
5.5
NARROW
T9
x
wide band axis
VERTICAL
T11

Fig 4.5

35
34
33
32
23
22
21
31
41
51
61
71
15
14
13
12
11
01
02
03
04
05
06
40
46
45
44
43
42
72
73
74
75
52
53
54
55
62
63
30
45
60
75 cm

Fig 4.6

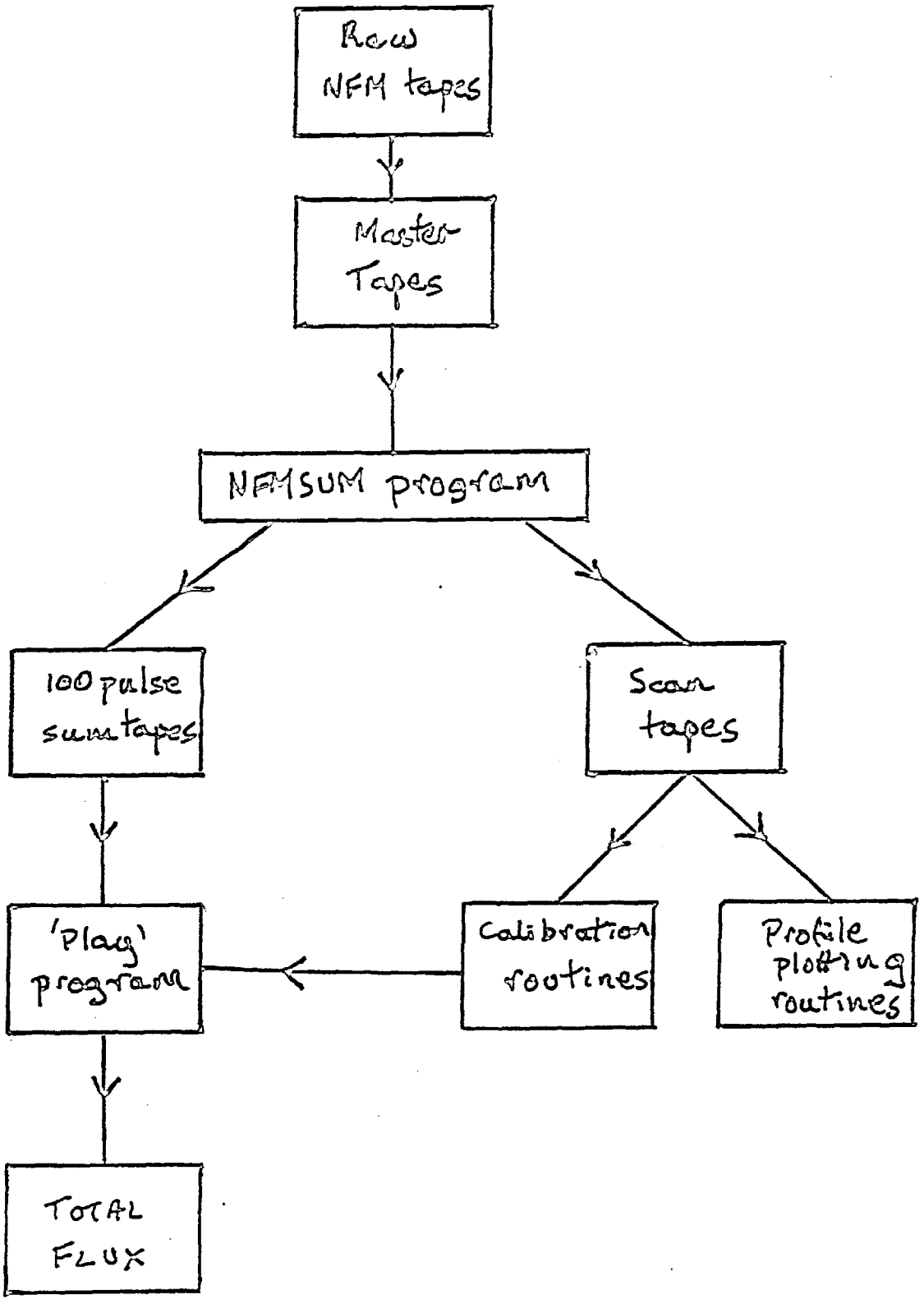
Raw NFM tapes
Master Tapes
NFMSUM program
100 pulse sum tapes
Scan tapes
'Play' program
Calibration routines
Profile plotting routines
TOTAL FLUX

Fig 5.1

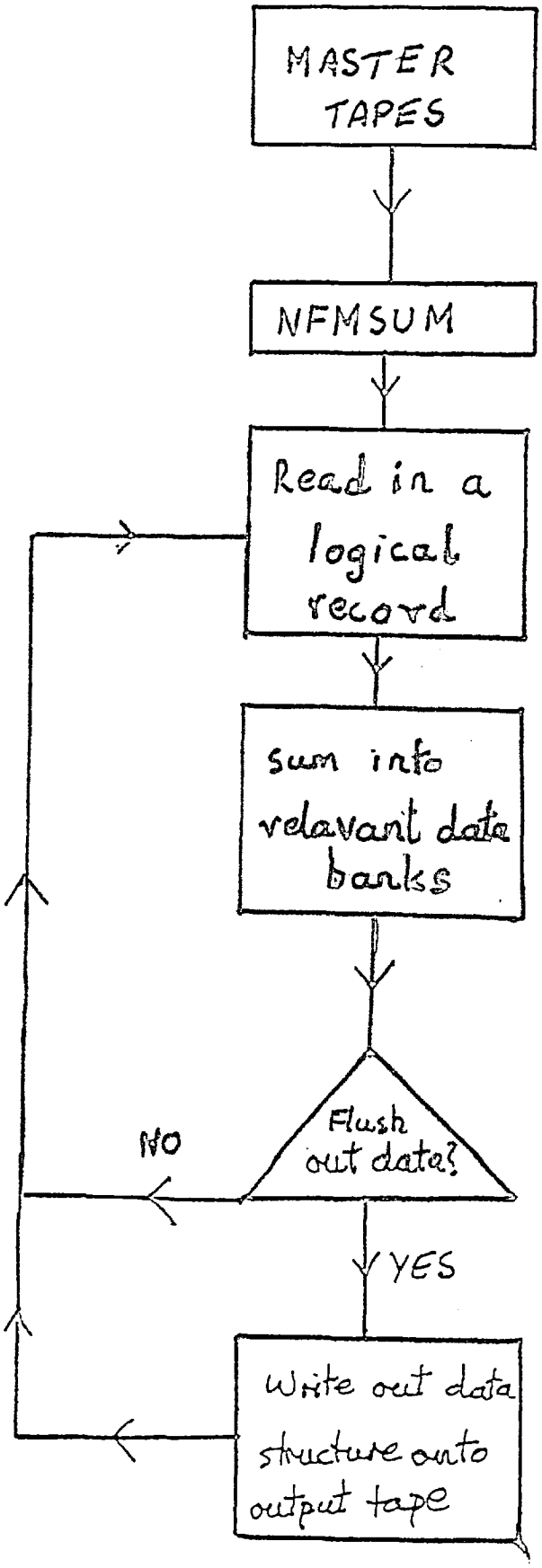
MASTER TAPES
NFMSUM
Read in a logical record
sum into relavant data banks
Flush out data?
NO
YES
Write out data structure onto output tape

Fig 5.2

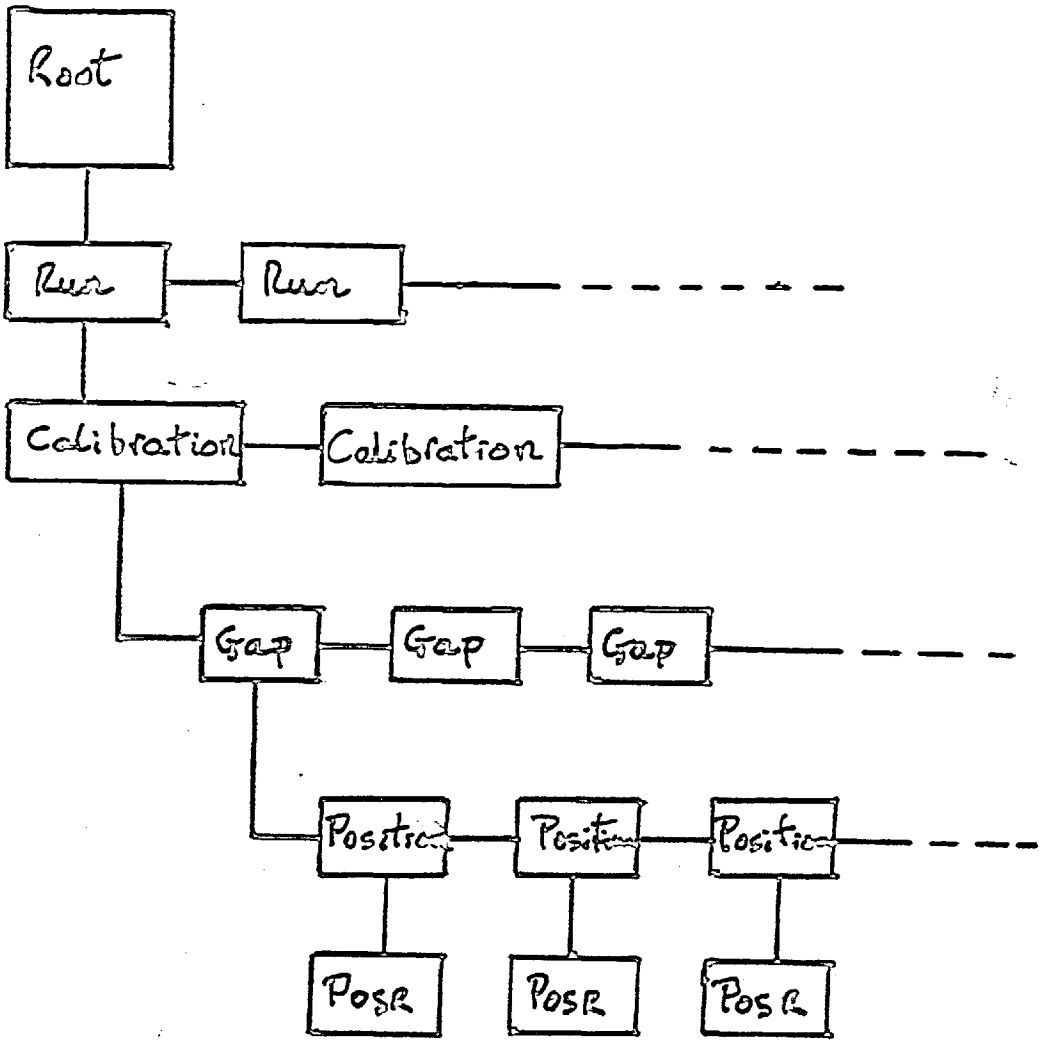
Root
Run
Run
Calibration
Calibration
Gap
Gap
Gap
Positio
Positio
Positio
PosR
PosR
PosR

Fig 5.3

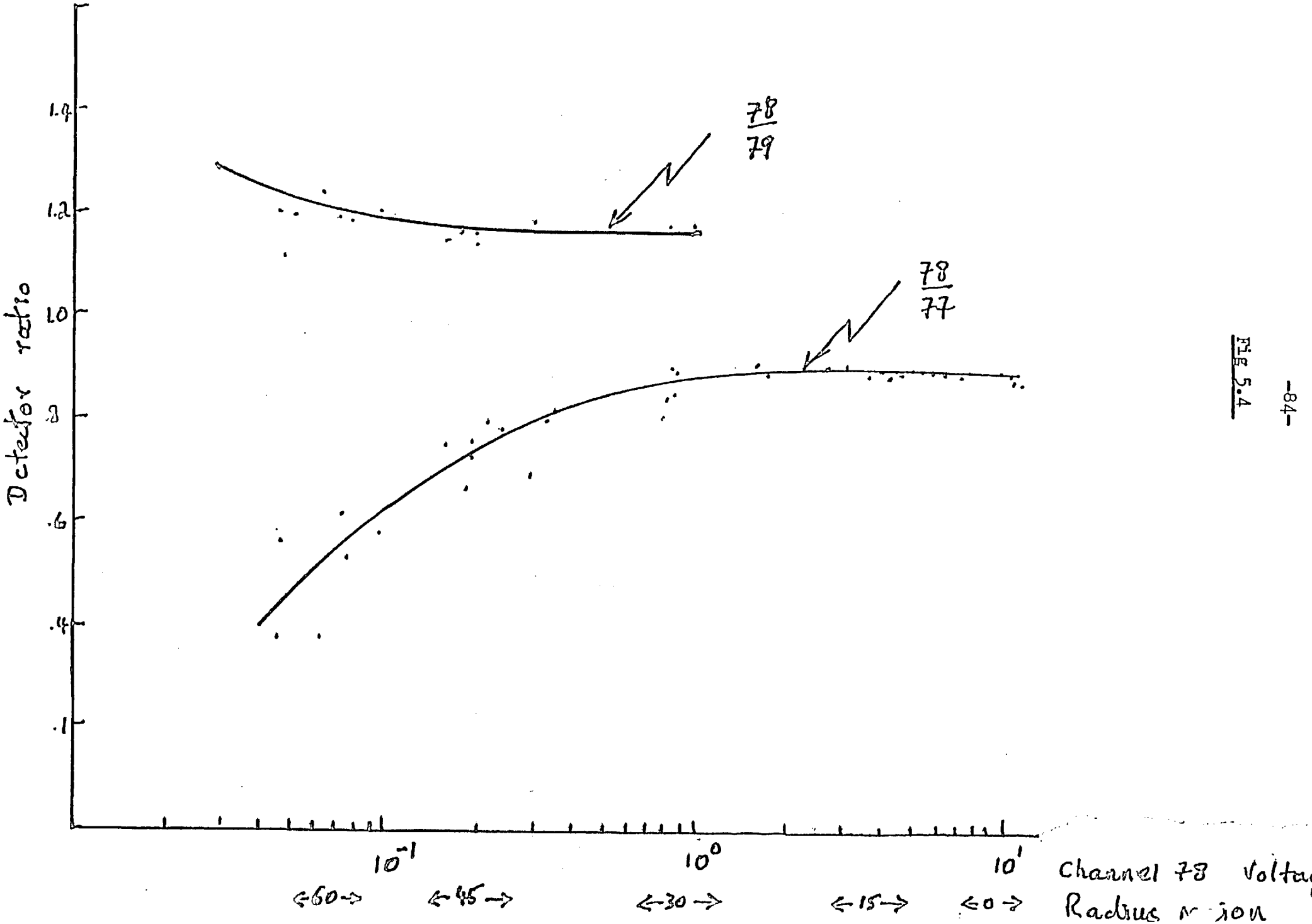
Detector ratio
1.4
1.2
1.0
.8
.6
.4
.1
78/79
78/77
10^{-1}
10^{0}
10^{1}
<60>
<45>
<30>
<15>
<0>
Channel 78 Voltage
Radius region

Fig 5.4

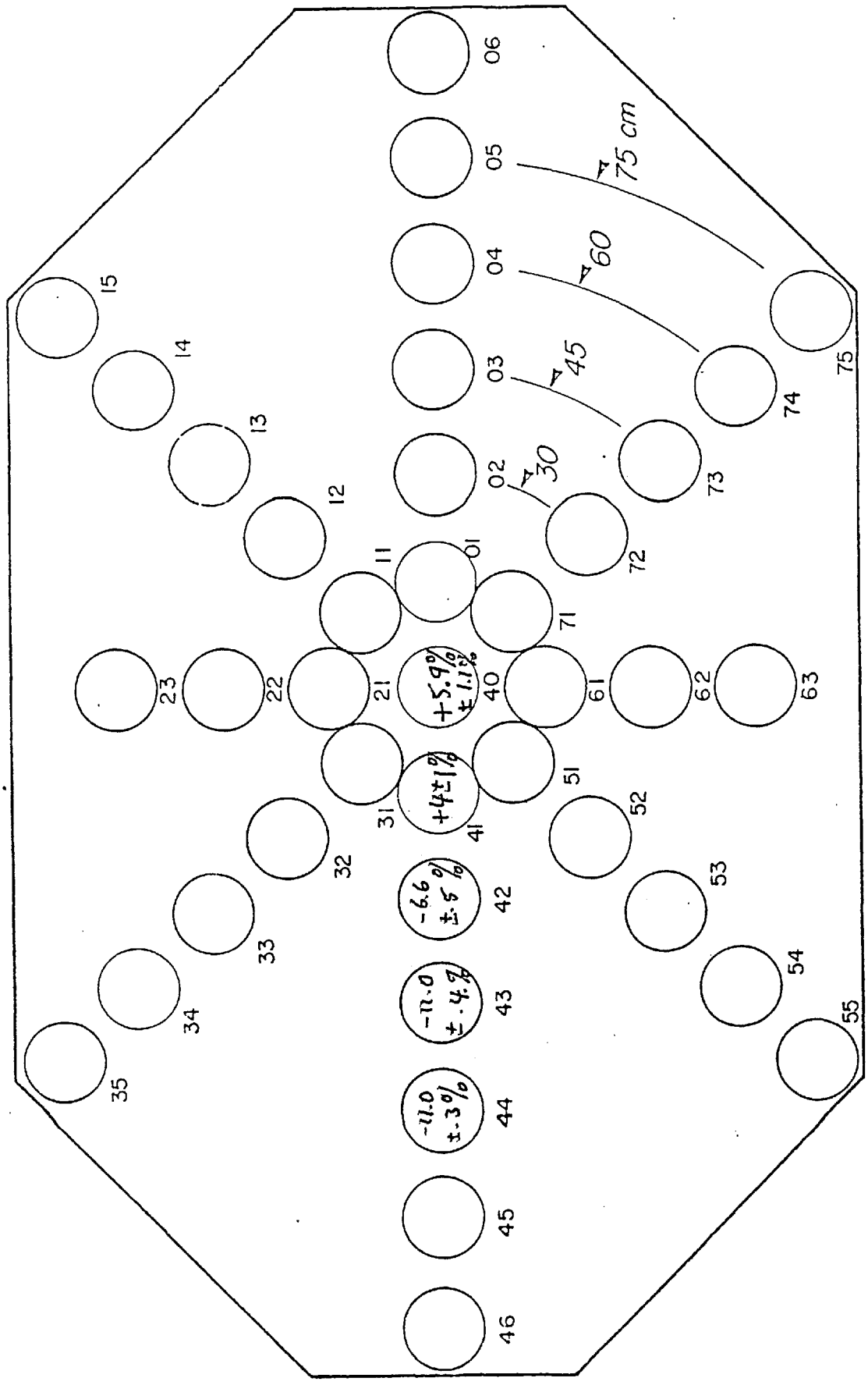
06
05
04
03
02
01
15
14
13
12
11
75 cm
60
45
30
75
74
73
72
71
23
22
21
40
61
62
63
+5.9%
±1.1%
+4±1%
31
41
51
52
32
42
53
33
-6.6%
±.5%
43
54
34
-11.0
±.4%
55
35
-11.0
±.3%
44
45
46

Fig 5.5

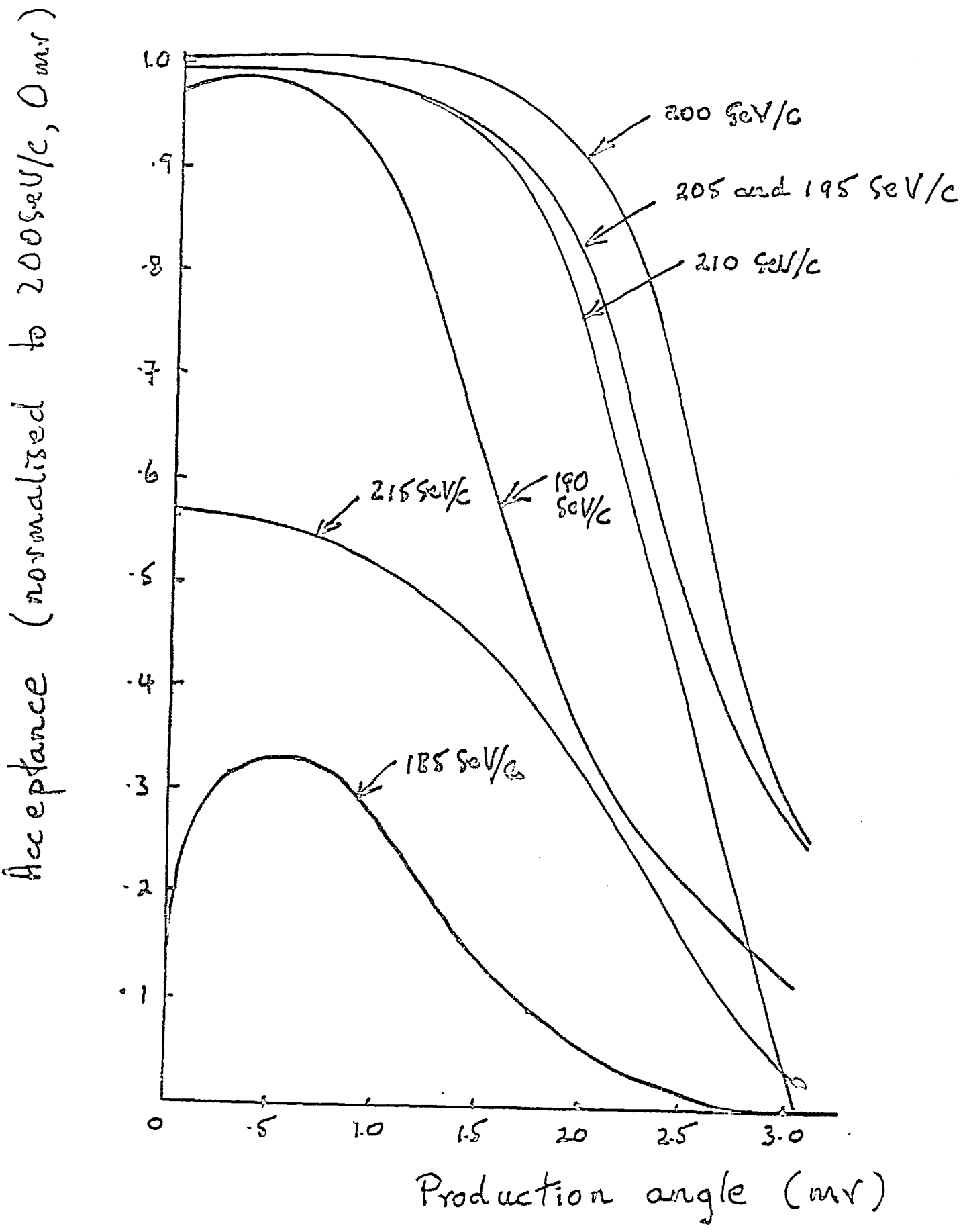
Acceptance (normalised to 200 GeV/c, 0 mr)
1.0
.9
.8
.7
.6
.5
.4
.3
.2
.1
0
.5
1.0
1.5
2.0
2.5
3.0
Production angle (mr)
200 GeV/c
205 and 195 GeV/c
210 GeV/c
215 GeV/c
190 GeV/c
185 GeV/c

Fig 6.1

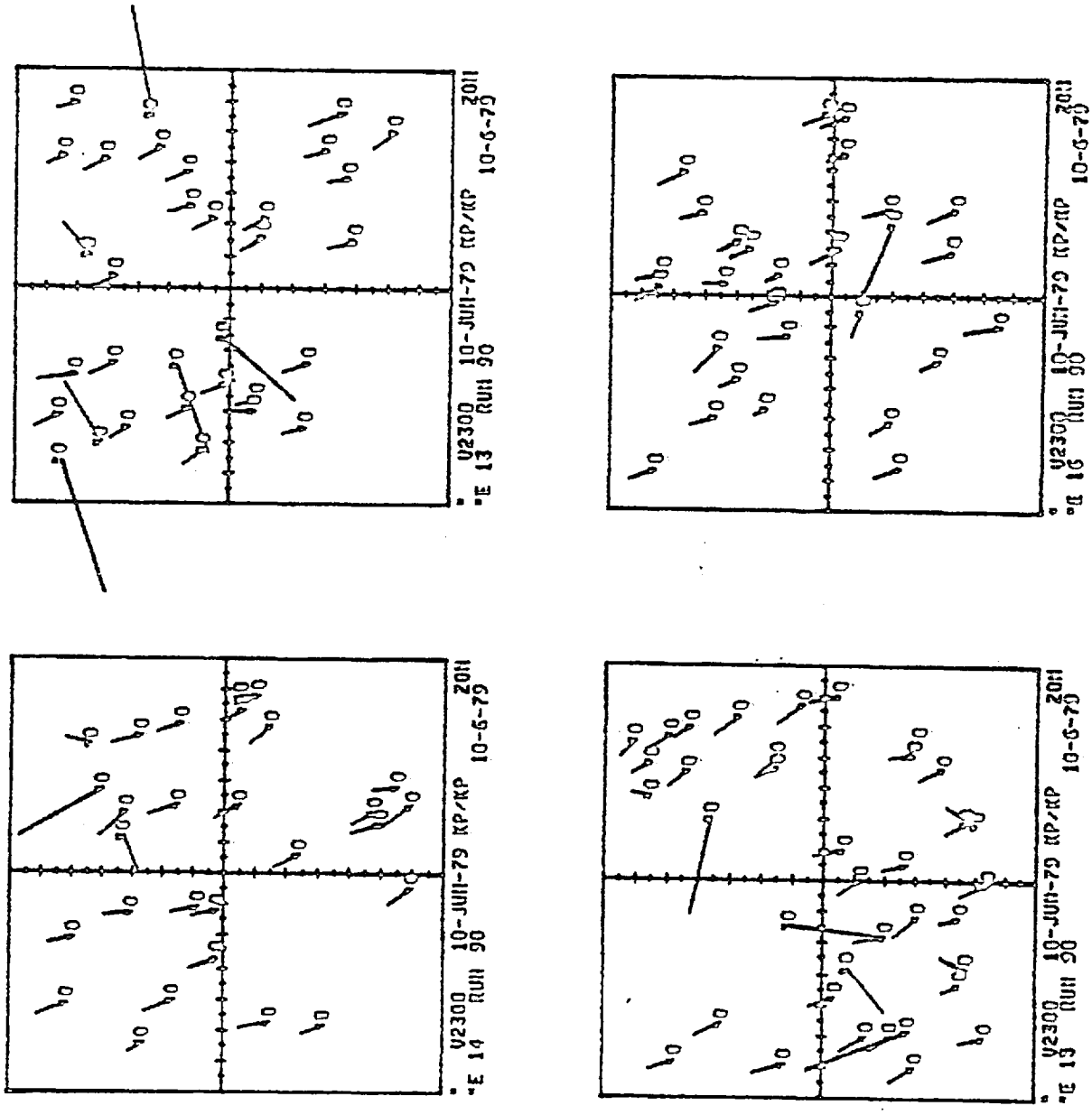
V2300 RUN 90 10-JUIN-79 KP/KP 10-6-79 2011
E 13
V2300 RUN 90 10-JUIN-79 KP/KP 10-6-79 2011
E 16
V2300 RUN 90 10-JUIN-79 KP/KP 10-6-79 2011
E 14
V2300 RUN 90 10-JUIN-79 KP/KP 10-6-79 2011
E 13

Fig. 6.2

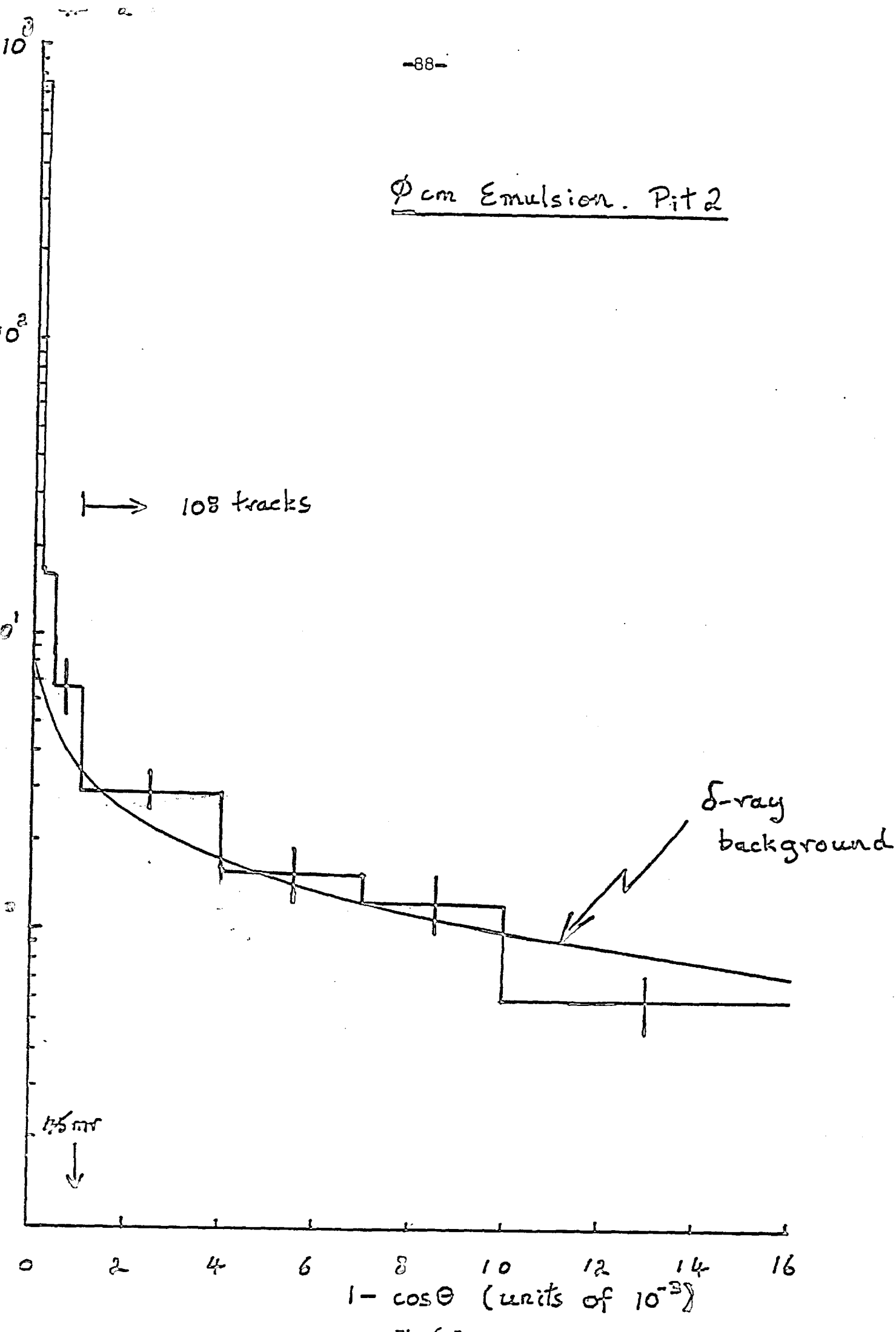
ϕ cm Emulsion. Pit 2
108 tracks
δ-ray background
1.5 mr
0
2
4
6
8
10
12
14
16
1 − cosΘ (units of 10^{-3})

Fig 6.3

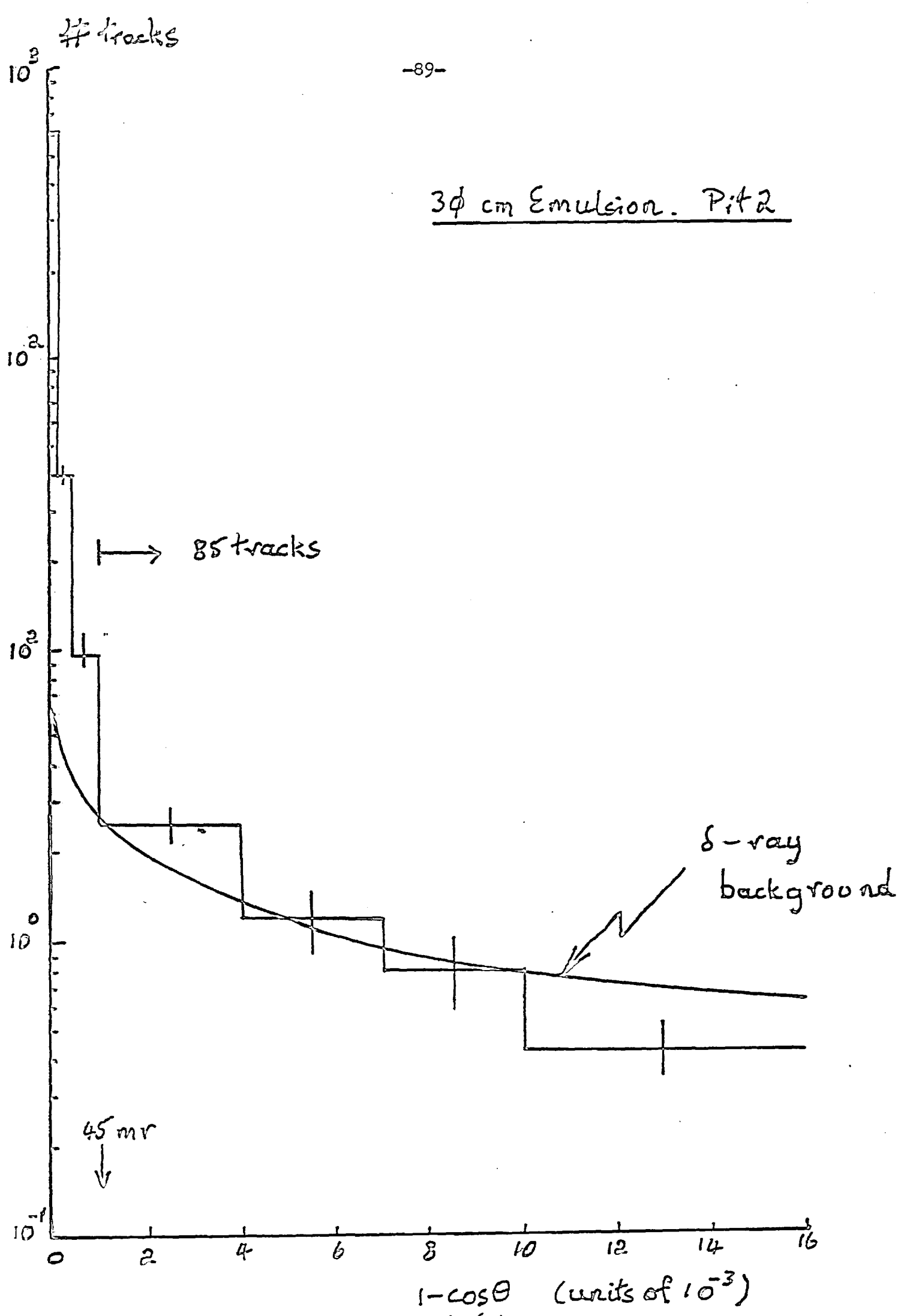
tracks
10^3
10^2
10^2
10^0
10^{-1}
3ϕ cm Emulsion. Pit 2
85 tracks
δ-ray background
45 mr
0
2
4
6
8
10
12
14
16
1-cosθ (units of 10^{-3})

Fig 6.4

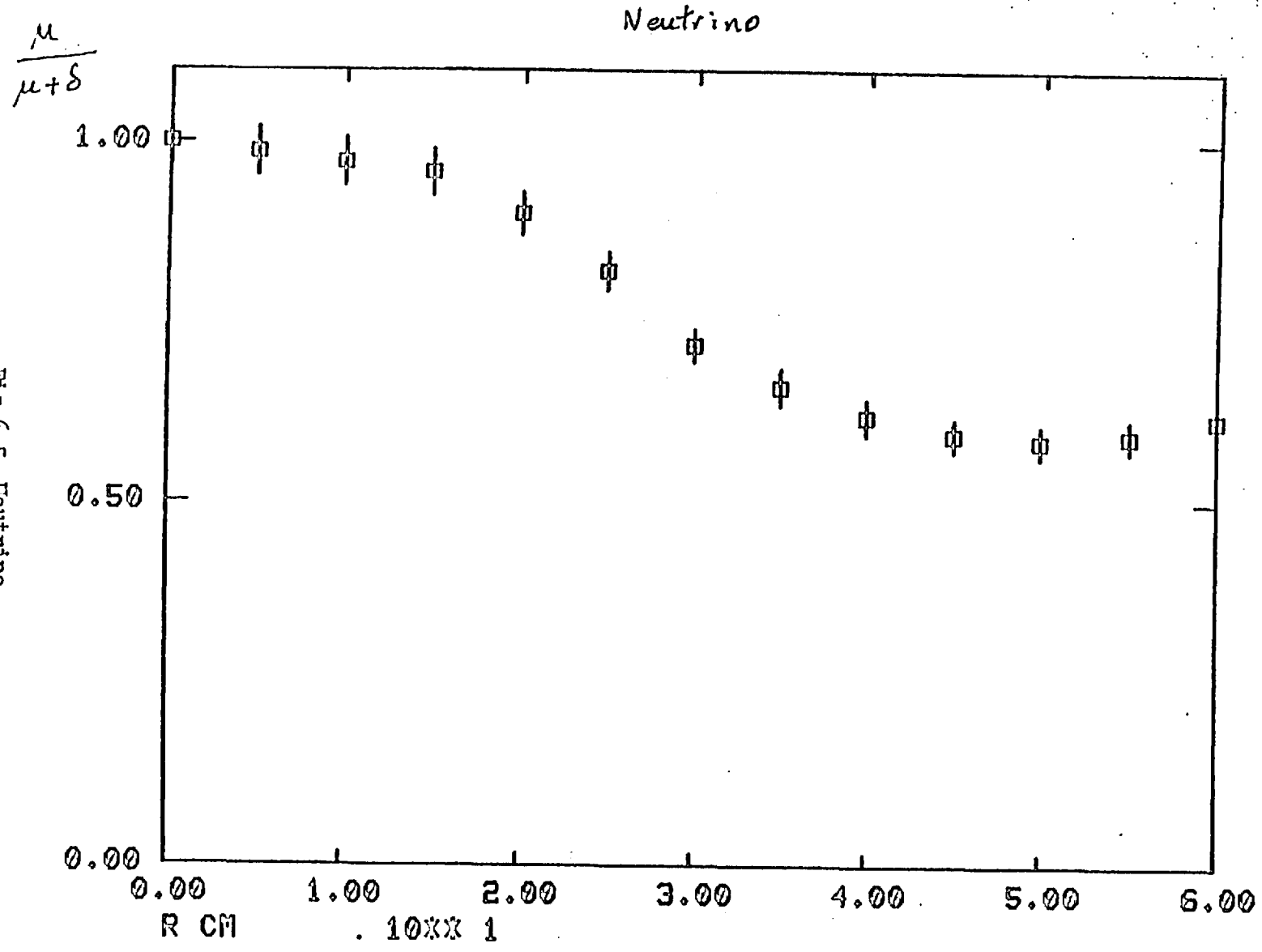

Fig 6.5 Neutrino

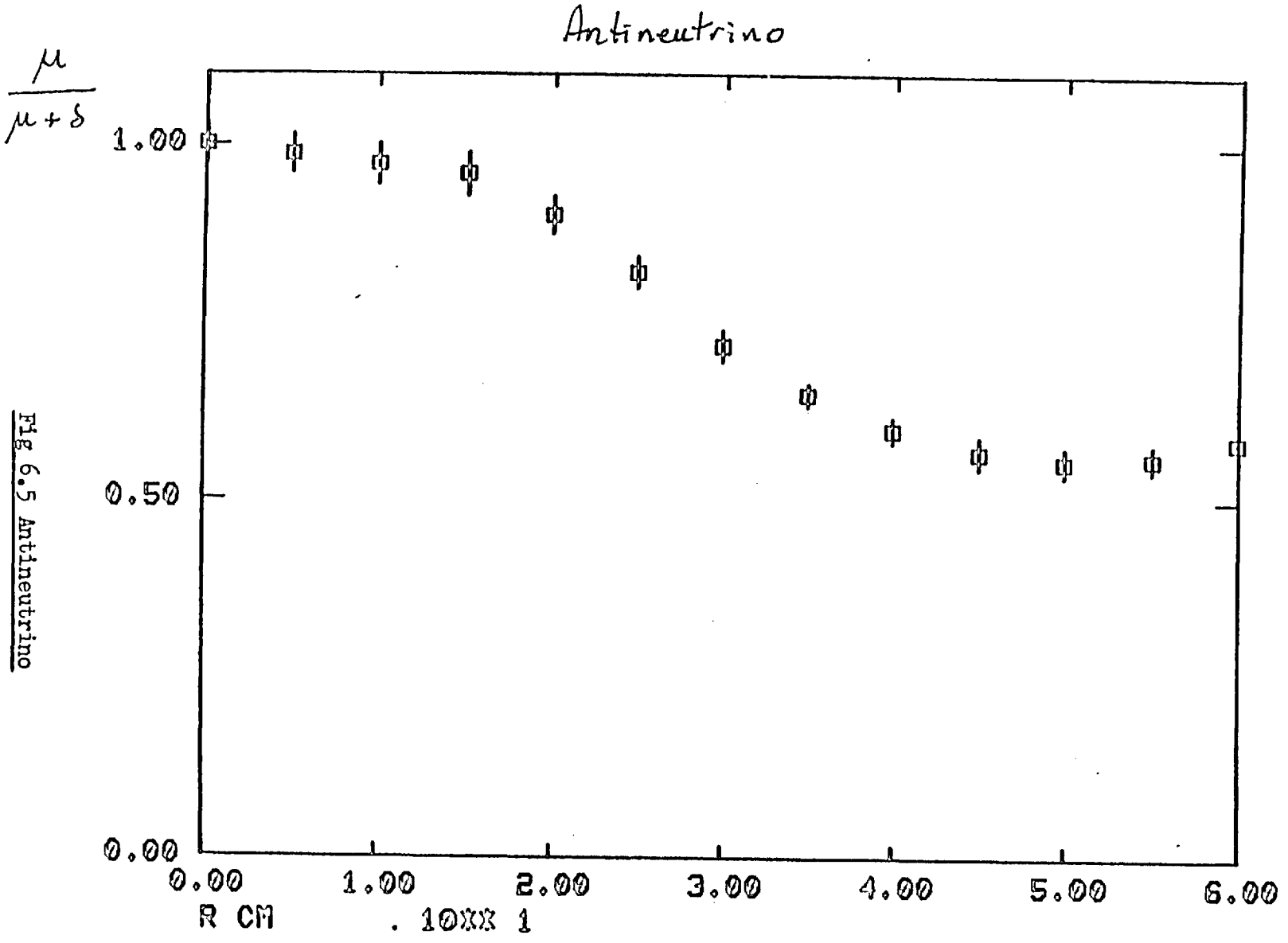

Fig 6.5 Antineutrino

Table of Trapped Muons in Gap2

From Decays before 116m after the Target

1	60.	55.	50.	45.	40.	35.	30.	25.	20.	15.	10.	5.	0.	-5.	-10.	-15.	-20.	-25.	-30.	-35.	-40.	-45.	-50.	-55.	-60.
2	.271	.220	.239	.231	.142	.135	.100	.080	.085	.062	.062	.063	.061	.063	.060	.061	.055	.058	.037	.054	.030	.033	.030	.030	.033
3	.271	.220	.239	.231	.149	.145	.020	.072	.080	.057	.059	.060	.059	.062	.062	.063	.061	.069	.050	.087	.000	.033	.000	.000	.000
4	0	0	0	0	0	5	18	57	154	346	617	919	1033	898	566	284	120	47	18	6	1	0	0	0	0
5	0	0	0	0	0	0	1	3	11	18	34	54	60	55	35	18	7	3	1	0	0	0	0	0	0
6	5	6	7	9	11	14	10	23	36	44	61	69	72	73	57	42	32	24	18	12	11	7	7	5	5
7	1	1	1	2	1	1	2	2	4	5	7	8	7	5	1	1	0	0	0	0	0	0	0	0	0

1) Radius in metres
2) Trapped/Total (K/π = .144)
3) Trapped/Total (K/π = .047)

4) Trapped μ_π
5) Total μ_π
6) Trapped μ_K
7) Total μ_K

} rounded to integers

Fig 6.6

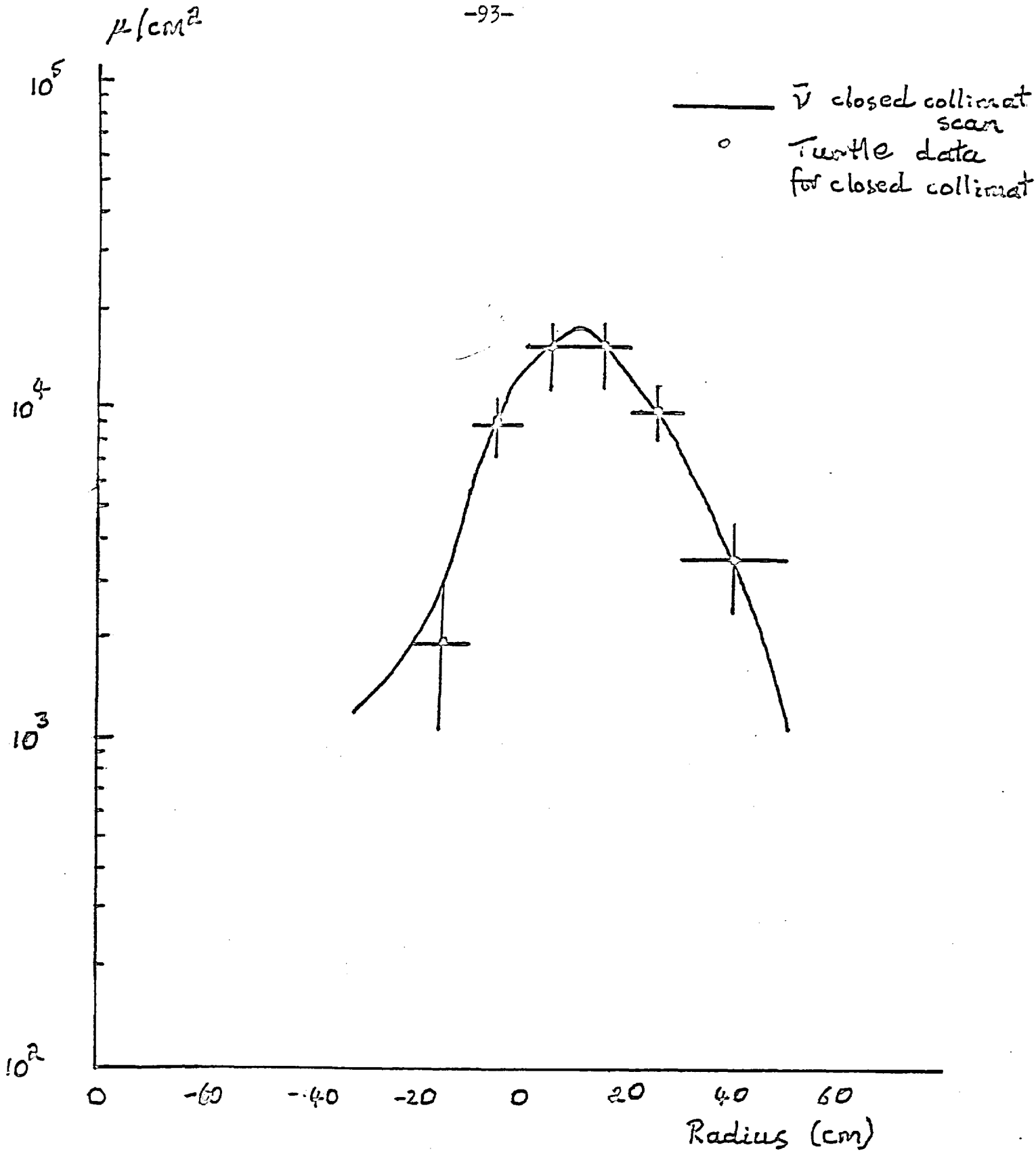
μ/cm²
10⁵
10⁴
10³
10²
$\bar{\nu}$ closed collimat scan
Turtle data for closed collimat
0
-60
-40
-20
0
20
40
60
Radius (cm)

Fig 6.7

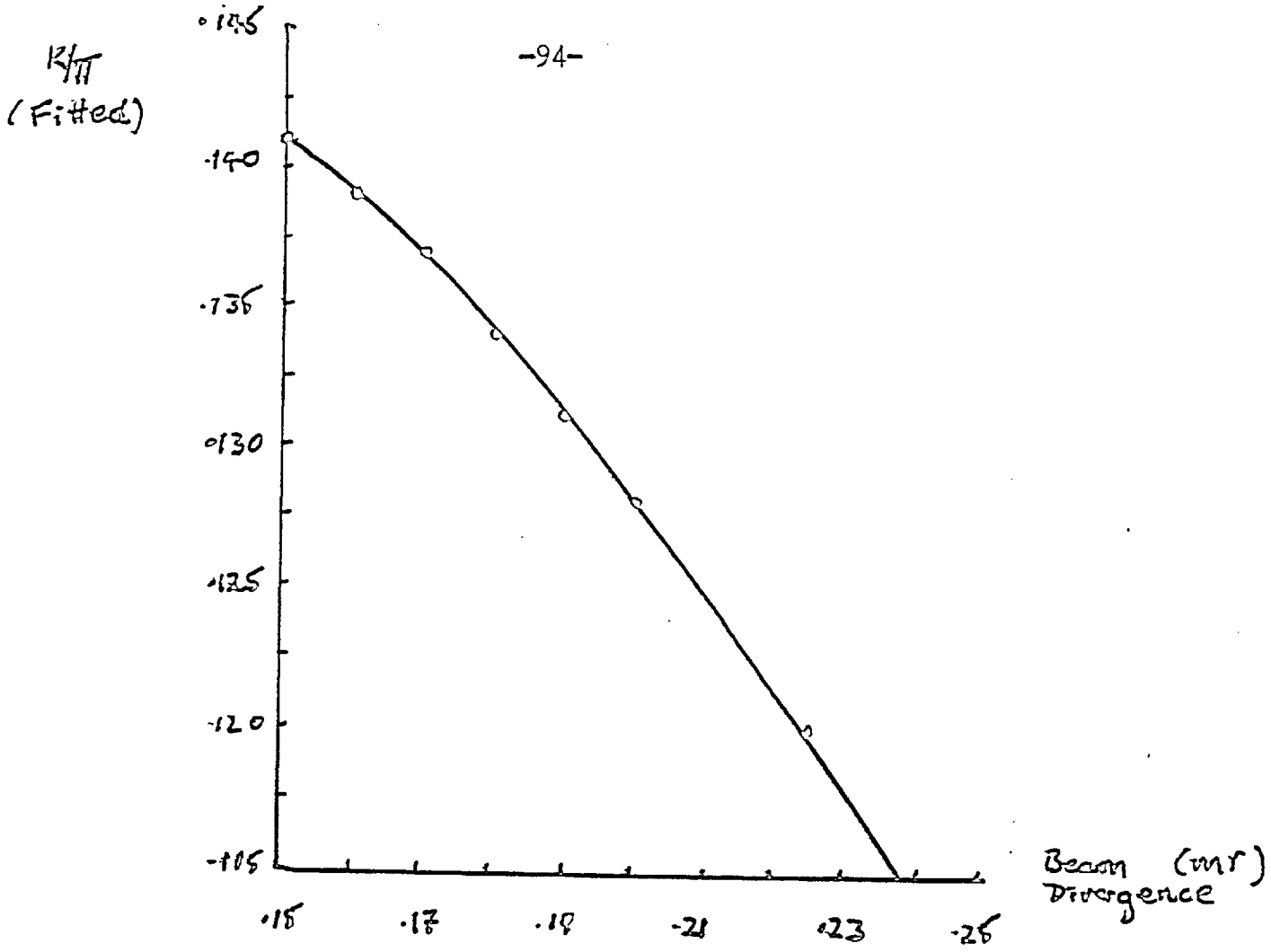
K/π (Fitted)
·145
·140
·135
·130
·125
·120
·115
·15
·17
·19
·21
·23
·25
Beam (mr) Divergence

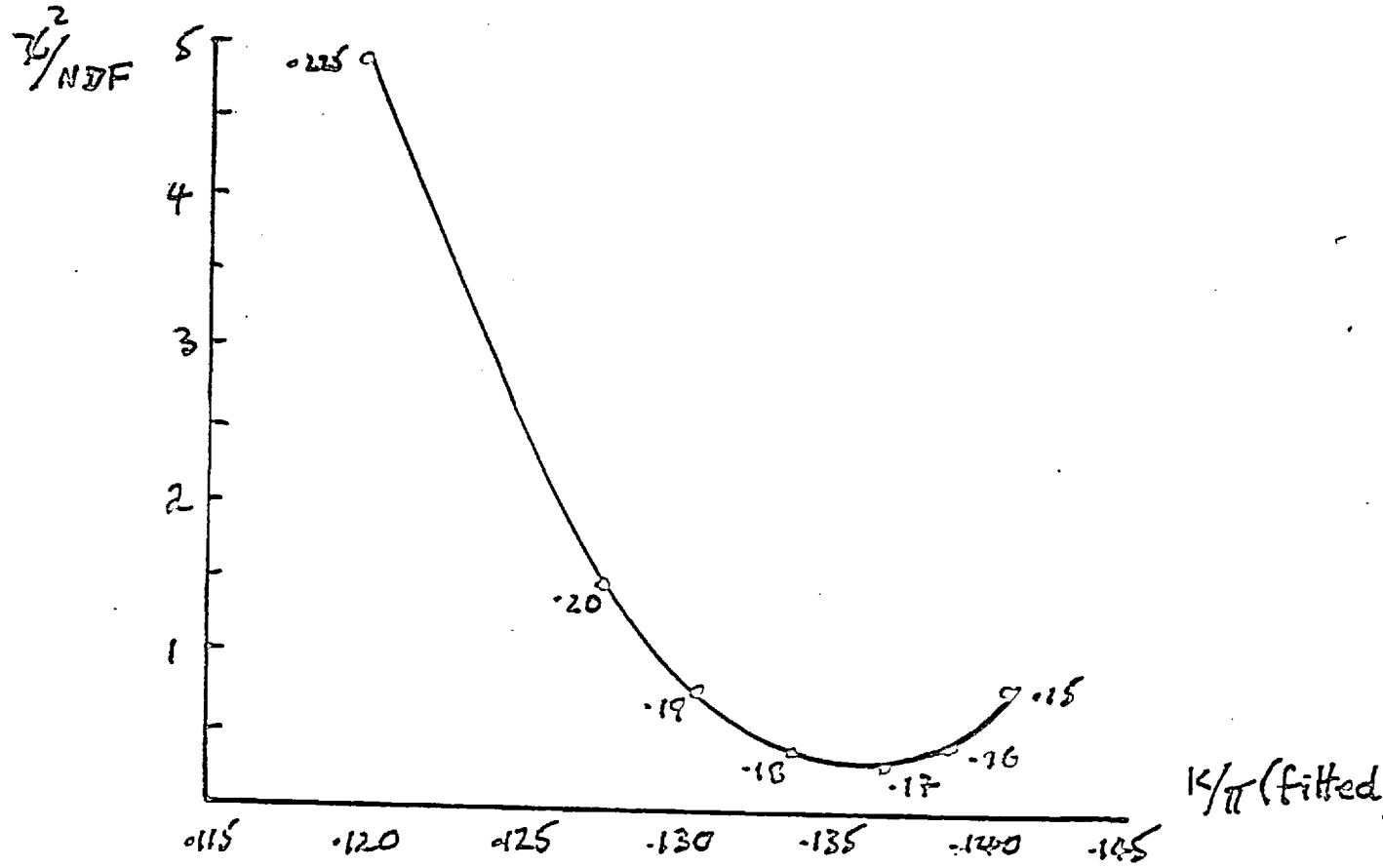
χ²/NDF
5
4
3
2
1
·225
·20
·19
·18
·17
·16
·15
·115
·120
·125
·130
·135
·140
·145
K/π (fitted)

Fig 6.8 (a)

Beam Divergence	Positives		Negatives	
	K/π	χ^2	K/π	χ^2
.150	.141 ± 8.5%	.811	.072 ± 7.6%	1.681
.160	.139 ± 8.9%	.446	.071 ± 7.7%	.860
.170	.137 ± 8.7%	.296	.070 ± 7.8%	.432
.180	.134 ± 8.9%	.399	.068 ± 8.0%	.462
.190	.131 ± 9.1%	.773	.067 ± 8.2%	1.036
.200	.128 ± 9.3%	1.477	.065 ± 8.4%	2.225
.225	.120 ± 9.5%	4.946	.059 ± 9.3%	8.832
.250	.109 ± 9.6%	XXXXX	.053 ± 9.4%	XXXXX

Fig 6.8 (b)

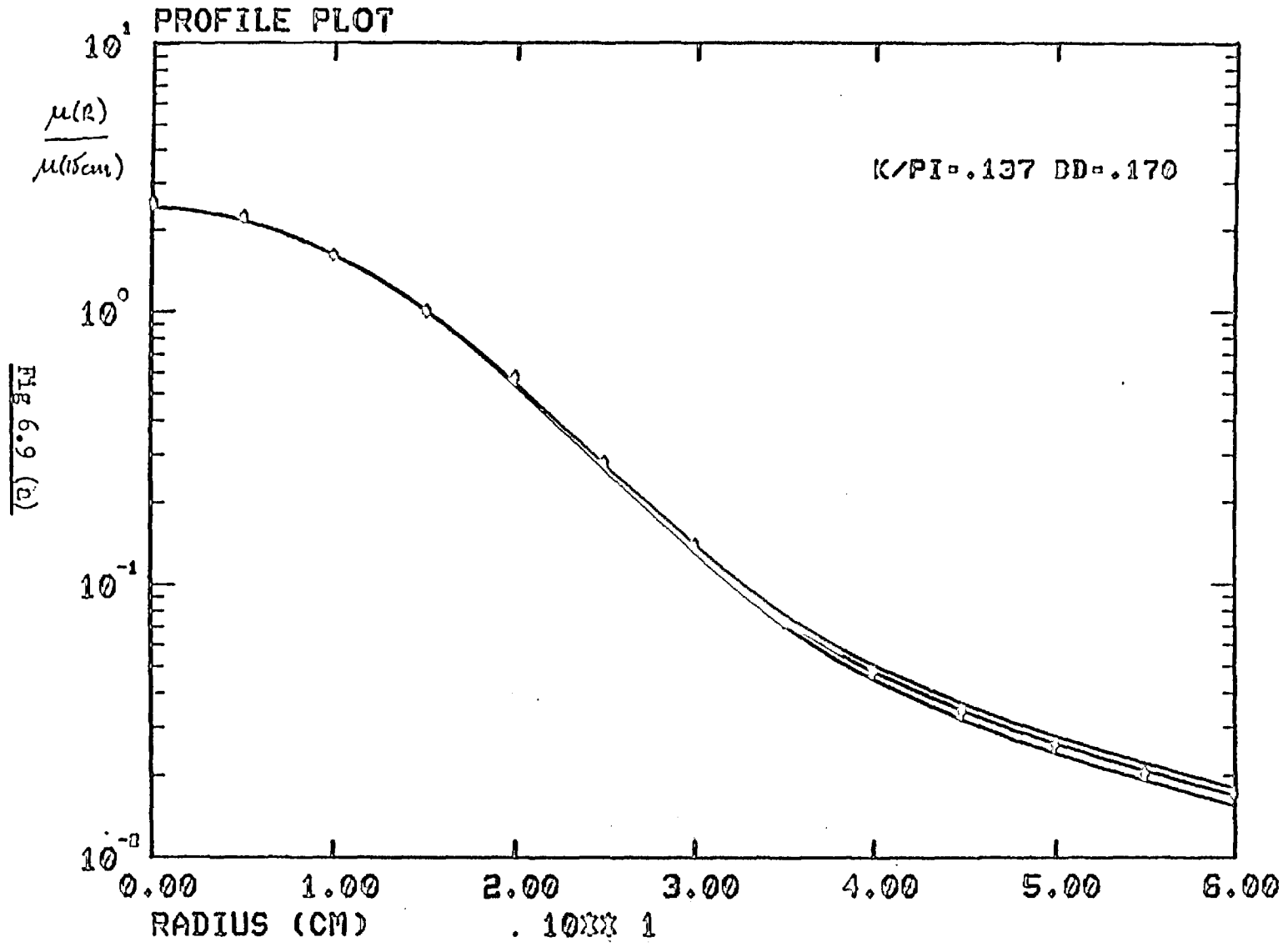
PROFILE PLOT
10^{1}
$\frac{\mu(R)}{\mu(15cm)}$
K/PI=.137 DD=.170
10^{0}
10^{-1}
10^{-2}
0.00
1.00
2.00
3.00
4.00
5.00
6.00
RADIUS (CM)
. 10XX 1

Fig 6.9 (a)

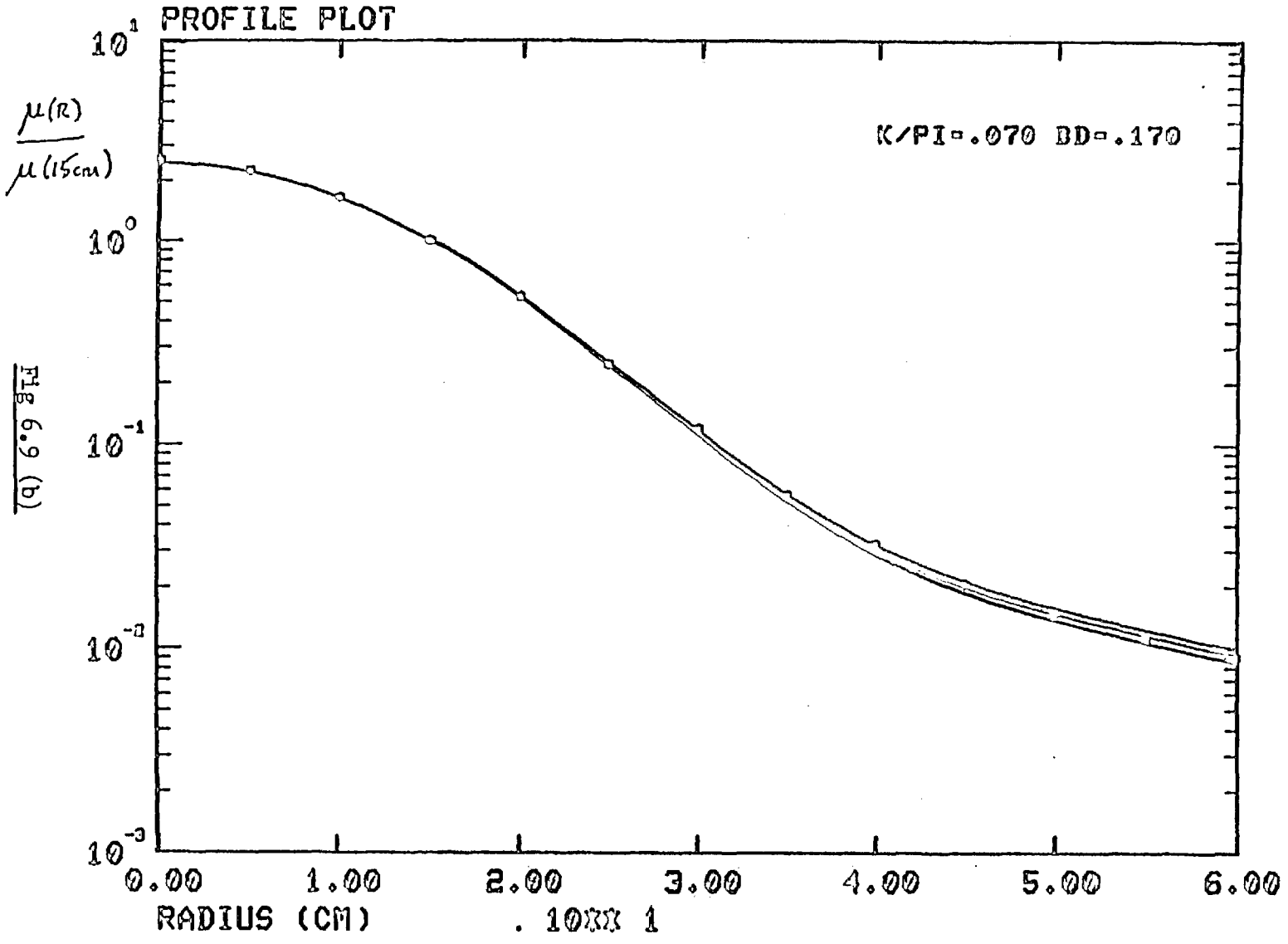
PROFILE PLOT
10^{1}
$\frac{\mu(R)}{\mu(15cm)}$
10^{0}
10^{-1}
10^{-2}
10^{-3}
K/PI=.070 BD=.170
$\frac{\text{FIG 6.9 (b)}}{}$
0.00
1.00
2.00
3.00
4.00
5.00
6.00
RADIUS (CM)
. 10XX 1

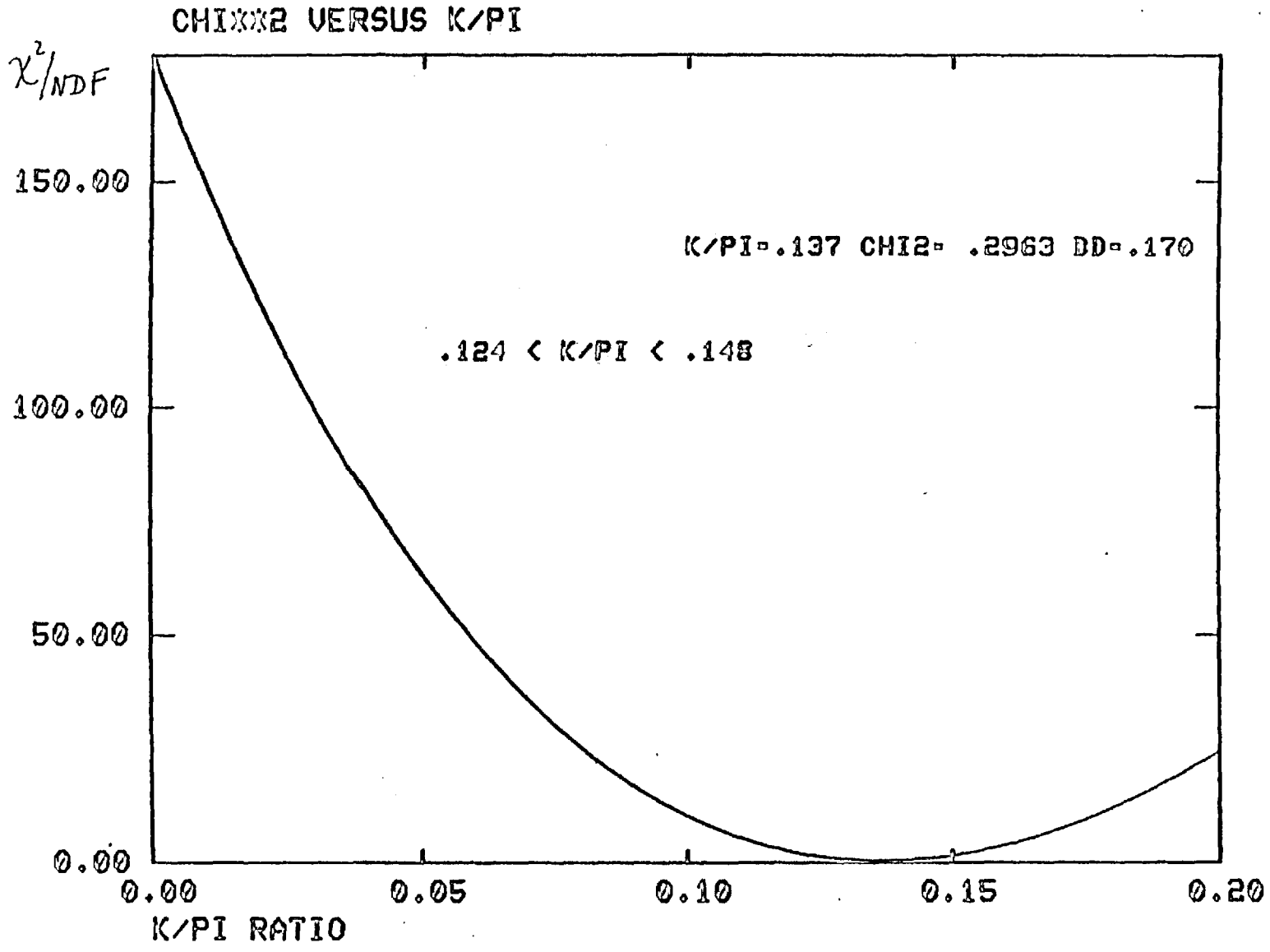
CHIXX2 VERSUS K/PI
χ²/NDF
150.00
100.00
50.00
0.00
K/PI=.137 CHI2= .2963 DD=.170
.124 < K/PI < .148
0.00
0.05
0.10
0.15
0.20
K/PI RATIO

FIG 6.9 (c)

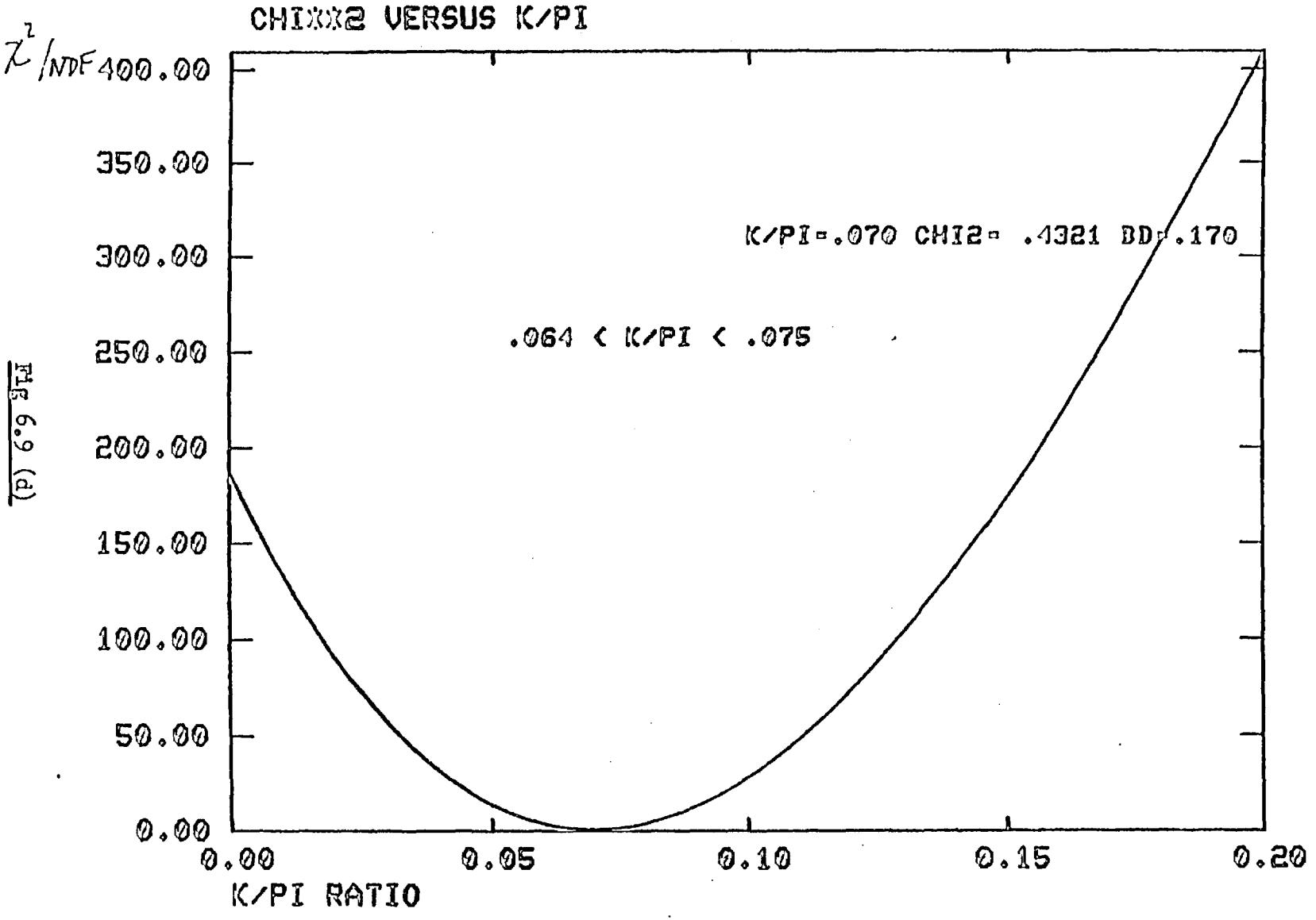
CHIXX2 VERSUS K/PI
χ²/NDF
400.00
350.00
300.00
250.00
200.00
150.00
100.00
50.00
0.00
FIG 6.9 (d)
K/PI=.070 CHI2= .4321 BD=.170
.064 < K/PI < .075
0.00
0.05
0.10
0.15
0.20
K/PI RATIO

```
7F- 1-25-08:16:40

 0    44   -.041   8829E-5    0       XXX
 2    53   2.225   1052E-4     .219   XXXX
 4    66   4.428   1315E-4     .480   XXXXX
 6   117   6.503   2332E-4     .858   XXXXXXXXXX
 8   174   7.865   3409E-4   1.255    XXXXXXXXXXXXXX
10   326  10.332   6524E-4   2.490    XXXXXXXXXXXXXXXXXXXXXXXXXXX
12   507  12.475   1014E-3   4.276    XXXXXXXXXXXXXXXXXXXXXXXXXXXXXXXXXXXXXXXXXXX
14   648  14.490   1295E-3   6.603    XXXXXXXXXXXXXXXXXXXXXXXXXXXXXXXXXXXXXXXXXXXXXXXXXXXXXX
16   771  16.440   1541E-3   9.370    XXXXXXXXXXXXXXXXXXXXXXXXXXXXXXXXXXXXXXXXXXXXXXXXXXXXXXXXXXXXXXXXX
18   849  18.327   1698E-3  12.427    XXXXXXXXXXXXXXXXXXXXXXXXXXXXXXXXXXXXXXXXXXXXXXXXXXXXXXXXXXXXXXXXXXXXXX
20   870  20.345   1739E-3  15.896    XXXXXXXXXXXXXXXXXXXXXXXXXXXXXXXXXXXXXXXXXXXXXXXXXXXXXXXXXXXXXXXXXXXXX
22   875  22.495   1749E-3  19.646    XXXXXXXXXXXXXXXXXXXXXXXXXXXXXXXXXXXXXXXXXXXXXXXXXXXXXXXXXXXXXXXXXXXXXX
24   845  24.450   1670E-3  22.989    XXXXXXXXXXXXXXXXXXXXXXXXXXXXXXXXXXXXXXXXXXXXXXXXXXXXXXXXXXXXXXXXXXXXX
26   782  26.471   1563E-3  26.258    XXXXXXXXXXXXXXXXXXXXXXXXXXXXXXXXXXXXXXXXXXXXXXXXXXXXXXXXXXXXXXXXXX
28   696  28.429   1392E-3  29.152    XXXXXXXXXXXXXXXXXXXXXXXXXXXXXXXXXXXXXXXXXXXXXXXXXXXXXXXXXX
30   593  30.452   1186E-3  31.763    XXXXXXXXXXXXXXXXXXXXXXXXXXXXXXXXXXXXXXXXXXXXXXXXXX
32   539  31.824   1077E-3  33.316    XXXXXXXXXXXXXXXXXXXXXXXXXXXXXXXXXXXXXXXXXXXXXX
34   427  34.373   8536E-4  35.777    XXXXXXXXXXXXXXXXXXXXXXXXXXXXXXXXXXXX
36   363  36.465   7262E-4  37.431    XXXXXXXXXXXXXXXXXXXXXXXXXXXXXXX
38   306  38.428   6111E-4  38.743    XXXXXXXXXXXXXXXXXXXXXXXXXX
40   244  40.458   4884E-4  39.859    XXXXXXXXXXXXXXXXXXXX
42   206  42.423   4124E-4  40.744    XXXXXXXXXXXXXXXXX
44   171  44.455   3429E-4  41.512    XXXXXXXXXXXXXX
46   150  46.422   2997E-4  42.144    XXXXXXXXXXXX
48   123  48.391   2454E-4  42.681    XXXXXXXXXX
50   106  50.361   2129E-4  43.132    XXXXXXXXX
52    88  52.331   1762E-4  43.516    XXXXXXX
54    76  54.435   1518E-4  43.861    XXXXXX
56    66  56.408   1324E-4  44.141    XXXXX
58    61  58.382   1220E-4  44.392    XXXXX
      58  60.423   1169E-4  44.636    XXXX
      43  65.365   8540E-5  45.136    XXX
      39  70.249   7846E-5  45.537    XXX
75    41  75.272   8208E-5  45.940    XXX
80    38  80.169   7545E-5  46.325    XXX
82    37  82.222   7401E-5  46.479    XXX
84    34  84.342   6791E-5  46.629    XX
86    39  86.200   7899E-5  46.766    XXX
88    37  88.324   7432E-5  46.929    XXX
90    37  90.249   7469E-5  47.072    XXX
92    41  92.375   8180E-5  47.238    XXX
94    46  94.369   9115E-5  47.411    XXX
96    47  96.298   9427E-5  47.590    XXXX
98    46  98.360   9217E-5  47.782    XXX
00    48 100.358   9646E-5  47.970    XXXX
02    54 102.357   1088E-4  48.176    XXXX
04    55 104.356   1106E-4  48.395    XXXX
06    56 106.424   1113E-4  48.624    XXXX
08    59 108.359   1184E-4  48.847    XXXXX
10    61 110.095   1227E-4  49.056    XXXXX
12    64 112.299   1282E-4  49.333    XXXXX
14    65 114.304   1298E-4  49.591    XXXXX
16    62 116.377   1239E-4  49.854    XXXXX
18    62 118.385   1245E-4  50.104    XXXXX
20    60 120.192   1195E-4  50.325    XXXXX
22    57 122.269   1137E-4  50.567    XXXX
24    56 124.414   1126E-4  50.810    XXXX
      52 126.291   1035E-4  51.013    XXXX
      51 128.371   1013E-4  51.226    XXXX
      47 130.318   9418E-5  51.416    XXXX
32    48 132.401   9519E-5  51.613    XXXX
34    39 134.417   7784E-5  51.788    XXX
36    36 136.434   7231E-5  51.939    XXX


38    42 138.385   8473E-5  52.092    XXX
40    46 140.338   9160E-5  52.264    XXX
42    34 142.426   6812E-5  52.431    XX
44    37 144.38    7427E-5  52.570    XXX
46    38 146.336   7636E-5  52.718    XXX
48    34 148.225   6828E-5  52.854    XX
50    35 150.317   6958E-5  52.999    XX
55    37 155.25    7451E-5  53.354    XXX
60    39 160.324   7881E-5  53.743    XXX
65    30 165.338   5976E-5  54.090    XX
70    29 170.223   5799E-5  54.378    XX
75    29 175.25    5882E-5  54.672    XX
80    34 180.285   6741E-5  54.989    XX
85    34 186.212   6756E-5  55.389    XX
90    34 190.306   6784E-5  55.667    XX
95    32 195.224   6445E-5  55.992    XX
00    36 200.217   7130E-5  56.331    XXX
```

Fig 6.10

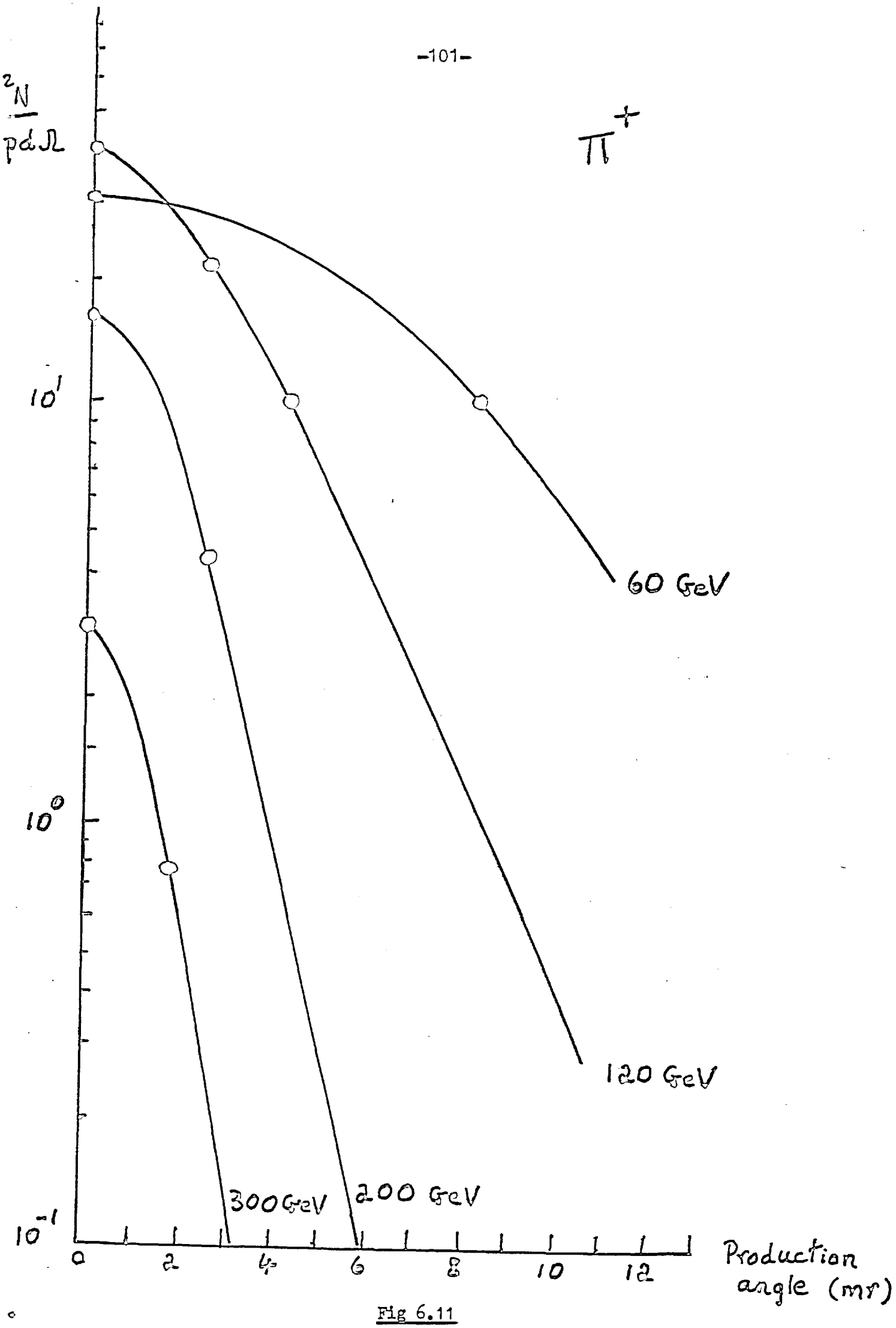
$\frac{d^2N}{pd\Omega}$
π^+
10^1
10^0
10^{-1}
60 GeV
120 GeV
200 GeV
300 GeV
0
2
4
6
8
10
12
Production angle (mr)

Fig 6.11

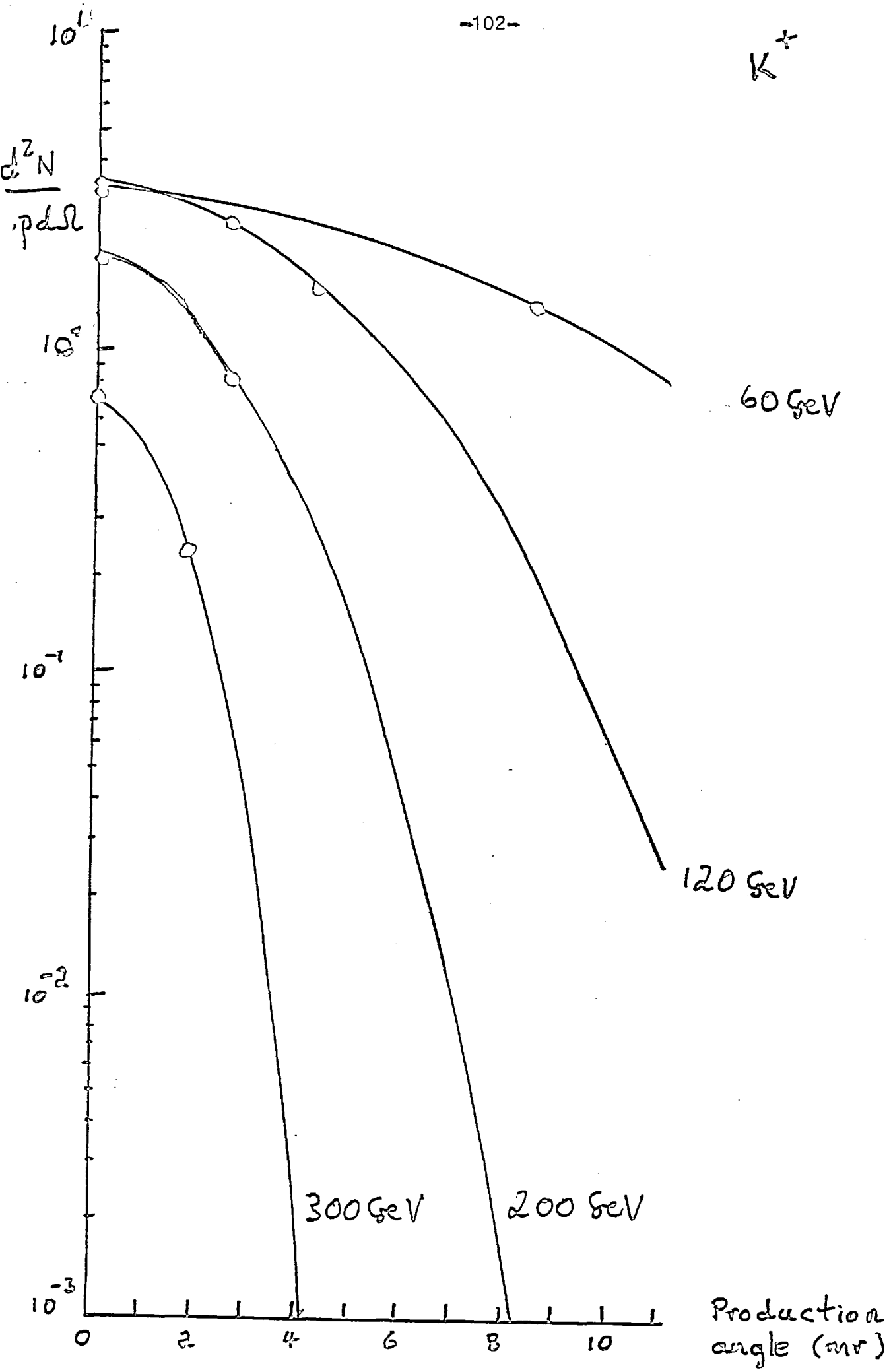
K^+
$\frac{d^2N}{pd\Omega}$
10^{1}
10^{0}
10^{-1}
10^{-2}
10^{-3}
60 GeV
120 GeV
200 GeV
300 GeV
0
2
4
6
8
10
Production angle (mr)

Fig 6.12

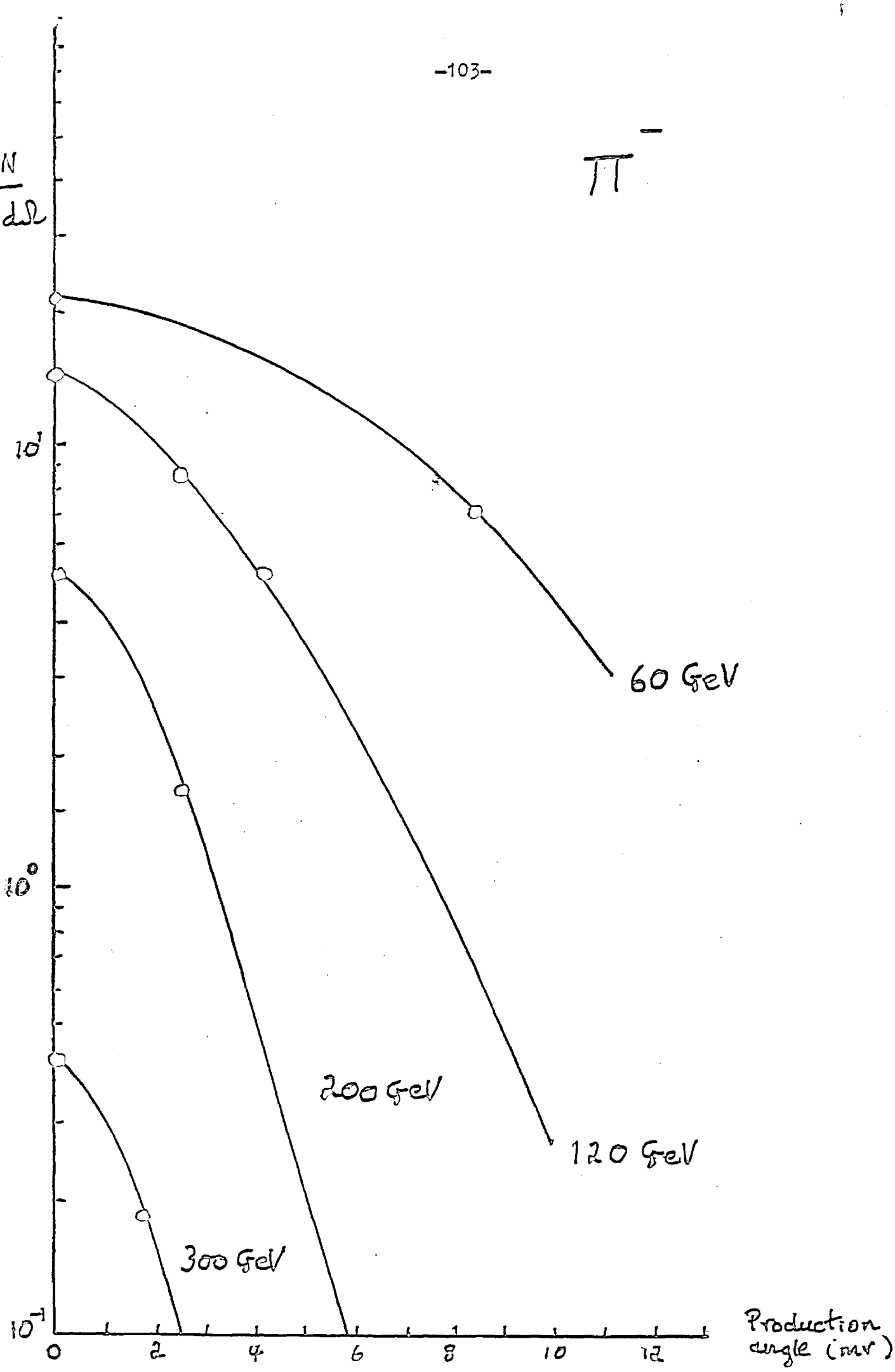
$\frac{N}{d\Omega}$
π^-
10^1
10^0
10^{-1}
60 GeV
120 GeV
200 GeV
300 GeV
0
2
4
6
8
10
12
Production angle (mr)

Fig 6.13

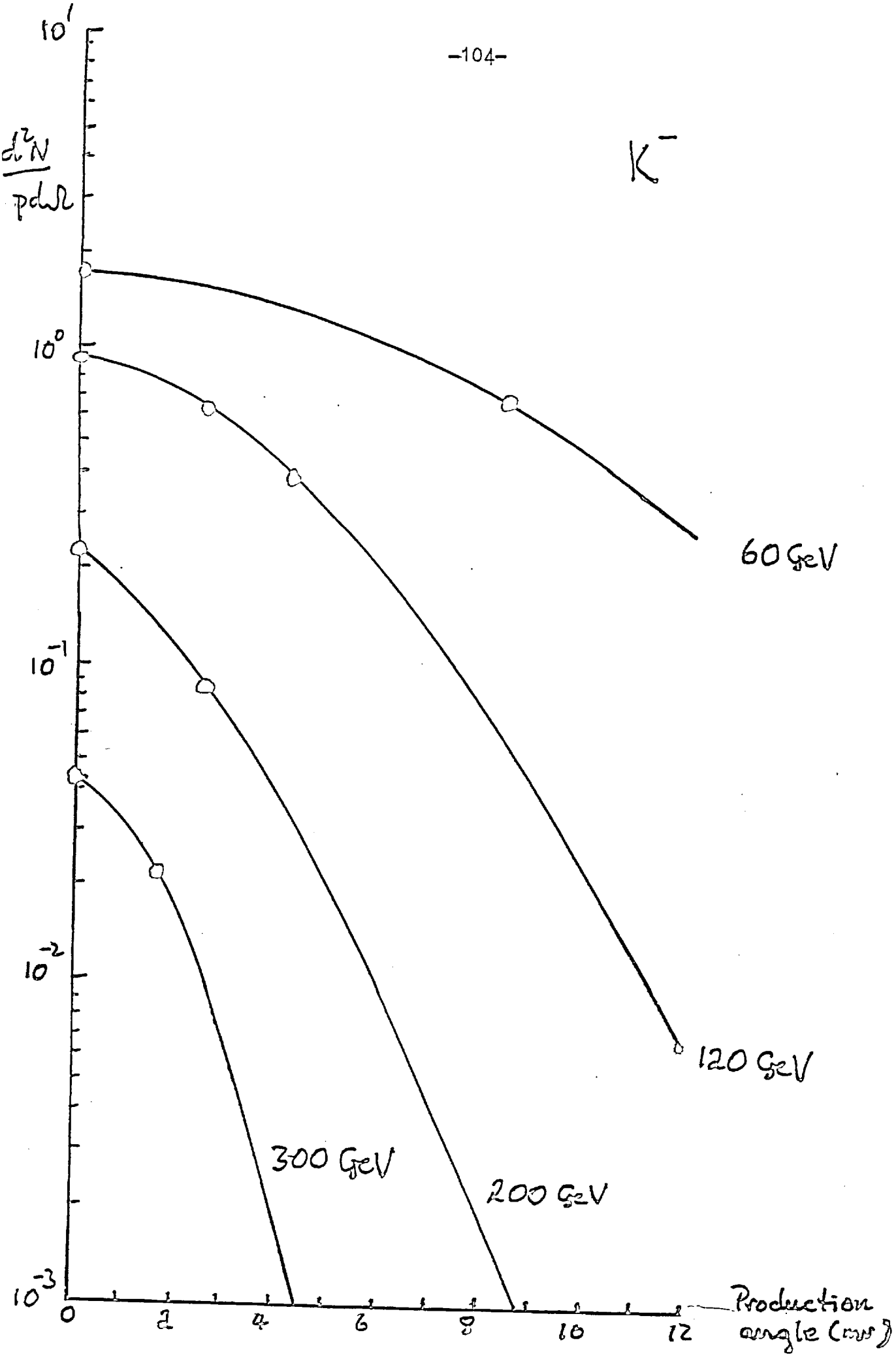
10^1
$\frac{d^2N}{pd\Omega}$
K^-
10^0
60 GeV
10^{-1}
120 GeV
10^{-2}
300 GeV
200 GeV
10^{-3}
0
2
4
6
8
10
12
Production angle (mr)

Fig 6.14

Interpolation	K/π
$\sqrt{\theta}$	.136
θ	.145
θ^2	.130

Fig 6.15

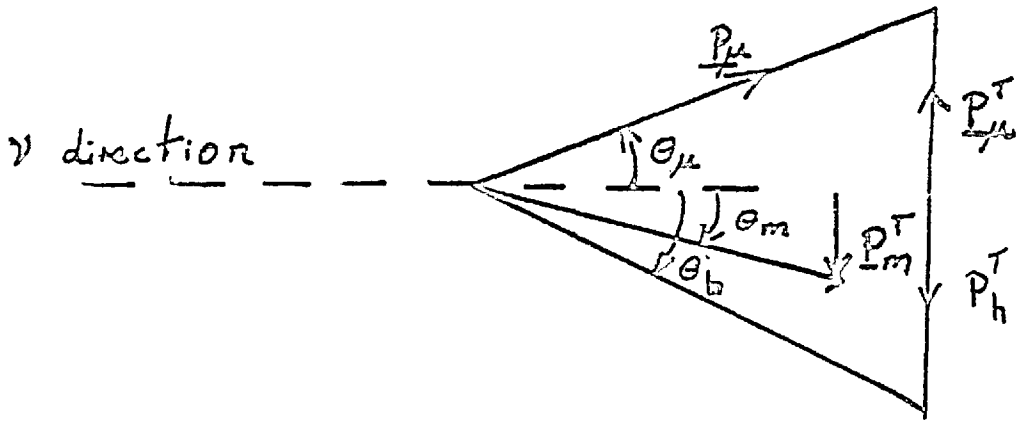

P^T = The muon transverse momentum

P_μ = The muon momentum vector

P_h^T = The hadronic transverse momentum in the mu-nu plano

P_m = The measured hadronic transverse momentum in the mu-nu plane.

θ_μ = The angle of the muon with respect to the beam

θ_h = The angle of the hadronic vector with respect to the beam in the mu-nu plane.

θ_m = The angle of the measured hadrons with respect to the beam direction in the mu-nu plane.

Fig 7.1

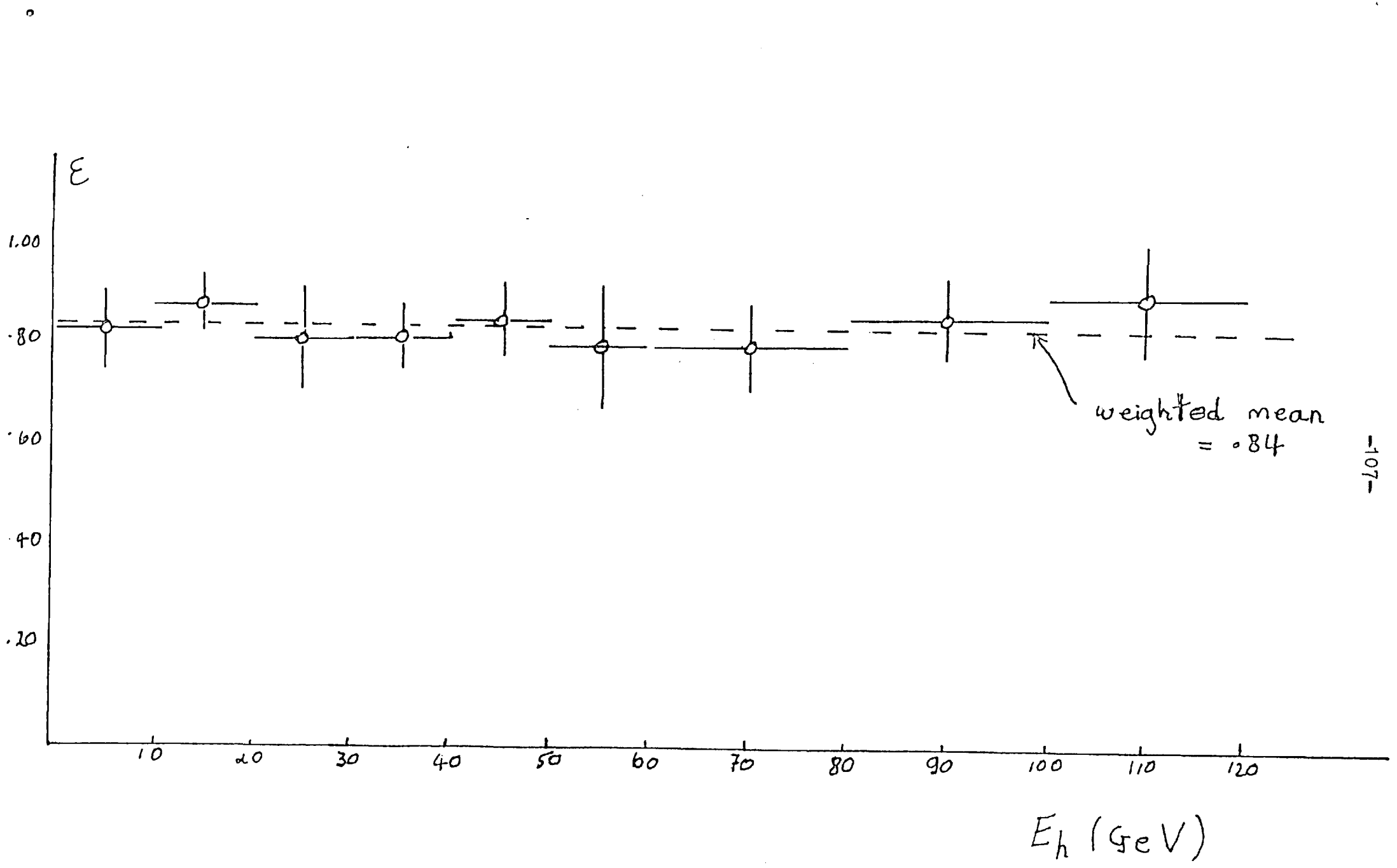
ε
1.00
·80
·60
·40
·20
10
20
30
40
50
60
70
80
90
100
110
120
weighted mean
= ·84
E_h (GeV)

Fig 7.2

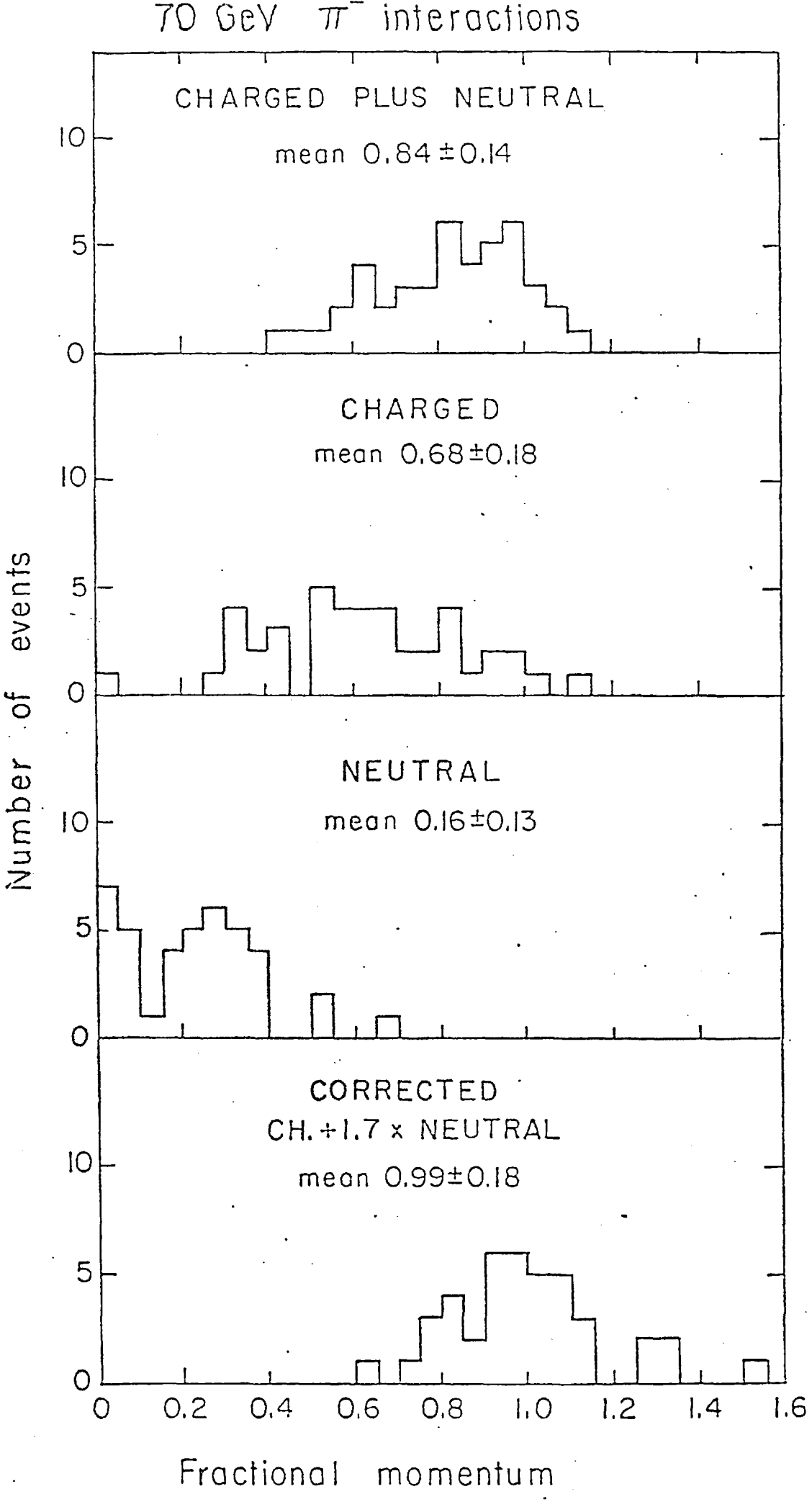
70 GeV π⁻ interactions
CHARGED PLUS NEUTRAL
mean 0.84±0.14
CHARGED
mean 0.68±0.18
NEUTRAL
mean 0.16±0.13
CORRECTED
CH.+1.7 x NEUTRAL
mean 0.99±0.18
Number of events
Fractional momentum
0
5
10
0.2
0.4
0.6
0.8
1.0
1.2
1.4
1.6

Fig 7.3

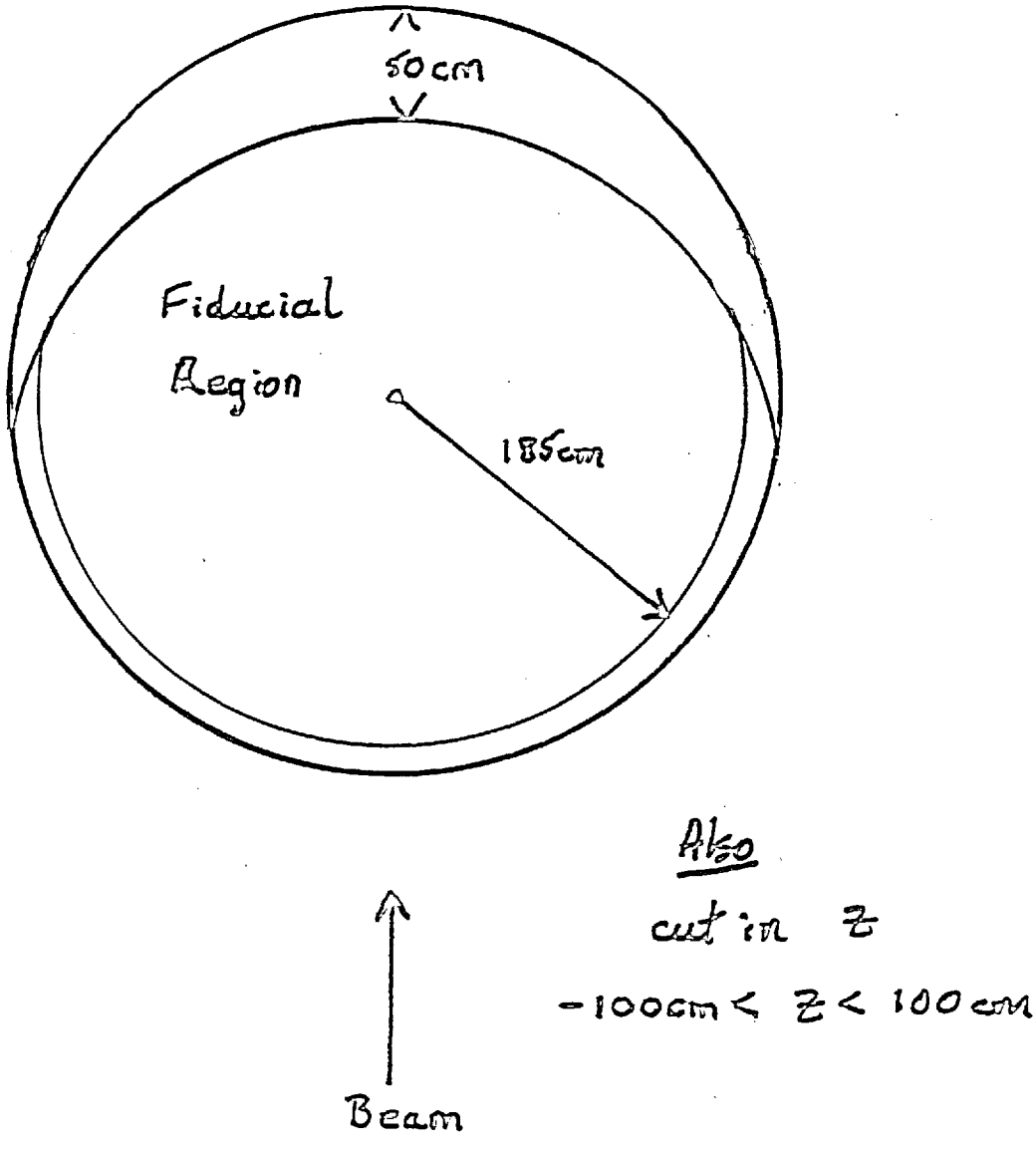

Fig 7.4

Wide Band Background

Correction Percentage

1	5.	15.	25.	35.	45.	55.	65.	75.	85.	95.	105.	115.	125.	135.	145.	155.	165.	175.	185.	195.	205.	215.
2	.018	.022	.027	.022	.022	.010	.025	.032	.027	.022	.014	.023	.019	.023	.043	.012	.022	.033	.031	.010	.000	.000
3	.010	.021	.020	.020	.022	.010	.021	.034	.024	.110	.014	.023	.019	.023	.043	.012	.023	.033	.031	.010	.000	.000
4	20	54	50	49	52	54	59	50	53	0	0	0	0	0	0	0	0	0	0	0	0	0
5	0	1	1	1	1	0	1	2	2	0	0	0	0	0	0	0	0	0	0	0	0	0
6	0	0	0	0	0	3	5	10	11	13	12	15	13	12	12	13	11	10	0	4	0	0
7	0	0	0	0	0	0	0	0	0	0	0	0	0	0	0	0	0	0	0	0	0	0

1) Neutrino energy (GeV)
2) Correction percentage (neutrino)
3) Correction percentage (antineutrino)
4) total flux
5) background flux
6) total flux
7) background flux

Fig 7.5

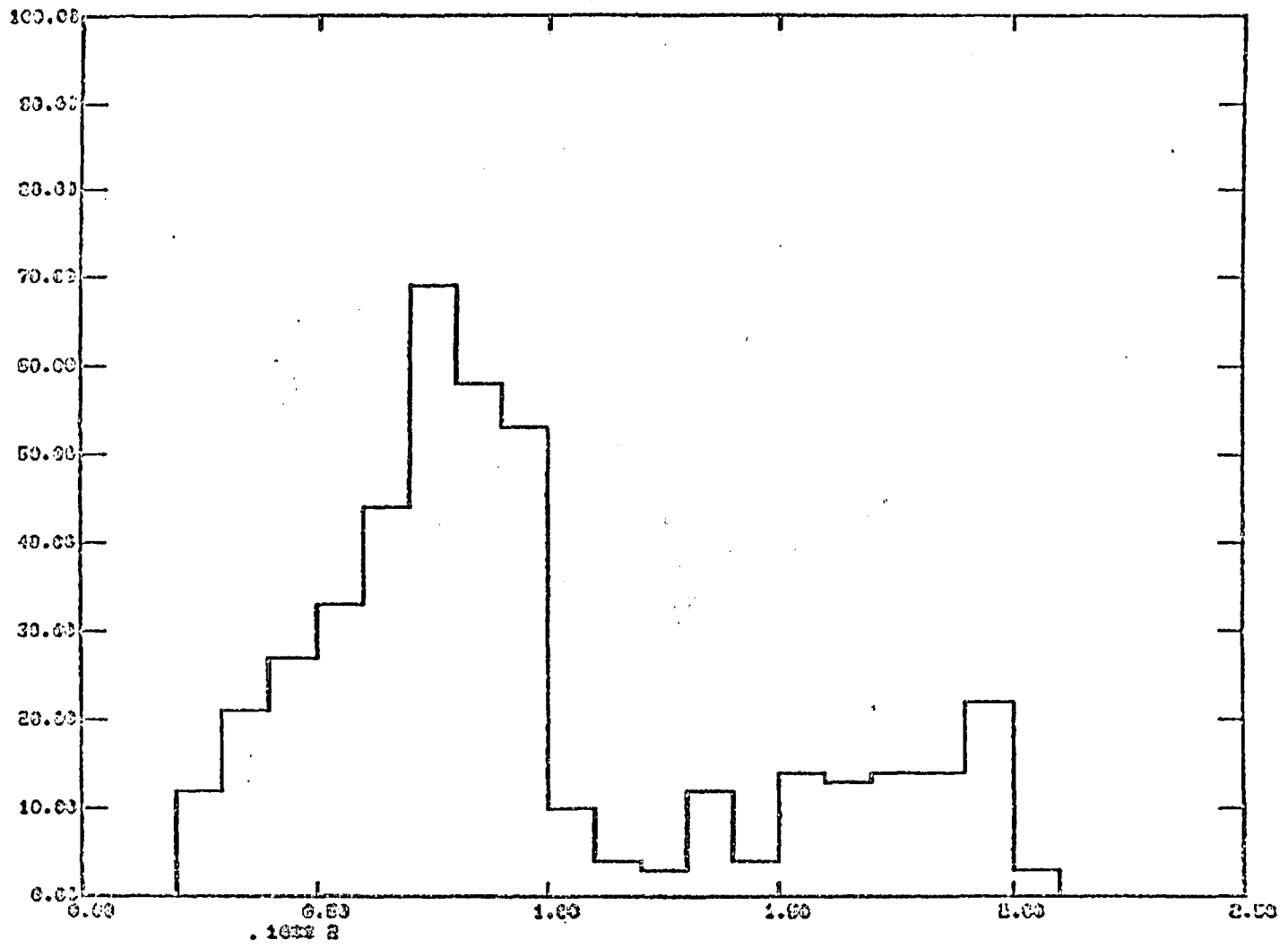
Events
100.00
80.00
70.00
60.00
50.00
40.00
30.00
20.00
10.00
0.00
0.00
1.00
1.50
2.00
$E_{\bar{\nu}}$ (GeV x 10^2)

Fig 7.6

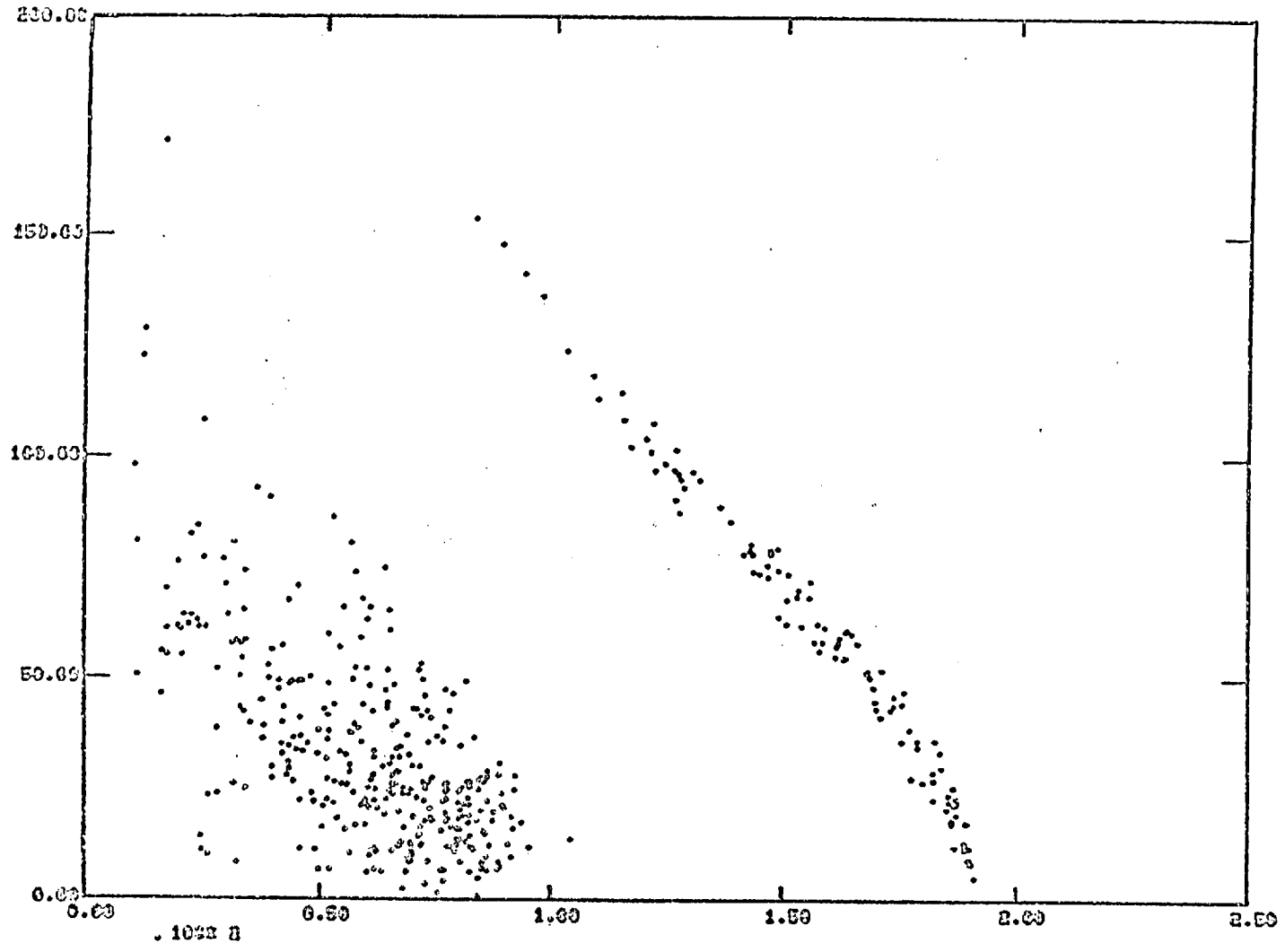

Fig 7.6 (continued)

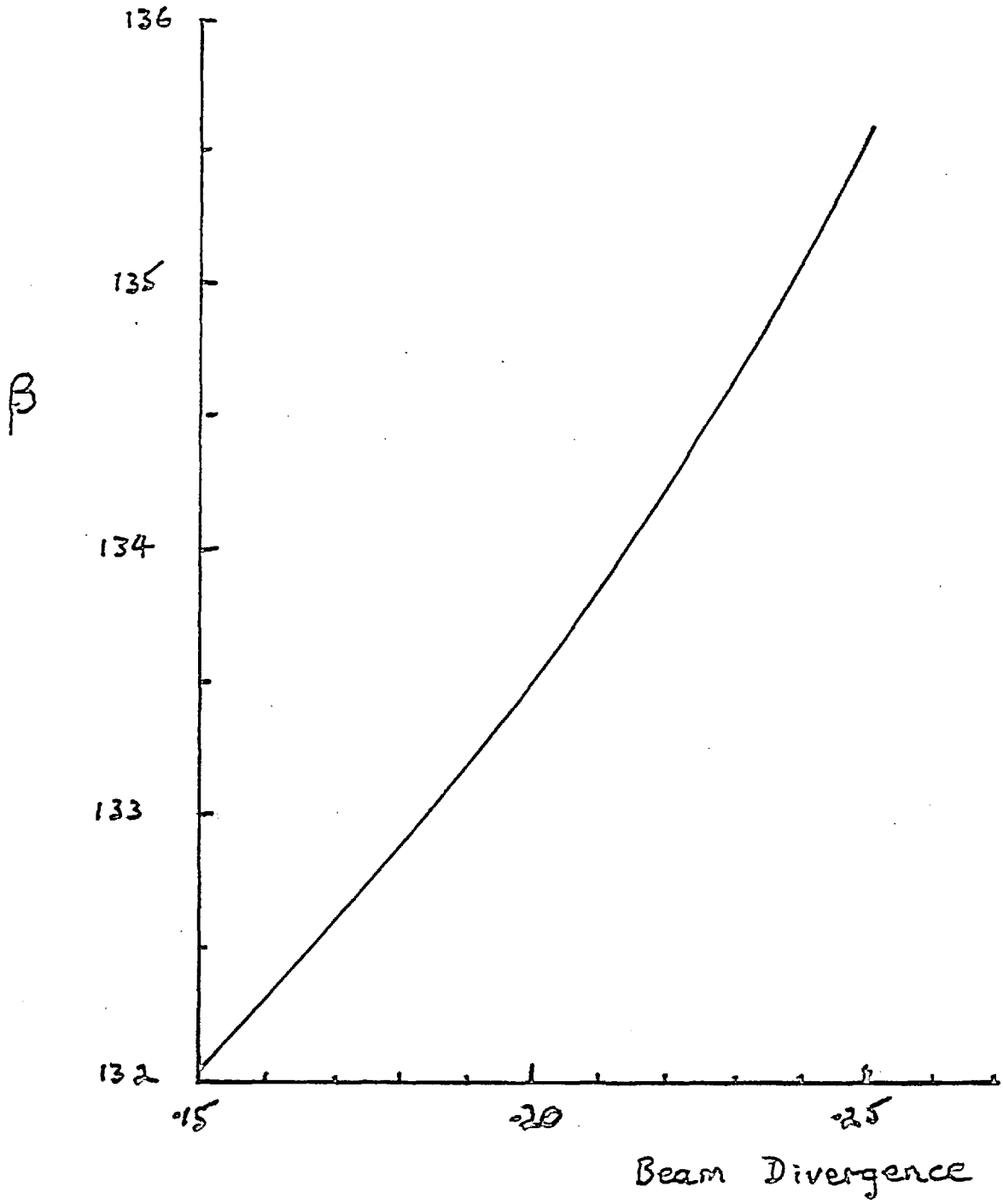

$$\beta = \frac{\text{Number of events in BEBC with } E_\nu > 20\,\text{GeV}, P_\mu < 5\frac{\text{GeV}}{c}}{\text{Total 15cm Flux in pit 2 } (K/\pi = \cdot 047)}$$

assuming $\frac{\sigma^{\bar{\nu}}}{E_{\bar{\nu}}} = 1.$

Fig 7.7

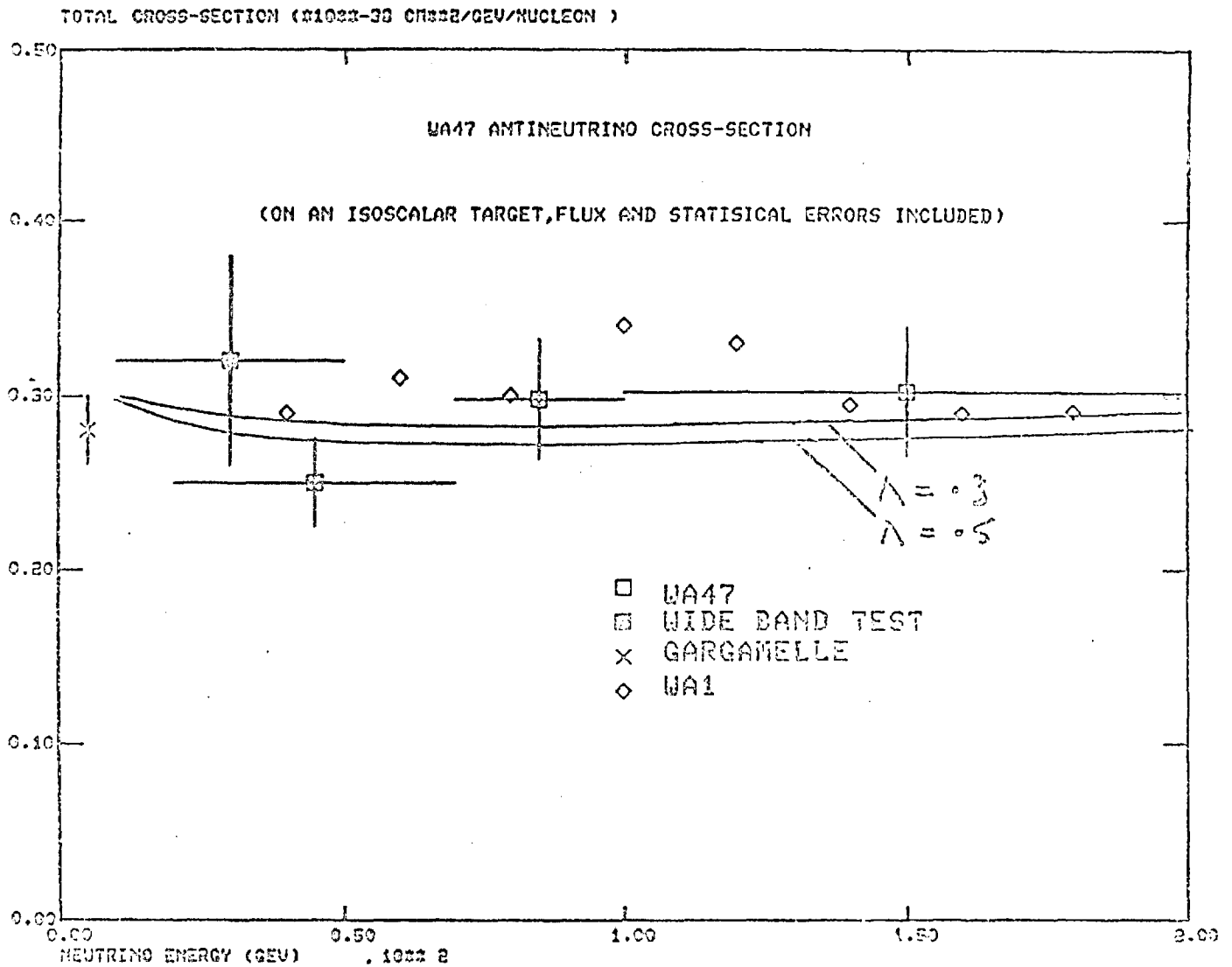
TOTAL CROSS-SECTION (*1000-38 CM**2/GEV/NUCLEON)
0.50
0.40
0.30
0.20
0.10
0.00
WA47 ANTINEUTRINO CROSS-SECTION
(ON AN ISOSCALAR TARGET,FLUX AND STATISICAL ERRORS INCLUDED)
Λ = 0.3
Λ = 0.5
WA47
WIDE BAND TEST
GARGAMELLE
WA1
0.00
0.50
1.00
1.50
2.00
NEUTRINO ENERGY (GEV) . 1000 2

Fig 7.8

SA47 ANTINEUTRINO CROSS-SECTION			
	20. - 70.	70. - 100.	100. - 200.
Number of Events	193.	119.	103.
$\frac{\sigma}{E}$ $\times 10^{-38}$ $cm^2/GeV/Nucleon$	.25±.03	.30±.03	.30±.04

Fig 7.8 (continued)

CHAPTER 1

REFERENCES

1.1 E. FERMI Z. PHYSIK 88 161 (1934)

1.2 REINES & COWAN Phys. Rev. 113 273 (1959)

1.3 DANBY et al. Phys. Rev. Lett. 9 36 (1962)

1.4 S.WEINBERG Phys. Rev. Lett. 19 1264 (1967)
A. SALAM Elementary Particle Physics N. Svartholm Ed. (Almquist and Wiksell Stockholm p. 367, 1968)

1.5 MASERT et al, Phys. Lett. 46B 138 (1973)

1.6 S.L. GLASHOW, J. ILLIOPOULOS and L. MIANI Phys. Rev. D2 1285 (1970)

1.7 M.L. PERL et al, Phys. Rev. Lett. 35 1489 (1973)

1.8 III Phys. Inst. Der Tech, Lehrstuhl B. RWTH Aachen.

1.9 Phys. Inst. Der Univ. Bonn, Nussalle 12, D-53 Bonn.

1.10 CERN CH-1211 Genève 23.

1.11 Imperial College. Blackett Lab. Prince Consort Rd. London. SW7.

1.12 Oxford Univ. Nuclear Physics Lab, Keble Rd., Oxford OX1 3RM

1.13 CEA Saclay, Orme des Merisiers B.P. No. 2 F - 91190 Gif - sur - Yvette.

CHAPTER 2 REFERENCES CONT...

2.1 R.P. FEYNMAN and M. GELL-MANN, Phys. Rev. 109 193 (1958)
2.2 J.D. BJORKEN Phys. Rev. 148 1467 (1966), 179 1547 (1969)
2.3 C.G. CALLAN and D.J. GROSS Phys. Rev. Lett. 22 156 (1969)
2.4 D.J. GROSS and C.M. LLEWELLYN-SMITH Nucl. Phys. B14 337 (1969)
2.5 E.M. RIORDAN et al. SLAC-PUB 1634 (1975)

CHAPTER 3

3.1 BEBC Users Handbook
3.2 IC/HENP/PN/79/2 Imperial College Physics Note
3.3 L. PAPE Private communication

CHAPTER 4

4.1 E.J. HEIJNE - CERN/EF/BEAM 77 - 1 (1977) Solid State Detectors used in the Neutrino Flux Monitoring
4.2 H. WACHSMUTH CERN/EP/PHYS. 77 43 Physics of Neutrino Beams
4.3 H.W. ATHERTON CERN/Lab. II/EA/74 - 6 Some Characteristics of the WANF Narrow Band Beam

CHAPTER 5

4.1 G. CAVALLARI NFM - WB MAG TAPE FORMATS
5.2 G. SIGURDSON Narrow band beam data blocks (Also available from CERN)
5.3 HANFMSUM HYDRA Application Library Write-Up
5.4 HYDRA System Manual

CHAPTER 6 REFERENCES CONT .....

6.1 H.W. WACHSMUTH, Private communication.

6.2 J. MAY, Private comminucation.

CHAPTER 7

7.1 P.C. BOSSETTI et al, Phys. Lett. 70B 273 (1977)

7.2 B. BARISH et al, Phys. Rev. Lett. 39 1595 (1977)

7.3 CDHS Collaboration, Inclusive Interactions of High Energy Neutrinos and Antineutrinos in Iron (Nov. 1978) Submitted to Zeitschrift für Physik.

7.4 G. MYATT CERN/ECFA/ 72 - 4 Vol. III 172 (1972)

7.5 BURAS + R.J.F. GAEMERS Phys, Lett. 71B 106 (1977)

ACKNOWLEDGEMENTS

I would like to express my thanks and appreciation to the following people and organisations:-

The Science Research Council for the award of a grant to enable the work described in this thesis to be carried out.

Prof. I.Butterworth for the opportunity of working in the H.E.N.P group at Imperial College.

My supervisor Dr. K.W.J.Barnham for constant support during the course of my stay at Imperial College.

Dr. H.W.Wachsmuth at CERN for initiating me into the delights and mysteries of Neutrino Beams.

Dr E.Clayton provided many helpful comments and criticisms of the text in chapters 1 - 4.

All the scanners and computing staff at Imperial College for their unceasing efforts on behalf of the Neutrino Experiment.

Finally, but by no means least, my sister Jacqueline for typing the bulk of this thesis in record time. Any mistakes that remain are solely my own doing.